Příloha číslo 1:

David Šorm, Bogdana Bashta, Jan Blahut, Ivana Císařová, Lada Dolejšová Sekerová, Eliška Vyskočilová, Jan Sedláček, Porous Polymer Networks Cross-Linked by Novel Copper Schiff Base Complex: From Synthesis to Catalytic Activity, *European Polymer Journal*, *184*, **2023**, 111772.

European Polymer Journal 184 (2023) 111772

Contents lists available at ScienceDirect

European Polymer Journal

journal homepage: www.elsevier.com/locate/europolj

Porous polymer networks cross-linked by novel copper Schiff base complex: From synthesis to catalytic activity

David Šorm[a,*], Bogdana Bashta[a], Jan Blahut[b,c], Ivana Císařová[d], Lada Dolejšová Sekerová[e], Eliška Vyskočilová[e], Jan Sedláček[a,*]

[a] Department of Physical and Macromolecular Chemistry, Faculty of Science, Charles University, Hlavova 2030, Prague 2 128 43, Czech Republic
[b] Department of Chemistry, Faculty of Science, Charles University, Hlavova 2030, Prague 2 128 43, Czech Republic
[c] Institute of Organic Chemistry and Biochemistry of the Czech Academy of Sciences, Flemingovo náměstí 542/2, Prague 6 160 00, Czech Republic
[d] Department of Inorganic Chemistry, Faculty of Science, Charles University, Hlavova 2030, Prague 2 128 43, Czech Republic
[e] Department of Organic Technology, University of Chemistry and Technology in Prague, Technická 5, Prague 6 166 28, Czech Republic

ARTICLE INFO

Keywords:
Porous polymer networks
Microporous polyacetylenes
Schiff base
Copper
Heterogeneous catalysis

ABSTRACT

A new ethynylated Schiff base complex, [Cu(SALANI)$_2$], in which two *N*-salicylidene(3-ethynylaniline) (SALANI) ligands coordinated one Cu^{2+} ion, was prepared and characterized by single-crystal X-ray diffraction, FTIR and ^{1}H NMR spectroscopy. The ^{1}H NMR spectra were obtained and interpreted (with the help of DFT calculation) despite the paramagnetic character of the [Cu(SALANI)$_2$] complex. Chain-growth copolymerization of [Cu(SALANI)$_2$] with 4,4′-diethynylbiphenyl and 1,4-diethynylbenzene provided polyacetylene-type micro/mesoporous organometallic networks with [Cu(*N*-salicylideneaniline)$_2$] segments as network knots. Networks of this type were also prepared by postpolymerization metalation of polyacetylene networks containing *N*-salicylideneaniline segments as pendant groups. Postpolymerization metalation (leading to further cross-linking) enabled to transform nonporous parent networks into organometallic networks with permanent porosity. The new porous organometallic networks showed a specific surface area from 400 to 700 m^2/g and a Cu^{2+} content of about 6 wt %. The networks prepared by both prepolymerization and postpolymerization metalation were active as heterogeneous catalysts of oxidation of linalool to linalool oxide.

1. Introduction

Schiff base complexes of metal ions are well known as versatile catalysts of many different reactions including oxidation, isomerization, epoxidation, condensation, polymerization and ring-opening/forming reactions [1–3]. In addition to imine CH=N group(s) the Schiff bases derived from salicylaldehyde also contain hydroxy group(s) suitably positioned for metal binding. The lone pair electrons of the N atom of the imine group(s) and the deprotonated hydroxy group(s) participate in the coordination of the metal ions in such complexes. The negative charge of the deprotonated OH group(s) fully or partially compensates the positive charge of the coordinated metal ion. Salen-type tetradentate ligands [various *N,N*′-ethylene-bis(salicylimine)s] containing two imine groups and two hydroxy groups are probably the most used ligands of catalytically active Schiff base complexes [4]. Complexes with bidentate *N*-substituted salicylimine ligands (e.g. of the *N*-salicylideneaniline-type) containing one pair of CH=N and OH groups are reported less frequently as the catalysts in the literature [1,5]. On the other hand, various complexes with bidentate *N*-substituted salicylimine ligands were prepared and tested in non-catalytic applications. For example, Kargar *et al.* reported Cu and Zn complexes with bidentate Schiff-base ligands composed from ring-substituted salicylaldehyde and ring-substituted anilines or aminopyrazoles. The complexes were applied as antibacterial agents and their binding to DNA was studied [6–9].Fig. 1..

Much attention has been paid to the heterogenization of Schiff base complexes aimed at the preparation of easily separable and potentially reusable catalysts [10,11]. For example, Mn, Fe, and Cu salen complexes were anchored on surface-modified siliceous mesoporous molecular sieves of various types to form porous heterogeneous catalysts for the synthesis and transformation of epoxides [12,13] and Henry reaction [14]. Efficient heterogeneous catalysts were also achieved by immobilizing Schiff base complexes on (i) polymer resins [15], (ii) graphene oxide [16], (iii) glass beads [17], (iv) magnetic nanoparticles [18] and other supports.

---

* Corresponding authors.
E-mail addresses: david.sorm@natur.cuni.cz (D. Šorm), jan.sedlacek@natur.cuni.cz (J. Sedláček).

https://doi.org/10.1016/j.eurpolymj.2022.111772
Received 21 October 2022; Received in revised form 10 December 2022; Accepted 14 December 2022

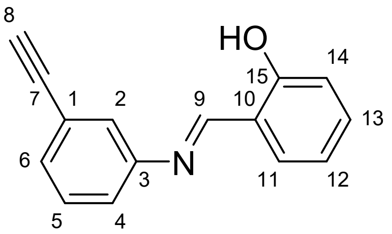

Fig. 1. Structure of the proligand/monomer SALANIH with numbered atoms according to the NMR spectra.

In several cases, heterogenization was carried out by covalent incorporating Schiff base complexes as building blocks into so-called Porous Organic Polymers (POPs) while maintaining the catalytic activity of these complexes. POPs are amorphous polymer networks with permanent micro/mesoporosity and a high specific surface area originating from the stiffness of the network segments combined with extensive cross-linking [19,20]. A number of different polymerization and postpolymerization procedures have been developed for the preparation of POPs, which allowed to tune the covalent structure and textural parameters of these materials. This makes POPs very promising for a number of applications, especially in the field of reversible sorption [21–24] and heterogeneous catalysis [25–29]. Xie et al. prepared a POP containing Co-salen segments by Sonogashira cross-coupling copolymerization of 1,3,5-triethynylbenzene and a dibromo-functionalized Co-salen complex. The prepared POP contained Co-salen segments as the struts between benzene-triyl knots and showed a Brunauer-Emmett-Teller specific surface area, S_{BET}, of 965 m^2/g [29]. Co-salen containing hyper-cross-linked POPs with S_{BET} up to 663 m^2/g were achieved by a knitting polymerization of the Co-salen complex with a 1,4-bis(bromomethyl)benzene cross-linker [30]. POPs containing Schiff base complexes with Al, Co and Ni ions were prepared by condensation polymerization of 2,3,6,7,14,15-hexaammoniumtriptycene with 2,6-diformyl-4-methylphenol in the presence of salts of respective metals [31]. One pot condensation reaction of 5-*tert*-butyl-4-hydroxyisophthalaldehyde, ethylenediamine, and copper(II) acetate provided POPs composed of Cu-salen and porphyrin segments [32]. The S_{BET} values up to 280 m^2/g were achieved. Schiff base complexes containing POPs were active as heterogeneous catalysts for the Henry reaction [32] and for the conversion of epoxides and CO_2 to cyclic carbonates [29–31].

Linear substituted polyacetylenes, i.e. mostly soluble polymers of formulas $[\text{–HC=CR-}]_n$ and $[\text{-R}_1\text{C=CR}_2\text{-}]_n$, are the first described conjugated polymers [33]. Polyacetylenes are prepared by transition metal-catalyzed coordination chain-growth polymerization of acetylenes, $HC{\equiv}CR$ and $R_1C{\equiv}CR_2$ [34,35]. In this way, not only hydrocarbon acetylenes but also monomers functionalized with a whole range of heteroatom groups, including imino [36–38] and hydroxy groups [39,40], were successfully polymerized into linear polymers. Recently, we modified and optimized this polymerization to provide micro- and micro/mesoporous hyper-cross-linked networks of the POP-type (S_{BET} ~ 1000 m^2/g) [28,35,41]. In order to ensure extensive cross-linking of the products, aromatic acetylenes with two to four ethynyl groups per molecule were used as (co)monomers. The resulting POPs consisted of conjugated polyacetylene (polyene) main chains in which single and double bonds alternated. These chains were hyper-cross-linked by rigid arene-type cross-links. The polymerization was well compatible with different heteroatom groups of monomers, which enabled the preparation of functionalized POPs for specific sorption, catalytic and luminescence applications [24,42–45].

In this paper, we report new micro/mesoporous organometallic polyacetylene POPs containing molecules of *N*-salicylideneaniline complex with Cu^{2+} ions as network knots. These POPs were achieved by chain-growth polymerization of ethynylated precursors combined with either prepolymerization or postpolymerization metalation with copper (II) acetate. Both methods provided organometallic POPs with a high content of Cu^{2+} ions which were active as heterogeneous catalysts for oxidation of linalool.

2. Experimental Section

Materials: (Acetylacetonato)(norbornadiene)rhodium(I), [Rh(nbd) acac], (>98 %), 4,4′-diethynylbiphenyl, DEBPh (>98 %), 1,4-diethynylbenzene, DEB (>98 %), 3-ethynylaniline (>98 %) (all TCI Europe), copper(II) acetate, $Cu(OAc)_2$ (98 %), salicylaldehyde (≥99 %), salicylideneaniline (97 %), methanol (≥99 %), tetrahydrofuran (≥99 %), *tert*-butylhydroperoxide (water solution 70 %) (all Merck), linalool (>95 %, Aroma Praha, a.s.), dichloromethane (99.95 %, Lach-Ner) was distilled with P_2O_5.

Synthesis of proligand/monomer: *N*-Salicylidene(3-ethynylaniline), SALANIH, was prepared by smooth condensation of 3-ethynylaniline (21 mmol) with salicylaldehyde (21 mmol) in a minimal amount of methanol at room temperature. The reaction mixture was stirred for 90 min during which the product was formed as a precipitate. The product was washed in cold methanol and dried under a vacuum. Yield 69 %.

ν_{max} (KBr)/cm^{-1} 631 s, 684 s, 755 s, 939 m, 1140 m, 1212 m, 1284 s, 1368 m, 1502w, 1565 s, 1620 s, 2105vw, 3285 s.

δ_H (CD_2Cl_2, 400 MHz) 12.99 (s, $1H^{OH}$), 8.65 (s, $1H^9$), 7.45 (d, $1H^{11}$), 7.42 (d, $1H^6$), 7.40 (d, $1H^2$), 7.39 (d, $1H^5$), 7.01 (d, $1H^{13}$), 6.99 (d, $1H^{12}$), 6.97 (d, $1H^{14}$), 6.95 (d, $1H^4$), 3.20 (s, $1H^8$).

δ_C (CD_2Cl_2, 100 MHz) 164.2 (C^9), 161.5 (C^{15}), 149.0 (C^3), 133.9 (C^{arom}), 133.1 (C^{arom}), 130.8 (C^{arom}), 130.0 (C^{arom}), 125.0 (C^{arom}), 123.5 (C^{arom}), 122.6 (C^{arom}), 119.6 (C^{arom}), 119.5 (C^{arom}), 117.5 (C^{arom}), 83.2 (C^7), 78.1 (C^8).

(^1H and $^{13}C\{^1H\}$ NMR spectra can be seen in **Figure S1** and **Figure S2** in the Supplementary Data).

HRMS ESI, measured (calculated) *m/z*: 222.091502 (222.091340), $C_{15}H_{11}NO$.

Melting point: 77.4 °C.

Synthesis of the [Cu(SALANI)$_2$] complex: 2.26 mmol of SALANIH was dissolved in 15 ml of methanol and 1.13 mmol of anhydrous copper (II) acetate was dissolved in 5 ml of distilled water. Both solutions were mixed in a vial and stirred for 5 days at room temperature. The precipitated complex [Cu(SALANI)$_2$] was isolated and washed with methanol and water, and dried under a vacuum. Yield 92 %.

Polymerization of [Cu(SALANI)$_2$]: [Cu(SALANI)$_2$] complex was homopolymerized and copolymerized with (i) DEBPh and with (ii) DEB. The polymerization catalyst was complex [Rh(nbd)acac] and reactions were performed in distilled dichloromethane. The total initial concentration of (co)monomer(s) was 0.3 mol/dm^3 and catalyst 0.025 mol/dm^3. In the copolymerization setup, two molar ratios were used: (i) 1:1 and (ii) 1:4 in favor of the cross-linker (DEBPh or DEB). The solution of the catalyst was mixed with the solution of (co)monomer(s). The reaction proceeded for 7 days at 75 °C. The precipitated product was isolated and washed in dichloromethane. The product was dried under a vacuum. Organometallic polyacetylene networks (NET-1, NET-2, NET-3, NET-4 and NET-5) were prepared in quantitative yields.

Copolymerization of proligand/monomer: SALANIH was copolymerized with (i) 4,4′-diethynylbiphenyl (DEBPh) and with (ii) 1,4-diethynylbenzene (DEB). The molar ratio of comonomers was 1:1. Polymerization catalyst was [Rh(nbd)acac] complex and reactions were performed in distilled dichloromethane. The total initial concentration of comonomers was 0.3 mol/dm^3 and catalyst 0.025 mol/dm^3. The solution of the catalyst was mixed with solutions of monomers, which started the polymerization. The reaction proceeded for 7 days at 75 °C. The precipitated product was separated from the liquid and washed in dichloromethane. The product was dried under a vacuum. In this way, non-metalated parent networks Poly(SALANIH-*co*-DEBPh) and Poly (SALANIH-*co*-DEB) were prepared in quantitative yields.

Postpolymerization metalation of Poly(SALANIH-*co*-DEBPh) and Poly(SALANIH-*co*-DEB): Non-metalated polymer network (0.4

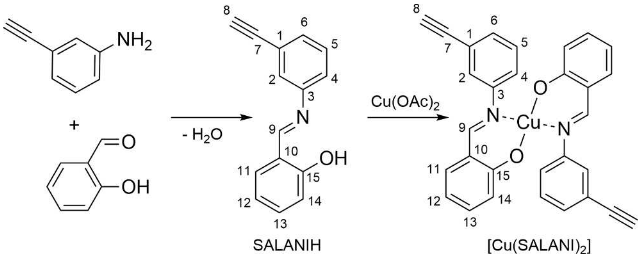

Scheme 1. Synthesis of SALANIH and [Cu(SALANI)$_2$].

mmol of SALANIH units) was dispersed in 2 ml of tetrahydrofuran and 0.2 mmol of copper(II) acetate dissolved in 2 ml of tetrahydrofuran were added into that dispersion. The reaction mixture was stirred at room temperature for 10 days. After that, the solid was separated by filtration, washed in tetrahydrofuran, and dried under a vacuum. In this way, the organometallic polyacetylene networks (NET-6 and NET-7) were prepared.

2.1 Testing of catalytic activity

The prepared metalated polymer networks were tested as the catalysts for oxidation of linalool. The catalyst (10 mg) was dispersed in dichloromethane (3 ml) in a reaction flask (25 ml) equipped with a condenser. The reaction flask was placed on the magnetic stirrer in the preheated oil bath (60 °C). Followingly, *tert*-butylhydroperoxide (molar ratio to linalool 3:1) and linalool (100 mg) were added under vigorous stirring. The reaction was carried out for 24 h, after that, the sample of the reaction mixture was analyzed using GC coupled with a flame ionization detector. The evaluation factors for catalytic activity were (i) conversion (calculated as the difference in the amount of linalool at the beginning and at the end of the reaction) and (ii) selectivity (calculated as a ratio of the areas of GC peaks of linalool oxide and linalool, A_{LO}/A_L, at the end of the reaction).

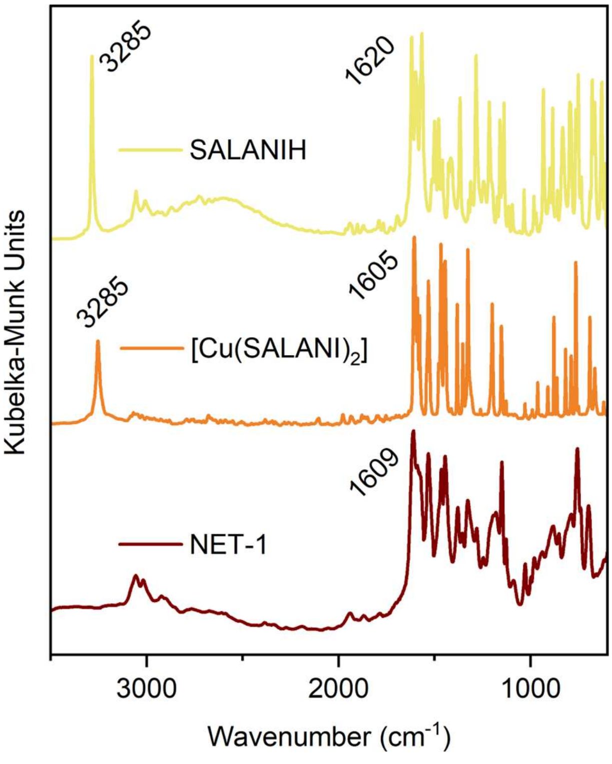

Fig. 2. FTIR spectra of proligand/monomer SALANIH, complex [Cu(SALANI)$_2$] and homopolymer network NET-1.

2.2 Techniques

Nitrogen adsorption and desorption isotherms were measured at 77 K using Triflex V4.02 apparatus (Micromeritics). The finely ground solid samples were first degassed (Micromeritics SmartVacPrep instrument) under a vacuum at a temperature of 383 K and a residual pressure of 1 Pa and then the adsorption and desorption isotherms were measured. The measurement was performed up to the value of relative nitrogen pressure $p/p_0 = 0.99$ ($p_0 = 101\ 325$ Pa). The specific surface area, S_{BET}, was calculated by the method of Brunauer, Emmett and Teller from the amount of adsorbed nitrogen in the range p/p_0 from 0.05 to 0.20. The volume of micropores, V_{mi}, was determined from the adsorbed amount of nitrogen at $p/p_0 = 0.1$ and the total pore volume, V_{tot}, was determined from the adsorbed amount of nitrogen at $p/p_0 \sim 0.99$. The density of liquid nitrogen at the boiling point of nitrogen was considered for the calculation, $\rho = 0.806$ g/cm^3. The maximum in micropore diameter distribution, D_{mi}, was subtracted from Horvath-Kawazoe differential pore volume plot. Atomic Absorption Spectrometry (AAS) was used to determine the content of Cu^{2+} ions. Before the measurement, the sample was first completely decomposed in a Biotage Initiator microwave reactor in HNO_3 or $HNO_3/HClO_4$ medium. The mineralized sample was then measured on a Perkin Elmer Model 3110 instrument. UV/VIS spectra were recorded on Perkin Elmer Lambda 465. A Nicolet Magna IR 760 spectrometer and a Diffuse Reflectance Infrared Fourier Transform Spectroscopy (DRIFTS) method were used to characterize solid, finely ground samples. KBr was used as the background. HR-MS (high-resolution mass spectrometry) spectra were obtained on a Bruker Q-TOF Compact instrument. ^{1}H and ^{13}C{^{1}H} NMR spectra of soluble SALANIH were measured on Bruker AVANCE III 400 MHz in CD_2Cl_2. The ^{1}H and ^{13}C{^{1}H} spectra of paramagnetic [Cu(SALANI)$_2$] were acquired on Bruker Avance III 600 MHz spectrometer (300 K, 14.3 T) using a direct-excitation spin-echo-detected experiment [46]. Crystallographic data were collected on Bruker D8 VENTURE Kappa Duo PHOTONIII by IμS micro-focus sealed tube MoKα (λ = 0.71073) at a temperature of 120(2) K. The structure was solved by direct methods (XT) [47] and refined by full-matrix least squares based on F^2 (SHELXL2018) [48]. The hydrogen atoms on carbon were fixed into idealized positions (riding model) and assigned temperature factors $H_{iso}(H) = 1.2\ U_{eq}$(pivot atom). Shimadzu GC 17-A with non-polar column ZB–5 (60 m, ID 0.32 mm, SF 0.25 μm coupled with a flame ionization detector was used for the analysis of reaction mixtures after catalytic tests.

3. Results and discussion

3.1. Synthesis of proligand/monomer

The main building block for the construction of organometallic polyacetylene networks reported in this article was a proligand/monomer *N*-salicylidene(3-ethynylaniline), SALANIH, which was synthesized by smooth condensation of 3-ethynylaniline with salicylaldehyde in methanol at room temperature (Scheme 1). SALANIH was designed to contain (i) a terminal ethynyl group suitable for chain-growth polymerization and (ii) a combination of imine (azomethine) and hydroxy groups suitable for metal ions complexation. SALANIH served as

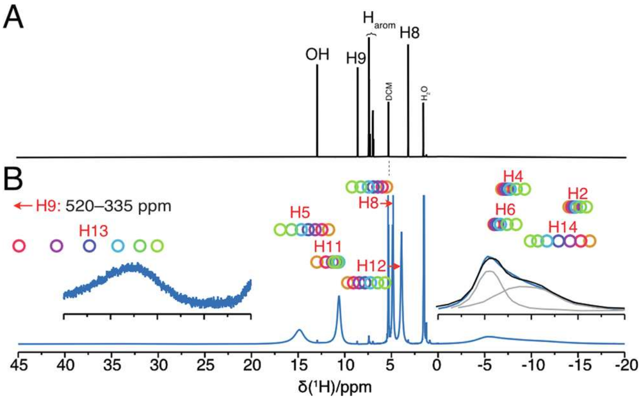

Fig. 3. ^{1}H NMR spectrum (14.3 T, 300 K) of (A) diamagnetic SALANIH and (B) paramagnetic [Cu(SALANI)$_2$] in CD_2Cl_2 solution. The rainbow-colored circles correspond to the calculated shifts using different Hartree–Fock exchange admixtures in hybrid DFT functional used for the hyperfine coupling calculations (Table S1), ranging from 10 % (orange) to 40 % (green). The H^9 signal (theoretically predicted in the region between 335 and 520 ppm) was not observed in the experimental spectrum due to fast paramagnetic-induced relaxation. Signals of H^2, H^4, H^6 and H^{14} are presented in an overlapped pattern between 0 and –20 ppm. Signal deconvolution is shown in gray.

proligand and/or monomer in our study.

The proligand/monomer SALANIH was used for the complexation of Cu^{2+} ions to form the [Cu(SALANI)$_2$] complex. Two molecules of deprotonated SALANIH coordinated one Cu^{2+} ion in [Cu(SALANI)$_2$] as confirmed by single-crystal X-ray diffraction (*vide infra*). This reaction was performed at room temperature in methanol/water (3/1 V/V), copper(II) acetate served as a source of Cu^{2+} ions. The yield of [Cu(SALANI)$_2$] was 92 %.

The evidence of successful complexation was gained from FTIR spectroscopy (see Fig. 2). The FTIR spectrum of SALANIH showed a characteristic band of CH=N stretching at 1620 cm^{-1}, while this band was slightly shifted to 1605 cm^{-1} in the spectrum of the [Cu(SALANI)$_2$] complex. This difference of 15 cm^{-1} indicated a change in the CH=N bond stretching due to metalation. A similar shift in the position of the CH=N stretching band was reported by Dong *et al.* who studied the complexation of Cu^{2+} ions with salen-type Schiff-base ligand [49]. The FTIR spectra of both SALANIH and [Cu(SALANI)$_2$] showed a strong band at 3285 cm^{-1} belonging to ≡C—H stretching of the ethynyl groups confirming that the ethynyl groups were not affected by metalation (see Fig. 2).

Figure S3 in the Supplementary Data shows UV–vis spectra of SALANIH and [Cu(SALANI)$_2$] in dimethylsulfoxide. The UV–vis spectrum of SALANIH contained two absorption bands at wavelength λ = 280 and 331 nm. The position of the latter band (ascribable to n → π* transition of the azomethine group) was significantly red-shifted in the spectrum of [Cu(SALANI)$_2$] due to the complexation of Cu^{2+} ions with SALANIH (λ = 384 nm). A similar bathochromic shift in the UV–vis spectra of free Schiff-base-type ligands and complexes of Cu^{2+} and other ions with these ligands were reported, for example, by Vinusha *et al.* who dealt with Schiff-base ligands composed of substituted benzaldehydes and aminotriazoles [50].

Additionally, the formation of the [Cu(SALANI)$_2$] was proved by NMR spectroscopy. The presence of a paramagnetic center in the vicinity of observed nuclei results in a substantial paramagnetic-induced shift and accelerated relaxation reflected in the signal broadening [46]. In our case, copper(II) in the square-planar coordination environment, induced the broadening of NMR signals to 50–4000 Hz and an increase of the spectral width to 60 ppm (see Fig. 3) which was in agreement with typically reported values [51]. Due to the fast relaxation and subsequent signal vanishing, the spectral assignment of the [Cu(SALANI)$_2$] resonances could not be completed by conventional methods of correlation spectroscopy (**Figure S4** in the Supplementary Data). Therefore, we

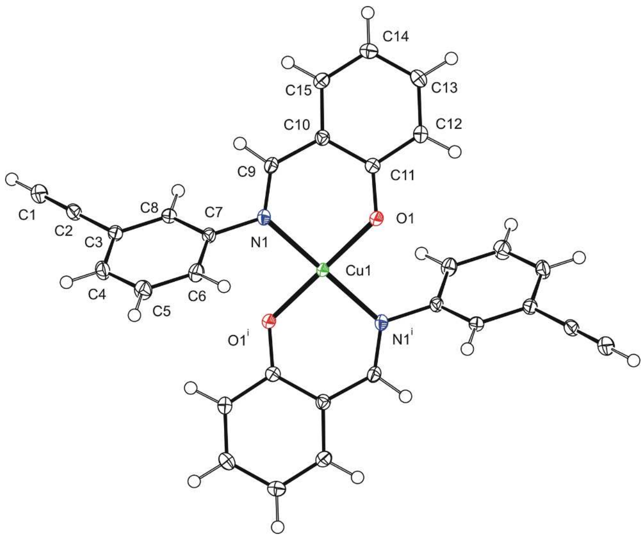

Fig. 4. View on the molecule of [Cu(SALANI)$_2$], the displacement ellipsoids are drawn at a 50 % probability level. Symmetry code: (i) -x + 1, -y + 1, -z + 1. The selected bond distances [Å] and angles [°]: Cu1-O1 1.8937(9), Cu1-N1 1.9959(11), N1-C9 1.2952(16), N1-C7 1.4377(15), O1-C11 1.3098(15), C1-C2 1.190(2); O1^{i}-Cu1-O1 180.0, O1-Cu1-N1 91.11(4), O1^{i}-Cu1-N1 88.89(4).

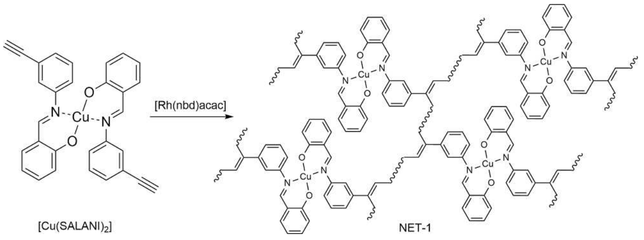

Scheme 2. Homopolymerization of [Cu(SALANI)$_2$] under the formation of NET-1.

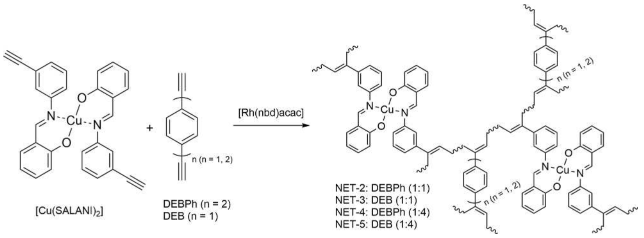

Scheme 3. Copolymerization of [Cu(SALANI)$_2$] with (i) DEBPh or (ii) DEB under the formation of NET-2 and NET-4 (with DEBPh comonomer) and NET-3 and NET-5 (with DEB comonomer).

employed a theoretical calculation of the paramagnetic-induced shift by DFT. A variable admixture of Hartree-Fock exchange was used here to estimate the calculation uncertainty due to DFT electron-density delocalization error as described in [52] and [53]. Conveniently, it provided a “confidence interval” of the calculation (rainbow plot in Fig. 3 and **Figure S4**, the numbering of atoms is shown in Scheme 1). Negative NMR-shift was observed for the nuclei H^2, H^4, H^{14} and H^6 which were in the positions *ortho* and *para* with respect to the coordinated group. Similarly, the nuclei H^5, H^{11} and H^{13}, localized in the *meta* position, showed a positive paramagnetic-induced shift. This phenomenon was probably related to spin-polarization effects. The signal of H^9 (from coordinated CH=N group) was predicted at an extremely high NMR shift (>300 ppm) but was not observed due to relaxation effects. On the contrary, acetylene H^8, which is distant from the Cu^{2+} ion, appeared at 4.85 ppm with a relatively narrow linewidth (~50 Hz).

Finally, the structure of the [Cu(SALANI)$_2$] complex (proposed in Scheme 1) was confirmed by the single-crystal X-ray diffraction (Fig. 4, see **Table S2** and more details in the Supplementary Data).

The complex consisted of two deprotonated *N*-salicylideneaniline ligands. This ligand had two benzene rings connected via an azomethine link (CH=N). The benzene ring attached to the carbon atom of the CH=N link bore an oxygen atom in the *ortho* position. The benzene ring attached to the nitrogen atom of the CH=N link was substituted (in the *meta* position) by an easily accessible terminal ethynyl group, which was suitable for the transformation into the polyacetylene chain. The deprotonated *N*-salicylideneaniline ligand coordinated the Cu^{2+} ion through coordination bonds between (i) the nitrogen atom and the Cu^{2+} ion and (ii) the oxygen atom and the Cu^{2+} ion. Two deprotonated *N*-salicylideneaniline ligands created with the Cu^{2+} ion centrosymmetric square complex with a small deformation of bond angles O1-Cu1-N1 (91.11°) and O1^{i}-Cu1-N1 (88.89°) and bound distances Cu1-O1 1.8937(9) Å, Cu1-N1 1.9959(11) Å. As seen from the X-ray determined structure, the Cu^{2+} ion had no ligand(s) above and below the plane of the complex, so the Cu^{2+} ion was easily accessible to the substrate molecules in terms of catalytic application.

3.2. *Organometallic polyacetylene networks by prepolymerization metalation approach*

The diethynylated [Cu(SALANI)$_2$] complex was (i) homopolymerized (Scheme 2) and (ii) copolymerized with 4,4′-diethynylbiphenyl (DEBPh) or 1,4-diethynylbenzene (DEB) (Scheme 3) in chain-growth polymerization manner. Polymerizations were initiated by [Rh(nbd)acac] complex at 75 °C. All polymerizations resulted in totally insoluble (dichloromethane, methanol, benzene, tetrahydrofuran) brown-black polymer networks with quantitative yields.

The homopolymerization of [Cu(SALANI)$_2$] provided poly[Cu(SALANI)$_2$] labeled as NET-1. The determined Cu^{2+} content in NET-1 was 13 wt%, which was in good agreement with the theoretical value of 12.6 wt % (Table 1). The FTIR spectrum of NET-1 (Fig. 2) did not show a band at 3285 cm^{-1}, which confirmed the highly efficient transformation of both terminal ethynyl groups of [Cu(SALANI)$_2$] into main-chain vinylene units of NET-1 during polymerization (Scheme 2). On the other hand, a strong FTIR band (at 1609 cm^{-1}) due to the CH=N group coordinating Cu^{2+} ion was retained in the spectrum of NET-1, which indicated that the transformation of [Cu(SALANI)$_2$] to NET-1 segments did not affect the mode of coordination of Cu^{2+} ions by *N*-salicylideneaniline. Thus, network NET-1 consisted of conjugated polyene (polyacetylene) chains

Table 1
Networks NET-1 to NET-5, their composition of monomeric units, specific surface area (S_{BET}), content of Cu^{2+}, micropore diameter (D_{mi}), volume of micropores (V_{mi}) and total pore volume (V_{tot}).

Network code	Comonomers		Molar ratio (A:B)	S_{BET} [m^2/g]	Content of Cu^{2+} [wt%]	D_{mi} [nm]	V_{mi} [cm^3/g]	V_{tot} [cm^3/g]	V_{mi}/V_{tot}
	A	B							
NET-1	[Cu(SALANI)$_2$]	–	–	13	**13.0**[a] *12.6*[b]	nd	nd	0.07	nd
NET-2	[Cu(SALANI)$_2$]	DEBPh	1:1	91	**8.8**[a] *9.0*[b]	1.06	0.03	0.18	0.17
NET-3	[Cu(SALANI)$_2$]	DEB	1:1	82	**10.4**[a] *10.1*[b]	1.10	0.03	0.17	0.18
NET-4	[Cu(SALANI)$_2$]	DEBPh	1:4	709	**4.9**[a] *4.8*[b]	0.73	0.27	1.58	0.17
NET-5	[Cu(SALANI)$_2$]	DEB	1:4	684	**5.6**[a] *6.3*[b]	0.71	0.26	1.19	0.22

[a] Determined value, [b] theoretical value.

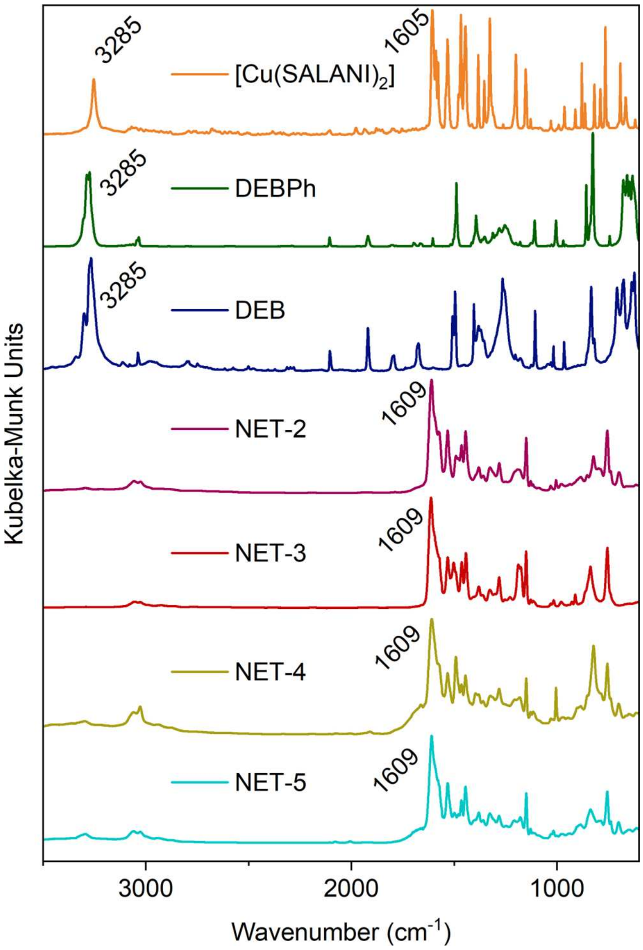

Fig. 5. FTIR spectra of [Cu(SALANI)$_2$], DEBPh, DEB and networks NET-2, NET-3, NET-4 and NET-5.

cross-linked by [Cu(*N*-salicylideneaniline)$_2$] cross-links. Despite the rigidity of the main polyene chains and the dense cross-linking, NET-1 was almost non-porous. The N_2 adsorption/desorption isotherms on NET-1 (at 77 K) detected a Brunauer-Emmett-Teller specific surface area (S_{BET}) of only 13 m^2/g and a total pore volume (V_{tot}) of only 0.07 cm^3/g. It should be mentioned that the previously reported polyacetylene networks cross-linked by short arylene links, prepared for example by polymerization of diethynylbenzenes, showed excellent micro/mesoporosity and S_{BET} values around 1000 m^2/g [41,42,54]. We speculated that the poor porosity of NET-1 could be due to the bulkiness and/or insufficient rigidity of the [Cu(*N*-salicylideneaniline)$_2$] cross-links, allowing tight packing of the network segments in the solid phase.

To support the formation of pores in [Cu(SALANI)$_2$]-based networks, we decided to introduce short rigid arylene cross-links into these types of networks in addition to cross-links derived from the [Cu(SALANI)$_2$] monomer. Networks with two different types of cross-links were prepared by copolymerization of [Cu(SALANI)$_2$] with diethynylated comonomers DEBPh and DEB (Scheme 3). Copolymerizations of [Cu(SALANI)$_2$] with DEBPh and DEB (molar ratio in the feeds: [Cu(SALANI)$_2$]:DEBPh = 1:1, [Cu(SALANI)$_2$]:DEB = 1:1) provided networks poly{[Cu(SALANI)$_2$]–*co*-DEBPh(1:1)} labeled as NET-2 and poly{[Cu(SALANI)$_2$]–*co*-DEB(1:1)} labeled as NET-3. Copolymerizations of the feeds of the mole composition [Cu(SALANI)$_2$]:DEBPh = 1:4 and [Cu(SALANI)$_2$]:DEB = 1:4 provided networks poly{[Cu(SALANI)$_2$]–*co*-DEBPh(1:4)} labeled as NET-4 and poly{[Cu(SALANI)$_2$]–*co*-DEB(1:4)} labeled as NET-5. The FTIR spectra of copolymer networks are shown in Fig. 5 together with the spectra of comonomers used for their synthesis. The FTIR spectra of all copolymer networks contained a strong band at 1609 cm^{-1} due to vibration of the CH=N bond participating in Cu^{2+} coordination. On the other hand, the band due to the ≡C—H vibration of the terminal ethynyl groups at about 3285 cm^{-1} was either absent (NET-2, NET-3) or only very weak (NET-4, NET-5) in the spectra of the copolymer networks. This indicated the highly efficient transformation of ethynyl groups achieved in the preparation of NET-2, NET-3, NET-4 and NET-5 and thus the high extent of cross-linking of these networks by [Cu(*N*-salicylideneaniline)$_2$] and 4,4′-biphenyldiyl or 1,4-phenylene cross-links (Scheme 3).

The cross-linking of the copolymer networks with arylene cross-links formed from DEBPh and DEB had the expected positive effect on the porosity of the networks. The S_{BET} values of NET-2 and NET-3 were 91 and 82 m^2/g, respectively, which was about six times higher compared to the homopolymer network NET-1. A further increase in the content of short arylene cross-links in the networks led to an increase in S_{BET} values even to 709 m^2/g (NET-4) and 684 m^2/g (NET-5) (Table 1). Cross-linking with 4,4′-biphenyldiyl and 1,4-phenylene cross-links realized by the copolymerization approach obviously reduced the Cu^{2+} content in the networks. However, even the highly porous NET-4 and NET-5 networks prepared by the copolymerization of feeds with a molar ratio [Cu(SALANI)$_2$]:DEBPh(or DEB) = 1:4 still showed a fully

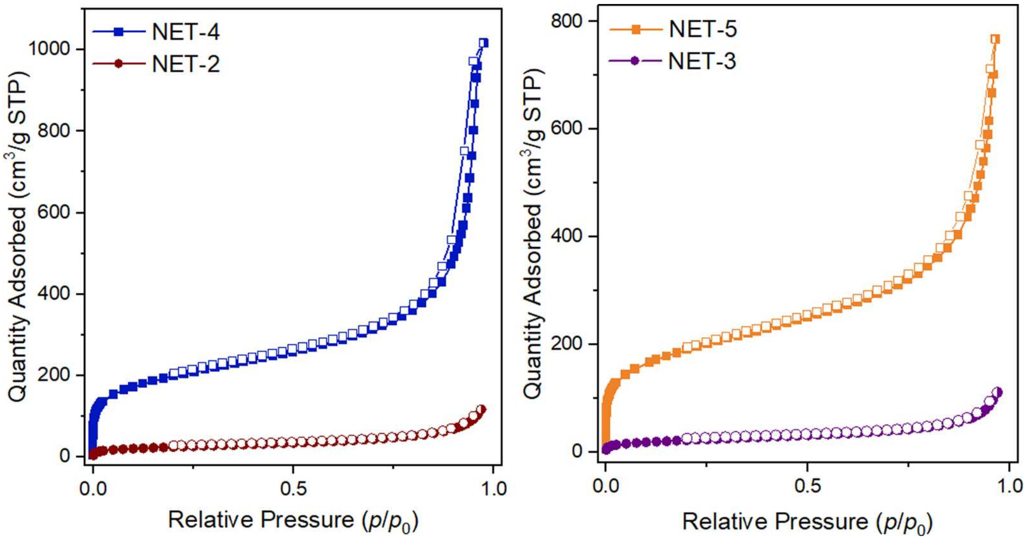

Fig. 6. N_2 adsorption (full symbols) and desorption (empty symbols) isotherms (measured at 77 K) on networks NET-2, NET-3, NET-4 and NET-5.

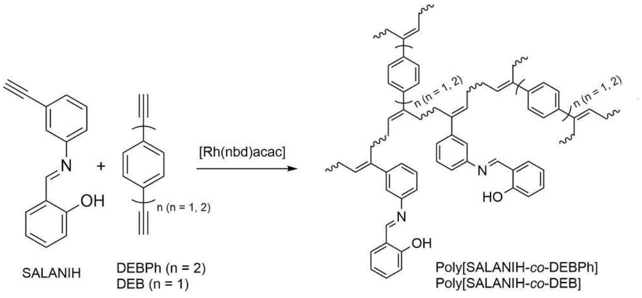

Scheme 4. Copolymerization of proligand/monomer SALANIH with (i) DEBPh or (ii) DEB under the formation of Poly(SALANIH-*co*-DEBPh) and Poly(SALANIH-*co*-DEB).

Table 2
Specific surface area (S_{BET}), micropore diameter (D_{mi}), volume of micropores (V_{mi}) and total pore volume (V_{tot}) of networks Poly(SALANIH-*co*-DEBPh), Poly(SALANIH-*co*-DEB), NET-6 and NET-7, content of Cu^{2+} for NET-6 and NET-7.

Before metalation Network code	S_{BET} [m^2/g]	D_{mi} [nm]	V_{mi} [cm^3]	V_{tot} [cm^3]	V_{mi}/V_{tot}	After metalation with Cu^{2+} Network code	Content of Cu^{2+} [wt%]	S_{BET} [m^2/g]	D_{mi} [nm]	V_{mi} [cm^3]	V_{tot} [cm^3]	V_{mi}/V_{tot}
Poly(SALANIH-*co*-DEBPh)	449	0.85	0.16	0.57	0.28	NET-6	**6.1**[a] *7.0*[b]	471	0.77	0.17	0.63	0.27
Poly(SALANIH-*co*-DEB)	3	nd	nd	0.01	nd	NET-7	**6.4**[a] *8.4*[b]	403	0.95	0.15	0.29	0.52

[a] Determined value, [b] theoretical value.

satisfactory Cu^{2+} content of about 5 wt% (see Table 1 for details).

Fig. 6 shows N_2 adsorption/desorption isotherms (77 K) on NET-2, NET-3, NET-4 and NET-5 (the N_2 adsorption/desorption isotherms are shown in more detail in **Figure S5** in the Supplementary Data). The shape of the isotherms indicated the micro/mesoporous texture of the networks. A steep increase in the adsorbed amount of N_2 in the relative pressure (p/p_0) region from 0 to 0.05 ($p_0 = 101\ 325$ Pa) confirmed the presence of micropores. The increase in the adsorbed amount of N_2 at $p/p_0 > 0.7$ and slight hystereses on the adsorption/desorption isotherms reflected the trapping of N_2 in the mesopores and interparticle voids. The values of total pore volume (V_{tot}) and micropore volume (V_{mi}) are summarized in Table 1. The highest V_{tot} and V_{mi} values, 1.58 and 0.27 cm^3/g, respectively, were obtained for NET-4. The V_{mi}/V_{tot} ratios ranged from 0.17 to 0.22 indicating that in NET-2, NET-3, NET-4 and NET-5 the micropores contributed to the total porosity in a similar manner. The micropore diameter distributions of NET-2, NET-3, NET-4 and NET-5 are shown in **Figure S6** in the Supplementary Data. The diameters corresponding to the maxima on these distributions (D_{mi}) are given in Table 1. The values of D_{mi} were approximately 0.7 nm for networks NET-4 and NET-5. Slightly higher values of D_{mi} (~1.1 nm) were found for NET-2 and NET-3, i.e. for networks with a lower content of 4,4′-biphenyldiyl and 1,4-phenylene cross-links.

3.3. *Organometallic polyacetylene networks by postpolymerization metalation approach*

Micro/mesoporous [$Cu(SALANI)_2$]-containing networks were achieved also by the postpolymerization metalation approach. For this purpose, two non-metalated polyacetylene networks were first prepared by copolymerization of SALANIH with DEBPh and DEB cross-linkers (Scheme 4). Copolymerization of SALANIH with DEBPh and

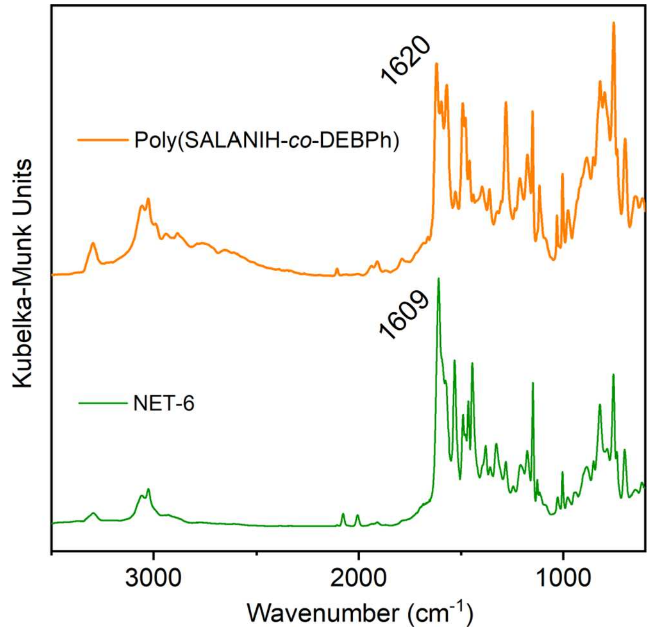

Fig. 7. FTIR spectra of parent network Poly(SALANIH-*co*-DEBPh) and NET-6.

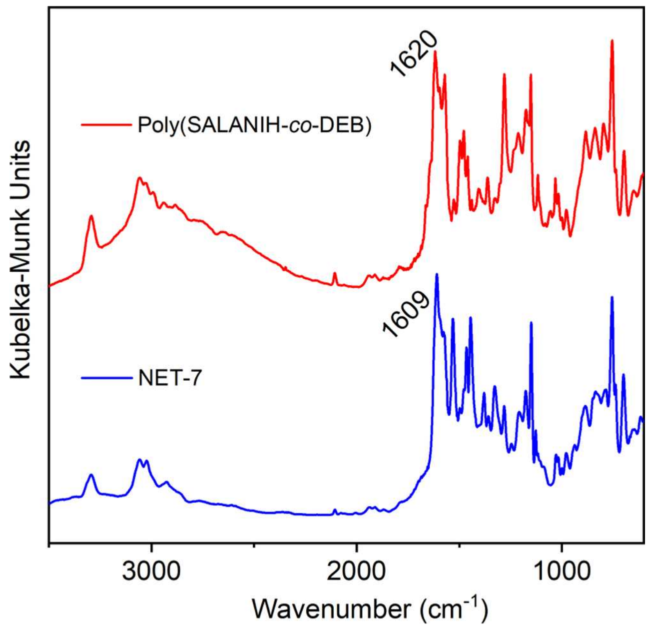

Fig. 8. FTIR spectra of parent network Poly(SALANIH-*co*-DEB) and NET-7.

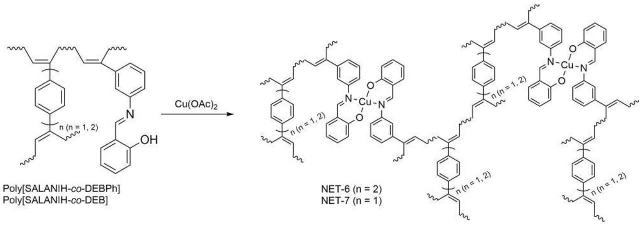

Scheme 5. Postpolymerization metalation of networks Poly(SALANIH-*co*-DEBPh) and Poly(SALANIH-*co*-DEB) by Cu^{2+} ions under the formation of NET-6 and NET-7.

copolymerization of SALANIH with DEB (molar ratio SALANIH:cross-linker = 1:1) provided totally insoluble (dichloromethane, methanol, benzene, tetrahydrofuran) networks Poly(SALANIH-*co*-DEBPh) and Poly (SALANIH-*co*-DEB), respectively (Table 2). Both networks were formed with quantitative yield.

FTIR spectra (Fig. 7 and Fig. 8) showed a strong band at 1620 cm^{-1} due to CH=N stretching that confirmed the preservation of *N*-salicylideneaniline segments in the networks. *N*-Salicylideneaniline segments were attached as pendant groups to the linear units of the networks. A weak band at 3285 cm^{-1} in FTIR spectra of both networks indicated that some monomeric units formed from DEBPh and DEB contained one unreacted ethynyl group.

Poly(SALANIH-*co*-DEBPh) was micro/mesoporous ($S_{BET} = 449$ m^2/g, $V_{mi}/V_{tot} = 0.28$, see Table 2). The N_2 adsorption/desorption isotherms on Poly(SALANIH-*co*-DEBPh) are given in **Figure S7** in the Supplementary Data. Contrary to Poly(SALANIH-*co*-DEBPh), the network Poly (SALANIH-*co*-DEB) was non-porous. Both networks contained large *N*-salicylideneaniline pendant groups and differed in the length of the cross-links. In the case of Poly(SALANIH-*co*-DEBPh), the length of the 4,4′-biphenyldiyl cross-links was close to the length of the *N*-salicylideneaniline pendant groups. This enabled the formation of pores in Poly (SALANIH-*co*-DEBPh). On the other hand, the 1,4-phenylene cross-links were significantly shorter than the *N*-salicylideneaniline pendant groups, which counteracted the pore formation in Poly(SALANIH-*co*-DEB). We reported similar findings recently for networks prepared by copolymerization of phenylacetylenes with diethynylarene cross-linkers [43].

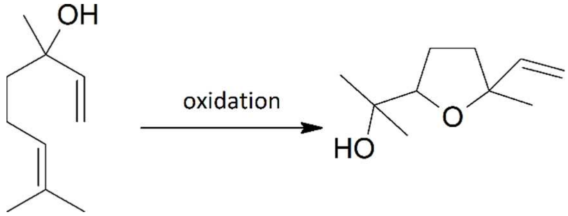

Scheme 6. Oxidation of linalool forming linalool oxide as the desired product.

Table 3
Catalytic activity in the oxidation of linalool forming linalool oxide as the desired product; 10 mg catalyst, 100 mg linalool, *tert*-butylhydroperoxide (3:1 M ratio to linalool); 3 ml dichloromethane, 60 °C, 24 h.

No.	Catalyst	Conversion of linalool (%)	A_{LO}/A_L[a]
1	None	0	0
2	Copper(II) acetate		
3	Poly(SALANIH-*co*-DEBPh)		
4	$[Cu(SALANI)_2]$	42	0.18
5	NET-4	40	0.30
6	NET-5	32	0.12
7	NET-6	48	0.40
8	NET-7	34	0.13

[a] selectivity given as the ratio of the areas of GC peaks of linalool oxide (A_{LO}) and linalool (A_L).

Dry micro/mesoporous Poly(SALANIH-*co*-DEBPh) was dispersed in tetrahydrofuran and metalated with Cu^{2+} ions using copper(II) acetate as the source of these ions (see Experimental Section). Metalation of Poly (SALANIH-*co*-DEBPh) gave an organometallic network (labeled as NET-6, see Scheme 5) with a Cu^{2+} content of 6.1 wt%. The S_{BET} of metalated NET-6 (471 m^2/g) was slightly higher than that of parent Poly(SALANIH-*co*-DEBPh) (449 m^2/g). As a result of metalation, the values of V_{tot} also increased slightly. Considering the observed positive effect of metalation on the textural parameters of NET-6, we also decided to study the metalation of the non-porous network Poly(SALANIH-*co*-DEB). Metalation of Poly(SALANIH-*co*-DEB) provided an organometallic network NET-7 (see Scheme 5). The Cu^{2+} content in NET-7 was 6.4 wt%, which confirmed that the metalation was highly effective (Table 2). Characterization of NET-7 by nitrogen adsorption/desorption isotherms

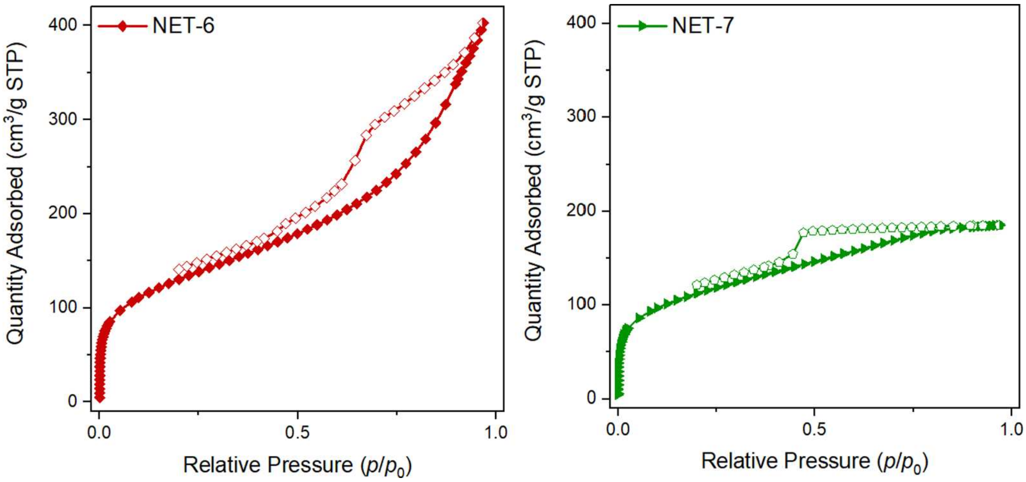

Fig. 9. N_2 adsorption (full symbols) and desorption (empty symbols) isotherms (measured at 77 K) on networks NET-6 and NET-7.

gave surprising results: the S_{BET} and V_{tot} values determined for this network were 403 m^2/g and 0.29 cm^3/g, respectively. Therefore, as a result of metalation, the non-porous Poly(SALANIH-*co*-DEB) was transformed into a porous network with a high value of the specific surface area. This finding confirmed that the Cu^{2+} ions effectively penetrated into Poly(SALANIH-*co*-DEB), where they were coordinated by *N*-salicylideneaniline pendant groups to form the [Cu(*N*-salicylideneaniline)$_2$] complex. This complex created new cross-links in the network, which led to the formation of pores. The formation of [Cu(*N*-salicylideneaniline)$_2$] cross-links in NET-6 and NET-7 was also confirmed by FTIR spectroscopy. FTIR spectra (Fig. 7, Fig. 8) showed that as a result of metalation the band of the CH=N group was shifted from a wavenumber of 1620 cm^{-1} to a wavenumber of 1609 cm^{-1} (*vide supra*).

Fig. 9 shows N_2 adsorption/desorption isotherms (77 K) on NET-6 and NET-7. The micropore diameter distributions of NET-6 and NET-7 are shown in **Figure S8** in the Supplementary Data. Both networks were micro/mesoporous, but differed in the contribution of micropores to the total pore volume, as evident from the V_{mi}/V_{tot} values, which were 0.27 for NET-6 and 0.52 for NET-7 (Table 2).

3.4. *Catalytic activity of organometallic polyacetylene networks*

Schiff base complexes of metal ions can be widely used in the field of catalysis. E. g., Schiff base complexes with Cu^{2+} ions have been described as active catalysts for oxidation/epoxidation reactions [1]. The oxidation of linalool forming linalool oxide as the desired product (Scheme 6) was used as a model reaction to evaluate the catalytic activity of prepared organometallic polyacetylene networks (NET-4, NET-5, NET-6 and NET-7; Table 3). Oxidation of linalool, like oxidation of other substrates of this type, provides a wide range of products (**Scheme S1** in the Supplementary Data), therefore enhanced selectivity towards certain product(s) is desirable.

Testing the catalytic activity of prepared organometallic polyacetylene networks showed good potential for their use as heterogeneous catalysts of linalool oxidation (Table 3). In the initial stage of the catalytic study, we excluded the catalytic activity of the non-metalated network Poly(SALANIH-*co*-DEBPh) (Table 3, No. 3) as well as the precursor of Cu^{2+} ions, copper(II) acetate (Table 3, No. 2). Likewise, no conversion of linalool has been observed in a reaction without catalyst addition (Table 3, No. 1). The above finding showed that the catalytic activity of the prepared organometallic polyacetylene networks was due to the presence of [Cu(*N*-salicylideneaniline)$_2$] segments in these networks and that traces of copper(II) acetate or polymerization catalyst [Rh(nbd)acac] did not catalyze the studied oxidation.

With NET-5 and NET-7 the conversion of linalool of about 30 % and A_{LO}/A_L of about 0.12 were achieved (Table 3, No. 6 and 8). Better values were obtained with NET-4 and NET-6 (conversion of linalool 40 and 48 %, A_{LO}/A_L 0.30 and 0.40, respectively, Table 3, No. 5 and 7). As can be seen from Table 3, NET-4 and NET-6 showed similar catalytic activity and even higher selectivity as compared to [Cu(SALANI)$_2$] applied as a homogeneous catalyst. The higher catalytic efficiency of NET-4 and NET-6 (compared to NET-5 and NET-7) may reflect the presence of longer 4,4′-biphenyldiyl co-cross-links in these networks, which could facilitate the access of substrate molecules to the catalytic active centers.

4. Conclusion

A new ethynylated organometallic Schiff base complex, [Cu(SALANI)$_2$], in which two *N*-salicylidene(3-ethynylaniline) ligands coordinated one Cu^{2+} ion, was prepared and characterized by various methods including single-crystal X-ray diffraction and ^1H NMR spectroscopy. The resolved ^1H NMR spectra were obtained (and interpreted with the help of theoretical DFT calculation) despite the paramagnetic character of the [Cu(SALANI)$_2$] complex. Copolymerization of [Cu(SALANI)$_2$] with diethynylarenes provided polyacetylene-type micro/mesoporous organometallic networks with [Cu(*N*-salicylideneaniline)$_2$] segments as network knots. Networks of this type were also prepared by post-polymerization metalation of parent networks containing *N*–salicylideneaniline segments as pendant groups. Postpolymerization metalation caused further cross-linking and increased the pore content in the networks. The new highly porous organometallic polyacetylene networks showed a specific surface area from 400 to 700 m^2/g and a Cu^{2+} content of about 6 wt%. The porous organometallic polyacetylene networks prepared by both prepolymerization and postpolymerization metalation were active as heterogeneous catalysts of oxidation of linalool to linalool oxide.

Data availability.

The raw/processed data required to reproduce these findings cannot be shared at this time as the data also forms part of an ongoing study.

CRediT authorship contribution statement

David Šorm: . **Bogdana Bashta:** . **Jan Blahut:** . **Ivana Císařová:** . **Lada Dolejšová Sekerová:** . **Eliška Vyskočilová:** Conceptualization, Methodology. **Jan Sedláček:** Conceptualization, Methodology.

Declaration of Competing Interest

The authors declare that they have no known competing financial interests or personal relationships that could have appeared to influence the work reported in this paper.

Data availability

The raw/processed data required to reproduce these findings cannot be shared at this time as the data also forms part of an ongoing study.

Acknowledgements

Financial support from the Czech Science Foundation (Project 21-02183S) and “Grant Schemes at CU“ (reg. no. CZ.02.2.69/0.0/0.0/19_073/0016935) (START/SCI/081, D. Šorm) is gratefully acknowledged.

Appendix A. Supplementary material

Supplementary data to this article can be found online at https://doi.org/10.1016/j.eurpolymj.2022.111772.

References

[1] K.C. Gupta, A.K. Sutar, Catalytic activities of Schiff base transition metal complexes, Coord. Chem. Rev. 252 (2008) 1420–1450, https://doi.org/10.1016/j.ccr.2007.09.005.

[2] W. Al Zoubi, Y.G. Ko, Schiff base complexes and their versatile applications as catalysts in oxidation of organic compounds: part I, Appl. Organomet. Chem. 31 (3) (2017) e3574.

[3] M.S. More, P.G. Joshi, Y.K. Mishra, P.K. Khanna, Metal complexes driven from Schiff bases and semicarbazones for biomedical and allied applications: a review, Mater. Today. Chem. 14 (2019) 100195. https://doi.org/https://doi.org/10.1016/j.mtchem.2019.100195.

[4] Y.-C. Yuan, M. Mellah, E. Schulz, O.R.P. David, Making Chiral Salen Complexes Work with Organocatalysts, Chem. Rev. 122 (2022) 8841–8883, https://doi.org/10.1021/acs.chemrev.1c00912.

[5] Y. Nakayama, H. Bando, Y. Sonobe, T. Fujita, Olefin polymerization behavior of bis(phenoxy-imine) Zr, Ti, and V complexes with MgCl2-based cocatalysts, J. Mol. Catal. A. Chem. 213 (2004) 141–150, https://doi.org/10.1016/j.molcata.2003.11.025.

[6] H. Kargar, R. Behjatmanesh-Ardakani, V. Torabi, M. Kashani, Z. Chavoshpour-Natanzi, Z. Kazemi, V. Mirkhani, A. Sahraei, M.N. Tahir, M. Ashfaq, K.S. Munawar, Synthesis, characterization, crystal structures, DFT, TD-DFT, molecular docking and DNA binding studies of novel copper(II) and zinc(II) complexes bearing halogenated bidentate N, O-donor Schiff base ligands, Polyhedron. 195 (2021), 114988, https://doi.org/10.1016/j.poly.2020.114988.

[7] H. Kargar, F. Aghaei-Meybodi, M.R. Elahifard, M.N. Tahir, M. Ashfaq, K. S. Munawar, Some new Cu(II) complexes containing O, N-donor Schiff base ligands derived from 4-aminoantipyrine: synthesis, characterization, crystal structure and

substitution effect on antimicrobial activity, J. Coord. Chem. 74 (2021) 1534–1549, https://doi.org/10.1080/00958972.2021.1900831.

[8] H. Kargar, F. Aghaei-Meybodi, R. Behjatmanesh-Ardakani, M.R. Elahifard, V. Torabi, M. Fallah-Mehrjardi, M.N. Tahir, M. Ashfaq, K.S. Munawar, Synthesis, crystal structure, theoretical calculation, spectroscopic and antibacterial activity studies of copper(II) complexes bearing bidentate schiff base ligands derived from 4-aminoantipyrine: Influence of substitutions on antibacterial activity, J. Mol. Struct. 1230 (2021), 129908, https://doi.org/10.1016/j.molstruc.2021.129908.

[9] H. Kargar, R. Behjatmanesh-Ardakani, V. Torabi, A. Sarvian, Z. Kazemi, Z. Chavoshpour-Natanzi, V. Mirkhani, A. Sahraei, M. Nawaz Tahir, M. Ashfaq, Novel copper(II) and zinc(II) complexes of halogenated bidentate N, O-donor Schiff base ligands: Synthesis, characterization, crystal structures, DNA binding, molecular docking, DFT and TD-DFT computational studies, Inorganica Chim. Acta. 514 (2021), 120004, https://doi.org/10.1016/j.ica.2020.120004.

[10] C. Baleizão, H. Garcia, Chiral Salen Complexes: An Overview to Recoverable and Reusable Homogeneous and Heterogeneous Catalysts, Chem. Rev. 106 (2006) 3987–4043, https://doi.org/10.1021/cr050973n.

[11] M. Abd El Sater, N. Jaber, E. Schulz, Chiral Salen Complexes for Asymmetric Heterogeneous Catalysis: Recent Examples for Recycling and Cooperativity, ChemCatChem. 11 (2019) 3662–3687, https://doi.org/10.1002/cctc.201900557.

[12] R. Ji, K. Yu, L.-L. Lou, S. Liu, Reactivity comparison of epoxidation of unfunctionalized olefins with different oxidants catalyzed by mesoporous silica supported unsymmetric chiral Mn(III) salen complexes in heterogeneous condition, J. Mol. Catal. A. Chem. 378 (2013) 7–16, https://doi.org/10.1016/j.molcata.2013.05.014.

[13] S. Roy, P. Bhanja, Sk. Safikul Islam, A. Bhaumik, Sk. Manirul Islam, A new chiral Fe (iii)–salen grafted mesoporous catalyst for enantioselective asymmetric ring opening of racemic epoxides at room temperature under solvent-free conditions, ChemComm. 52 (2016) 1871–1874. https://doi.org/10.1039/C5CC08675B.

[14] M. Halder, P. Bhanja, Md.M. Islam, A. Bhaumik, Sk.M. Islam, Chiral copper-salen complex grafted over functionalized mesoporous silica as an efficient catalyst for asymmetric Henry reactions and synthesis of the potent drug (R)-isoproterenol, New J. Chem. 42 (2018) 11896–11904. https://doi.org/10.1039/C8NJ01745J.

[15] T. Maharana, N. Nath, H.C. Pradhan, S. Mantri, A. Routaray, A.K. Sutar, Polymer-supported first-row transition metal schiff base complexes: Efficient catalysts for epoxidation of alkenes, React. Funct. Polym. 171 (2022), 105142, https://doi.org/10.1016/j.reactfunctpolym.2021.105142.

[16] C. Xing, J. Deng, R. Tan, M. Gao, P. Hao, D. Yin, D. Yin, Cooperative chiral salen TiIV catalyst supported on ionic liquid-functionalized graphene oxide accelerates asymmetric sulfoxidation in water, Catal, Sci. Technol. 7 (2017) 5944–5952, https://doi.org/10.1039/C7CY01511A.

[17] G.T. Sfrazzetto, S. Millesi, A. Pappalardo, R.M. Toscano, F.P. Ballistreri, G. A. Tomaselli, A. Gulino, Olefin epoxidation by a (salen)Mn(iii) catalyst covalently grafted on glass beads, Catal, Sci. Technol. 5 (2015) 673–679, https://doi.org/10.1039/C4CY00831F.

[18] J. Rakhtshah, A comprehensive review on the synthesis, characterization, and catalytic application of transition-metal Schiff-base complexes immobilized on magnetic Fe3O4 nanoparticles, Coord. Chem. Rev. 467 (2022), 214614, https://doi.org/10.1016/j.ccr.2022.214614.

[19] J.-S.-M. Lee, A.I. Cooper, Advances in Conjugated Microporous Polymers, Chem. Rev. 120 (2020) 2171–2214, https://doi.org/10.1021/acs.chemrev.9b00399.

[20] S. Luo, Z. Zeng, H. Wang, W. Xiong, B. Song, C. Zhou, A. Duan, X. Tan, Q. He, G. Zeng, Z. Liu, R. Xiao, Recent progress in conjugated microporous polymers for clean energy: Synthesis, modification, computer simulations, and applications, Prog. Polym. Sci. 115 (2021), 101374, https://doi.org/10.1016/j.progpolymsci.2021.101374.

[21] B. Lopez-Iglesias, F. Suárez-García, C. Aguilar-Lugo, A. González Ortega, C. Bartolomé, J.M. Martínez-Ilarduya, J.G. de la Campa, Á.E. Lozano, C. Álvarez, Microporous Polymer Networks for Carbon Capture Applications, ACS Appl. Mater. Interfaces. 10 (2018) 26195–26205, https://doi.org/10.1021/acsami.8b05854.

[22] R. Dawson, A.I. Cooper, D.J. Adams, Chemical functionalization strategies for carbon dioxide capture in microporous organic polymers, Polym. Int. 62 (2013) 345–352, https://doi.org/10.1002/pi.4407.

[23] Y. Byun, S.H. Je, S.N. Talapaneni, A. Coskun, Advances in Porous Organic Polymers for Efficient Water Capture, Chem. Eur. J. 25 (2019) 10262–10283, https://doi.org/10.1002/chem.201900940.

[24] A. Hašková, B. Bashta, Š. Titlová, J. Brus, A. Vagenknechtová, E. Vyskočilová, J. Sedláček, Microporous Hyper-Cross-Linked Polymers with High and Tuneable Content of Pyridine Units: Synthesis and Application for Reversible Sorption of Water and Carbon Dioxide, Macromol. Rapid. Commun. 42 (2021) 2100209, https://doi.org/10.1002/marc.202100209.

[25] S. Rat, A. Chavez-Sanchez, M. Jerigová, D. Cruz, M. Antonietti, Acetic Anhydride Polymerization as a Pathway to Functional Porous Organic Polymers and Their Application in Acid-Base Catalysis, ACS Appl. Polym. Mater. 3 (2021) 2588–2597, https://doi.org/10.1021/acsapm.1c00202.

[26] C.G. López-Calixto, M. Barawi, M. Gomez-Mendoza, F.E. Oropeza, F. Fresno, M. Liras, V.A. de la Peña O'Shea, Hybrids Based on BOPHY-Conjugated Porous Polymers as Photocatalysts for Hydrogen Production: Insight into the Charge Transfer Pathway, ACS Catal. 10 (2020) 9804–9812, https://doi.org/10.1021/acscatal.0c01346.

[27] S. Bhunia, B. Banerjee, A. Bhaumik, A new hypercrosslinked supermicroporous polymer, with scope for sulfonation, and its catalytic potential for the efficient synthesis of biodiesel at room temperature, ChemComm. 51 (2015) 5020–5023, https://doi.org/10.1039/C4CC09872B.

[28] L. Sekerová, M. Lhotka, E. Vyskočilová, T. Faukner, E. Slováková, J. Brus, L. Červený, J. Sedláček, Hyper-Cross-Linked Polyacetylene-Type Microporous Networks Decorated with Terminal Ethynyl Groups as Heterogeneous Acid Catalysts for Acetalization and Esterification Reactions, Chem. Eur. J. 24 (2018) 14742–14749, https://doi.org/10.1002/chem.201802432.

[29] Y. Xie, T.-T. Wang, X.-H. Liu, K. Zou, W.-Q. Deng, Capture and conversion of CO2 at ambient conditions by a conjugated microporous polymer, Nat. Commun. 4 (2013) 1960, https://doi.org/10.1038/ncomms2960.

[30] J. Li, Y. Han, H. Lin, N. Wu, Q. Li, J. Jiang, J. Zhu, Cobalt–Salen-Based Porous Ionic Polymer: The Role of Valence on Cooperative Conversion of CO2 to Cyclic Carbonate, ACS Appl. Mater. Interfaces. 12 (2020) 609–618, https://doi.org/10.1021/acsami.9b16913.

[31] Y. Zheng, X. Wang, C. Liu, B. Yu, W. Li, H. Wang, T. Sun, J. Jiang, Triptycene-supported bimetallic salen porous organic polymers for high efficiency CO2 fixation to cyclic carbonates, Inorg. Chem. Front. 8 (2021) 2880–2888, https://doi.org/10.1039/D1QI00163A.

[32] X. Sun, F. Meng, Q. Su, K. Luo, P. Ju, Z. Liu, X. Li, G. Li, Q. Wu, New catalytically active conjugated microporous polymer bearing ordered salen-Cu and porphyrin moieties for Henry reaction in aqueous solution, Dalton. Trans. 49 (2020) 13582–13587, https://doi.org/10.1039/D0DT02686G.

[33] H. Shirakawa, E.J. Louis, A.G. MacDiarmid, C.K. Chiang, A.J. Heeger, Synthesis of electrically conducting organic polymers: halogen derivatives of polyacetylene, (CH)$_x$, J. Chem. Soc. Chem. Commun. (1977) 578–580, https://doi.org/10.1039/C39770000578.

[34] T. Masuda, Substituted Polyacetylenes: Synthesis, Properties, and Functions, Polym. Rev. 57 (2017) 1–14, https://doi.org/10.1080/15583724.2016.1170701.

[35] J. Sedláček, H. Balcar, Substituted Polyacetylenes Prepared with Rh Catalysts: From Linear to Network-Type Conjugated Polymers, Polym. Rev. 57 (2017) 31–51, https://doi.org/10.1080/15583724.2016.1144207.

[36] H. Balcar, J. Sedláček, Jiří Zedník, V. Blechta, P. Kubát, Jiří Vohlídal, Polymerization of isomeric N-(4-substituted benzylidene)-4-ethynylanilines and 4-substituted N-(4-ethynylbenzylidene)anilines by transition metal catalysts: preparation and characterization of new substituted polyacetylenes with aromatic Schiff base type pendant groups, Polymer (Guildf). 42 (16) (2001) 6709–6721.

[37] J. Ren, B. Ni, H. Liu, Y. Hu, X. Zhang, T. Masuda, Postpolymerization modification based on dynamic imine chemistry for the synthesis of functional polyacetylenes, Polym. Chem. 10 (2019) 1238–1244, https://doi.org/10.1039/C8PY01793J.

[38] H. Balcar, J. Sedláček, J. Vohlídal, J. Zedník, V. Blechta, New polyacetylenes with aromatic Schiff's base pendant groups by polymerization of benzylidene-ring-substituted N-benzylidene-4-ethynylanilines with Rh-based catalysts, Macromol. Chem. Phys. 200 (1999) 2591–2596, https://doi.org/10.1002/(SICI)1521-3935(19991201)200:12<2591::AID-MACP2591>3.0.CO;2-N.

[39] C. Zhang, L. Liu, Y. Okamoto, Enantioseparation using helical polyacetylene derivatives, Trends Analyt. Chem. 123 (2020), 115762, https://doi.org/10.1016/j.trac.2019.115762.

[40] T. Kaneko, Y. Umeda, H. Jia, S. Hadano, M. Teraguchi, T. Aoki, Helix-Sense Tunability Induced by Achiral Diene Ligands in the Chiral Catalytic System for the Helix-Sense-Selective Polymerization of Achiral and Bulky Phenylacetylene Monomers, Macromolecules. 40 (2007) 7098–7102, https://doi.org/10.1021/ma0713963.

[41] E. Slováková, A. Zukal, J. Brus, H. Balcar, L. Brabec, D. Bondarev, J. Sedláček, Transition-Metal-Catalyzed Chain-Growth Polymerization of 1,4-Diethynylbenzene into Microporous Crosslinked Poly(phenylacetylene)s: the Effect of Reaction Conditions, Macromol. Chem. Phys. 215 (2014) 1855–1869, https://doi.org/10.1002/macp.201400198.

[42] L. Havelková, A. Hašková, B. Bashta, J. Brus, M. Lhotka, E. Vrbková, M. Kindl, E. Vyskočilová, J. Sedláček, Synthesis of hyper-cross-linked microporous poly(phenylacetylene)s having aldehyde and other groups and their chemisorption and physisorption ability, Eur. Polym. J. 114 (2019) 279–286, https://doi.org/10.1016/j.eurpolymj.2019.02.039.

[43] S. Stahlová, E. Slováková, P. Vaňkátová, A. Zukal, M. Kubů, J. Brus, D. Bondarev, R. Moučka, J. Sedláček, Chain-growth copolymerization of functionalized ethynylarenes with 1,4-diethynylbenzene and 4,4′-diethynylbiphenyl into conjugated porous networks, Eur. Polym. J. 67 (2015) 252–263, https://doi.org/10.1016/j.eurpolymj.2015.03.070.

[44] D. Bondarev, R. Sivkova, P. Šuly, M. Polášková, O. Krejčí, R. Křikavová, Z. Trávníček, A. Zukal, M. Kubů, J. Sedláček, Microporous conjugated polymers via homopolymerization of 2,5-diethynylthiophene, Eur. Polym. J. 92 (2017) 213–219, https://doi.org/10.1016/j.eurpolymj.2017.04.042.

[45] B. Bashta, L. Havelková, J. Sokol, J. Brus, J. Sedláček, Microporous polymers prepared from non-porous hyper-cross-linked networks by removing covalently attached template molecules, Microporous Mesoporous Mater. 330 (2022), 111636, https://doi.org/10.1016/j.micromeso.2021.111636.

[46] A.J. Pell, G. Pintacuda, C.P. Grey, Paramagnetic NMR in solution and the solid state, Prog. Nucl. Magn. Reason. Spectrosc. 111 (2019) 1–271, https://doi.org/10.1016/j.pnmrs.2018.05.001.

[47] G.M. Sheldrick, SHELXT – Integrated space-group and crystal-structure determination, Acta Crystallographica Section A. 71 (2015) 3–8, https://doi.org/10.1107/S2053273314026370.

[48] G.M. Sheldrick, Crystal structure refinement with SHELXL, Acta Crystallographica Section C. 71 (2015) 3–8, https://doi.org/10.1107/S2053229614024218.

[49] W.-K. Dong, J.-G. Duan, Y.-H. Guan, J.-Y. Shi, C.-Y. Zhao, Synthesis, crystal structure and spectroscopic behaviors of Co(II) and Cu(II) complexes with Salen-type bisoxime ligands, Inorganica Chim. Acta. 362 (2009) 1129–1134, https://doi.org/10.1016/j.ica.2008.05.028.

[50] H.M. Vinusha, S.P. Kollur, H.D. Revanasiddappa, R. Ramu, P.S. Shirahatti, M. N. Nagendra Prasad, S. Chandrashekar, M. Begum, Preparation, spectral characterization and biological applications of Schiff base ligand and its transition

metal complexes, Results. Chem. 1 (2019), 100012, https://doi.org/10.1016/j.rechem.2019.100012.

[51] I. Bertini, C. Luchinat, G. Parigi, E. Ravera, Chapter 7 - Transition metal ions: shift and relaxation, in: I. Bertini, C. Luchinat, G. Parigi, E. Ravera (Eds.), NMR of Paramagnetic Molecules (Second Edition), Elsevier, Boston, 2017, pp. 175–253, https://doi.org/https://doi.org/10.1016/B978-0-444-63436-8.00008-9.

[52] J. Blahut, L. Benda, A.L. Lejeune, K.J. Sanders, B. Burcher, E. Jeanneau, D. Proriol, L. Catita, P.-A.-R. Breuil, A.-A. Quoineaud, A.J. Pell, G. Pintacuda, Proton-detected fast-magic-angle spinning NMR of paramagnetic inorganic solids, RSC Adv. 11 (2021) 29870–29876, https://doi.org/10.1039/D1RA04110J.

[53] A. Bertarello, L. Benda, K.J. Sanders, A.J. Pell, M.J. Knight, V. Pelmenschikov, L. Gonnelli, I.C. Felli, M. Kaupp, L. Emsley, R. Pierattelli, G. Pintacuda, Picometer Resolution Structure of the Coordination Sphere in the Metal-Binding Site in a Metalloprotein by NMR, J. Am. Chem. Soc. 142 (2020) 16757–16765, https://doi.org/10.1021/jacs.0c07339.

[54] E. Slováková, M. Ješelnik, E. Žagar, J. Zedník, J. Sedláček, S. Kovačič, Chain-Growth Insertion Polymerization of 1,3-Diethynylbenzene High Internal Phase Emulsions into Reactive π-Conjugated Foams, Macromolecules. 47 (2014) 4864–4869, https://doi.org/10.1021/ma501142d.

Supplementary data for:

Porous Polymer Networks Cross-Linked by Novel Copper Schiff Base Complex: From Synthesis to Catalytic Activity

David Šorm[a*], Bogdana Bashta[a], Jan Blahut[b,c], Ivana Císařová[d], Lada Dolejšová Sekerová[e], Eliška Vyskočilová[e] and Jan Sedláček[a*]

[a]Department of Physical and Macromolecular Chemistry, Faculty of Science, Charles University, Hlavova 2030, Prague 2, 128 43, Czech Republic
[b]Department of Chemistry, Faculty of Science, Charles University, Hlavova 2030, Prague 2, 128 43, Czech Republic
[c]Institute of Organic Chemistry and Biochemistry of the Czech Academy of Sciences, Flemingovo náměstí 542/2, Prague 6, 160 00 Prague, Czech Republic
[d]Department of Inorganic Chemistry, Faculty of Science, Charles University, Hlavova 2030, Prague 2, 128 43, Czech Republic
[e]Department of Organic Technology, University of Chemistry and Technology in Prague, Technická 5, Prague 6, 166 28, Czech Republic

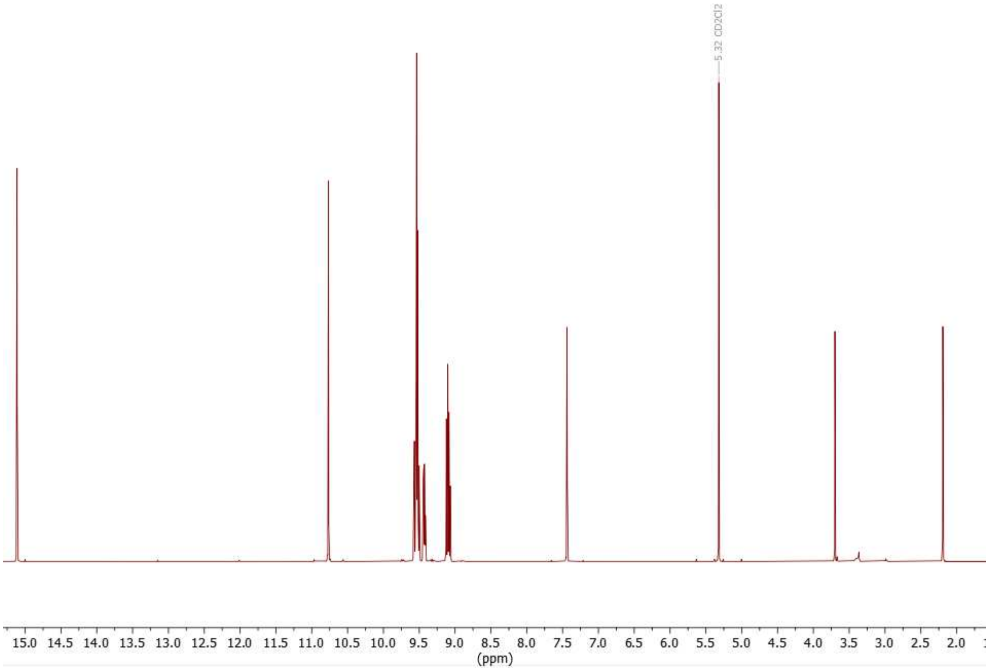

Figure S1: ^{1}H NMR spectrum of SALANIH in CD_2Cl_2.

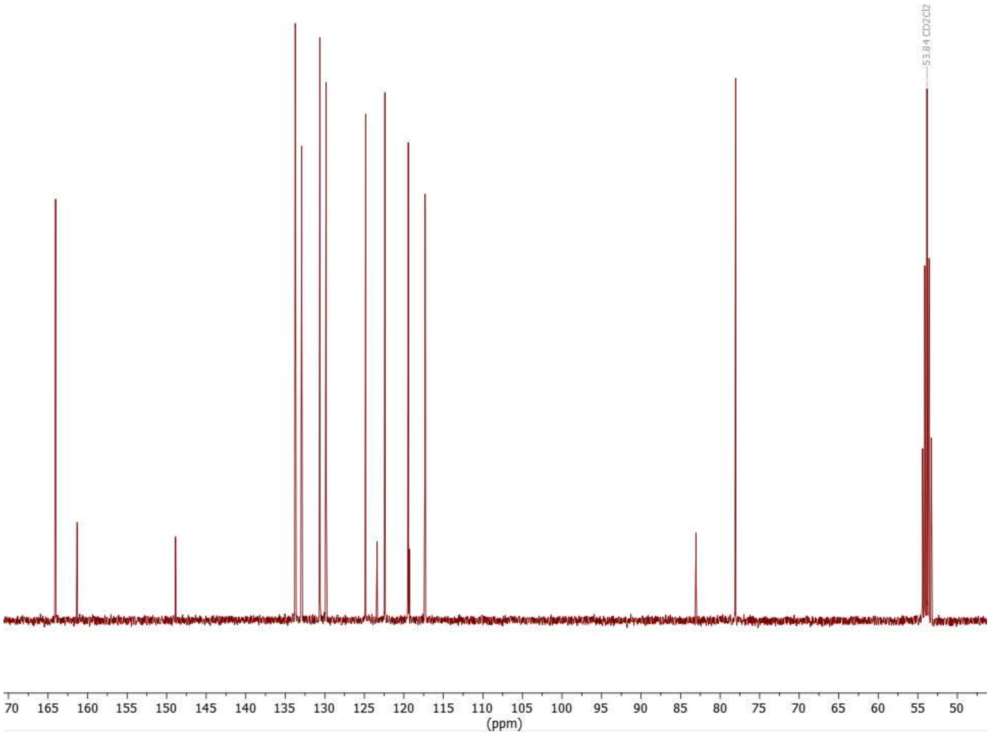

Figure S2: $^{13}C\{^1H\}$ NMR spectrum of SALANIH in CD_2Cl_2.

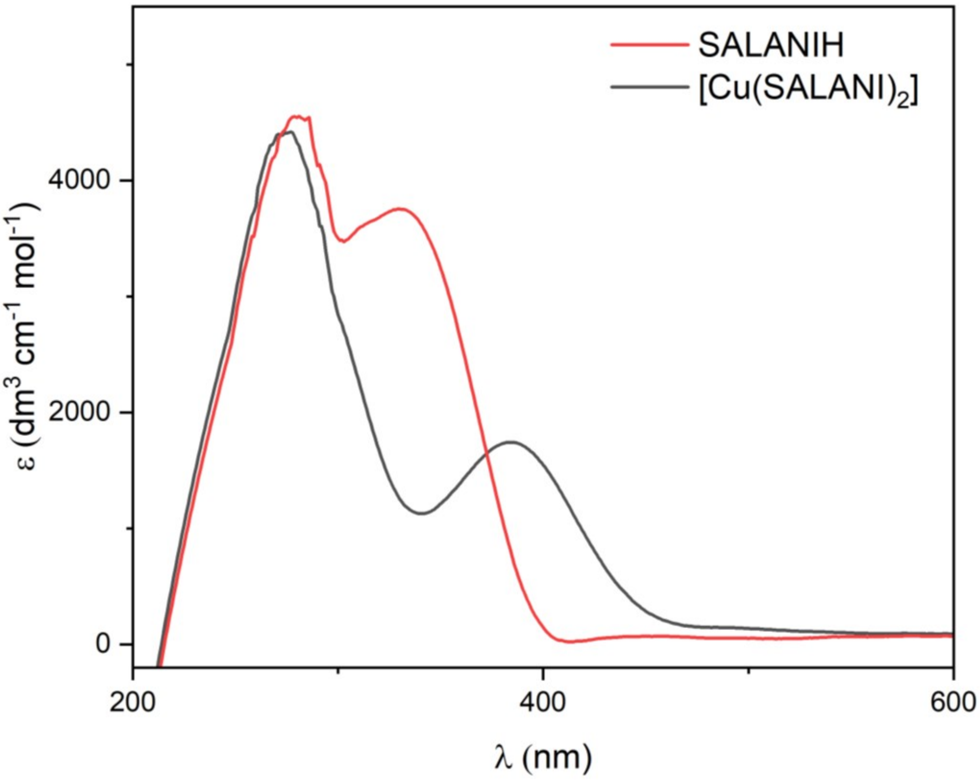

Figure S3: UV/VIS spectra of proligand/monomer SALANIH and complex $[Cu(SALANI)_2]$ in DMSO

Theoretical calculations of NMR shifts

For the purpose of NMR-shift calculation, the X-ray-based geometry of [Cu(SALANI)$_2$] was reoptimized using Turbomole 7.1 in COSMO polarization continuum model of CHCl$_3$ solution [1]. The PBE0 [2,3] functional with Grimme's D3 dispersion correction [4] and Becke–Johnson damping [5] as implemented in Turbomole were employed for geometry optimalisation using def2-TZVP base-set [6].

For resulting geometry, hyperfine-coupling constant, *g*-tensor and orbital-shielding tensor were calculated by ORCA 4.2.1 [7] using IGLO-III [8] base for NMR-active nuclei and def2-TZVPD for others. To sample accuracy of hyperfine-coupling constant, the ORCA calculation was performed using PBE DFT functional with variable admixture of Hartee-Fock exchange. Final values of NMR-shift were calculated in EPR-based formalism of Vaara [9] using self-made Matlab R2021b (MathWork) script as described in reference [10]. The temperature 300 K was used in all calculations of NMR shifts. The calculated NMR shifts of symmetry-equivalent nuclei of SALANI ligand in the [Cu(SALANI)$_2$] were averaged. Orbital-shielding tensor of tetramethylsilane as an NMR-shift reference was calculated by the same method.

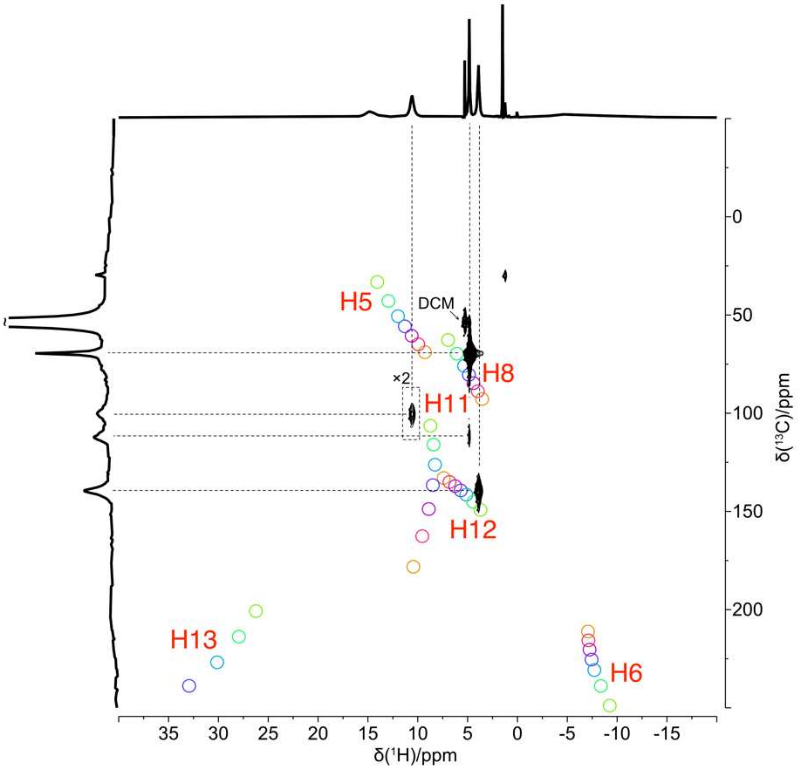

Figure S4: ^{1}H-^{13}C HSQC (14.3T, 300K) spectra of [Cu(SALANI)$_2$] (black) compared with theoretically calculated ^{1}H and ^{13}C NMR shift (rainbow-colored circles) calculated shifts using different Hartree–Fock exchange admixtures in hybrid DFT functional, ranging from 10% (orange) to 40% (green).

Table S1: DFT-optimized Cartesian coordinates (in Å) of [Cu(SALANI)$_2$] used of NMR-shift prediction.

Cu	-0.0049706	0.0004758	0.0139794	C	4.0380034	-5.876328	2.0676244
C	-4.0163178	5.8735054	-2.127681	H	4.4812241	-6.5325637	2.7809612
H	-4.4524597	6.5242908	-2.850313	O	-1.9045757	0.010444	0.0229939
O	1.8952197	-0.0099998	0.0282712	N	0.0072125	-2.0081943	0.0161692
N	-0.0143728	2.0097558	-0.0112762	C	1.7740655	-3.5672741	0.6296614
C	-1.7720834	3.5680635	-0.6528644	H	1.3320483	-3.6862688	1.6115162
H	-1.3248295	3.6729869	-1.633944	C	-2.6955768	-0.889262	0.5079086
C	2.6914224	0.8805991	-0.4650072	C	1.1966189	-2.7097087	-0.2928016
C	-1.2029897	2.7192364	0.282759	C	-3.2245621	-3.157884	1.2699099
C	3.2279081	3.1361056	-1.2595717	H	-2.8920856	-4.1772769	1.4395908
H	2.8976787	4.1529431	-1.4478953	C	-4.0373843	-0.5486349	0.787466
C	4.0349412	0.5343741	-0.7286776	H	-4.3462612	0.4713401	0.5916727
H	4.3418478	-0.4824193	-0.514053	C	-0.9951088	-2.7077048	0.437796
C	0.9924544	2.7015466	-0.4349644	H	-0.8534671	-3.7869771	0.5308509
H	0.8539713	3.7799382	-0.5425188	C	-4.5171573	-2.795139	1.5502184
C	4.5221361	2.7676993	-1.5247945	H	-5.2205796	-3.5148184	1.9492617
H	5.229072	3.480201	-1.930467	C	-4.914646	-1.4743577	1.2986728
C	4.9166614	1.4510273	-1.248632	H	-5.9356479	-1.1746148	1.510015
H	5.9389614	1.147255	-1.4475653	C	2.9458358	-4.2570609	0.3086205
C	-2.9416397	4.2678885	-0.345568	C	-2.2957028	-2.231101	0.7594597
C	2.294561	2.2184572	-0.7410697	C	3.5384343	-5.1340989	1.2620161
C	-3.5248246	5.1372195	-1.3117148	C	1.7907129	-2.5245606	-1.5365274
C	-1.8036731	2.5523401	1.5259112	H	1.3381066	-1.8406959	-2.2440638
H	-1.3576275	1.8751469	2.24384	C	3.5313529	-4.07466	-0.9446938
C	-3.5338267	4.1036609	0.9071262	H	4.4414673	-4.6068862	-1.1915343
H	-4.4422525	4.6435527	1.1433039	C	2.9481253	-3.2102923	-1.8574794
C	-2.959191	3.2475197	1.8330324	H	3.4046724	-3.0668647	-2.8294223
H	-3.4209017	3.1180733	2.8044918				

X-Ray crystallography

The crystal was grown in a dichloromethane environment by slow crystallization at constant temperature (~ 5 °C).

X-ray data for Cu(SALANI)$_2$ were collected on Bruker D8 VENTURE Kappa Duo PHOTONIII by IμS micro-focus sealed tube MoKα (λ= 0.71073) at a temperature of 120(2) K. The structure was solved by direct methods (XT[11]) and refined by full matrix least squares based on F^2 (SHELXL2018[12]) The hydrogen atoms on carbon were fixed into idealized positions (riding model) and assigned temperature factors Hiso(H) = 1.2 Ueq(pivot atom).

X-ray crystallographic data for [Cu(SALANI)$_2$] have been deposited with the Cambridge Crystallographic Data Centre (CCDC) under deposition number 2191315 and can be obtained free of charge from the Centre via its website (www.ccdc.cam.ac.uk/getstructures).

Table S2: Crystallographic data for [Cu(SALANI)$_2$].

Empirical formula	C30 H20 Cu N2 O2
Formula weight	504.02
T (K)	120
Crystal system, space group	Moniclinic, P2(1)/c (No. 14)
a, Å	12.1917(4)
b, Å	7.3353(2)
c, Å	14.3971(5)
α (°)	90
B (°)	113.404(1)
γ (°)	90
V (Å^3), Z	1181.60(7), 2
D_x (g m^{-3})	1.417
F (000)	518.0
Crystal size (mm^3)	0.33 x 0.26 x 0.09
Colour, habit	red, prism
μ (mm^{-1})	0.96
Θ_{max} (°)	27.5
hkl range	0→15, 0→9, 0→18
Diffractions collected	14 125
Diffractions unique	2 708
Diffractions observed, $I > 2\sigma(I)$	2613
Δ/σ_{max}, R	0.001, 0.023
w$R(F^2)$	0.063
GOF$_{all}$	1.09
$\Delta\rho$, e Å^{-3}	0.35; -0.35

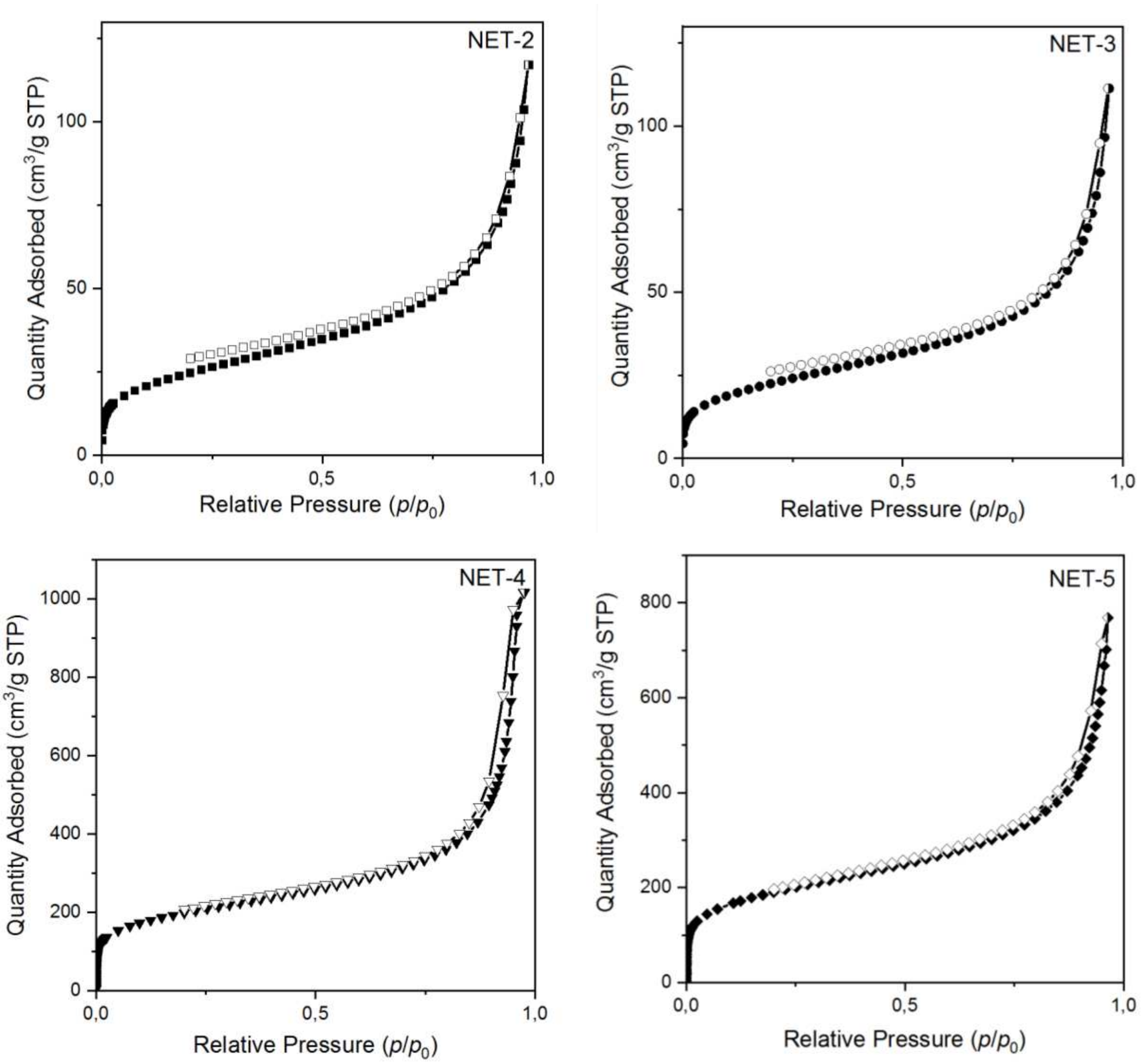

Figure S5: N_2 adsorption (full symbols) and desorption (empty symbols) isotherms (measured at 77 K) on networks NET-1, NET-2, NET-3, NET-4 and NET-5.

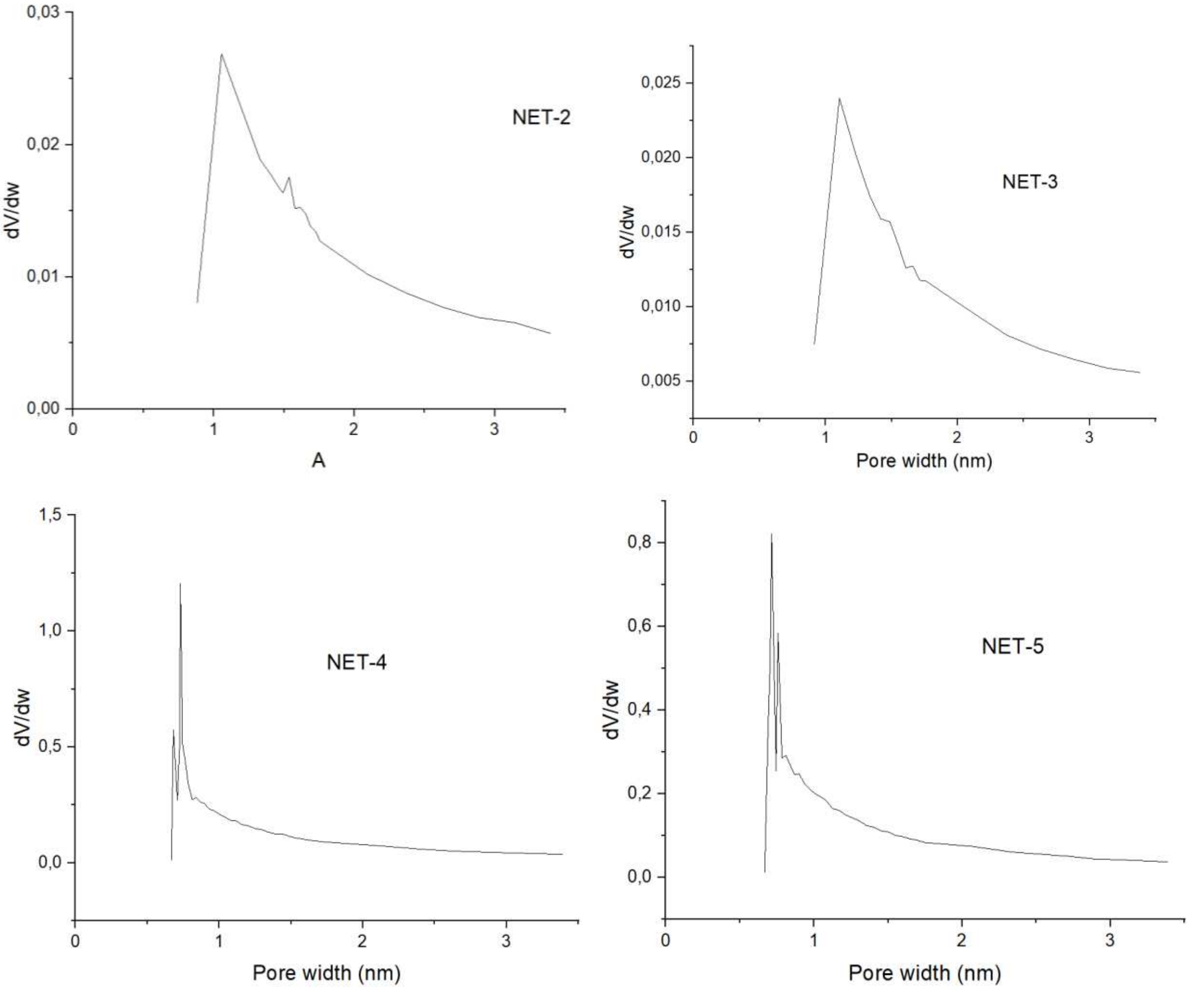

Figure S6: Micropore size distribution of NET-2, NET-3, NET-4 and NET-5.

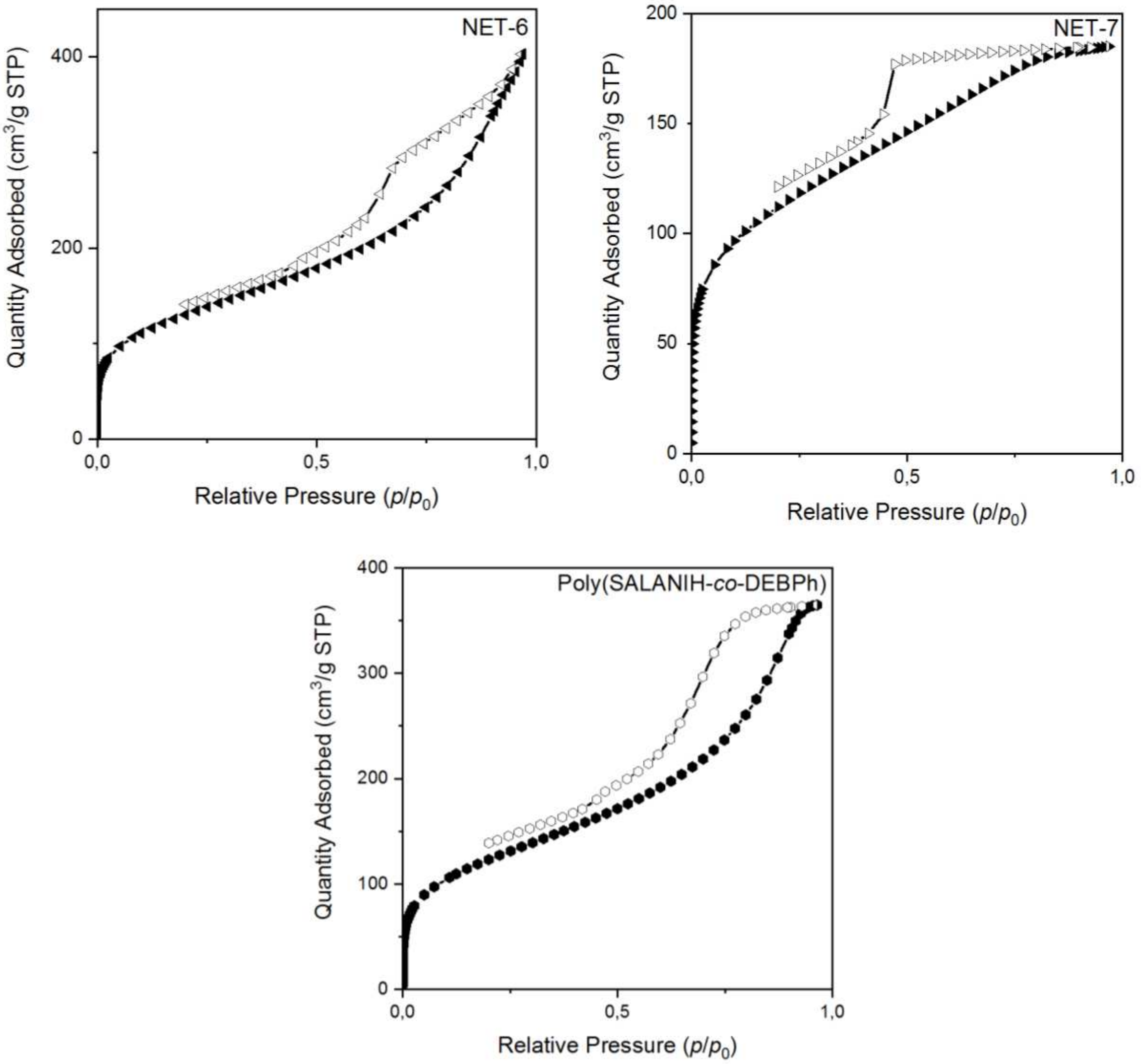

Figure S7: N_2 adsorption (full symbols) and desorption (empty symbols) isotherms (measured at 77 K) on networks NET-6, NET-7 and Poly(SALANIH-co-DEBPh).

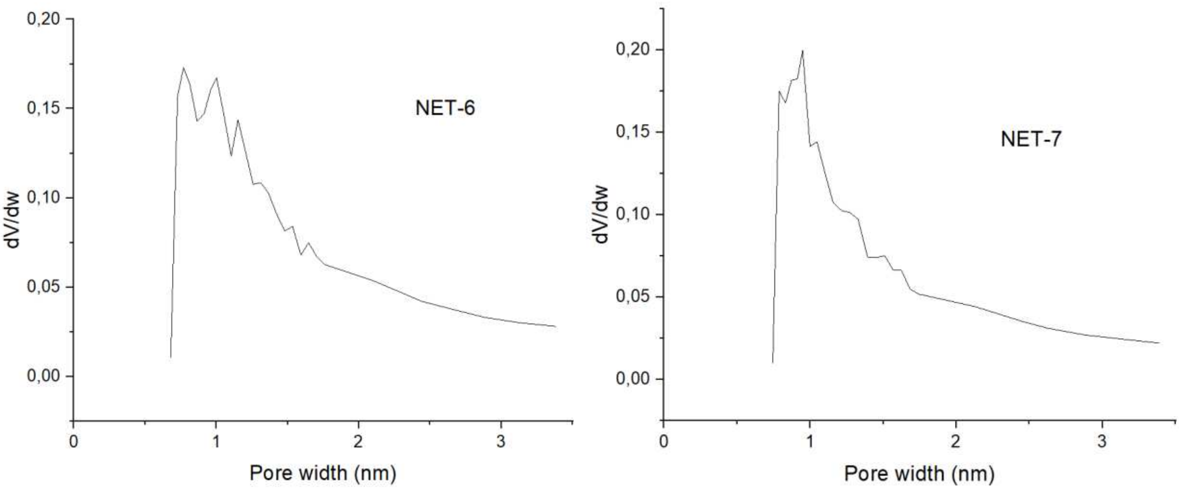

Figure S8: Micropore size distribution of NET-6 and NET-7.

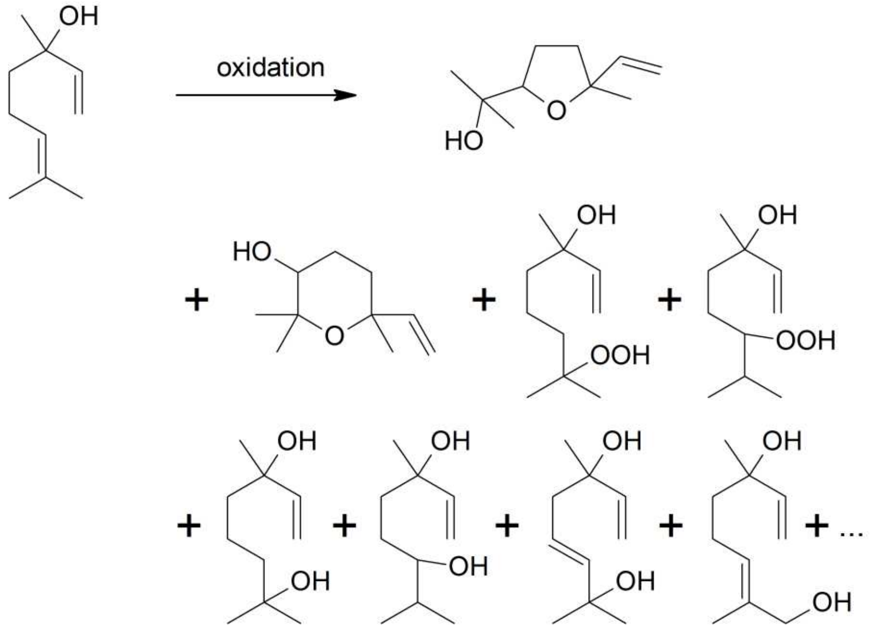

Scheme S1: Oxidation of linalool oxide – structures of identified products.

[1] A. Klamt, G. Schüürmann, COSMO: a new approach to dielectric screening in solvents with explicit expressions for the screening energy and its gradient, J. Chem. Soc., Perkin Trans. 2. (1993) 799–805. https://doi.org/10.1039/P29930000799.

[2] J.P. Perdew, M. Ernzerhof, Rationale for mixing exact exchange with density functional approximations, Phys. Rev. Lett. 77 (1996) 3865–3868.

[3] J.P. Perdew, M. Ernzerhof, K. Burke, Rationale for mixing exact exchange with density functional approximations, J. Chem. Phys. 105 (1996) 9982–9985. https://doi.org/10.1063/1.472933.

[4] S. Grimme, J. Antony, S. Ehrlich, H. Krieg, A consistent and accurate ab initio parametrization of density functional dispersion correction (DFT-D) for the 94 elements H-Pu, J. Chem. Phys. 132 (2010) 154104. https://doi.org/10.1063/1.3382344.

[5] S. Grimme, S. Ehrlich, L. Goerigk, Effect of the damping function in dispersion corrected density functional theory, J. Comput. Chem. 32 (2011) 1456–1465. https://doi.org/https://doi.org/10.1002/jcc.21759.

[6] F. Weigend, R. Ahlrichs, Balanced basis sets of split valence, triple zeta valence and quadruple zeta valence quality for H to Rn: Design and assessment of accuracy, Phys. Chem. Chem. Phys. 7 (2005) 3297–3305. https://doi.org/10.1039/B508541A.

[7] G. Bistoni, I. Polyak, M. Sparta, W. Thiel, F. Neese, Toward Accurate QM/MM Reaction Barriers with Large QM Regions Using Domain Based Pair Natural Orbital Coupled Cluster Theory, J. Chem. Theory Comput. 14 (2018) 3524–3531. https://doi.org/10.1021/acs.jctc.8b00348.

[8] W. Kutzelnigg, U. Fleischer, M. Schindler, The IGLO-Method: Ab-initio Calculation and Interpretation of NMR Chemical Shifts and Magnetic Susceptibilities, in: U. Fleischer, W. Kutzelnigg, H.-H. Limbach, G.J. Martin, M.L. Martin, M. Schindler (Eds.), Deuterium and Shift Calculation, Springer Berlin Heidelberg, Berlin, Heidelberg, 1991: pp. 165–262.

[9] J. Vaara, S.A. Rouf, J. Mareš, Magnetic Couplings in the Chemical Shift of Paramagnetic NMR, J. Chem. Theory Comput. 11 (2015) 4840–4849. https://doi.org/10.1021/acs.jctc.5b00656.

[10] J. Blahut, L. Benda, A.L. Lejeune, K.J. Sanders, B. Burcher, E. Jeanneau, D. Proriol, L. Catita, P.-A.R. Breuil, A.-A. Quoineaud, A.J. Pell, G. Pintacuda, Proton-detected fast-magic-angle spinning NMR of paramagnetic inorganic solids, RSC Adv. 11 (2021) 29870–29876. https://doi.org/10.1039/D1RA04110J.

Příloha číslo 2:

David Šorm, Jan Blahut, Bogdana Bashta, Ivana Císařová, Eva Vrbková, Eliška Vyskočilová, Jan Sedláček, Complex Isomerism Influencing the Textural Properties of Organometallic [Cu(salen)] Porous Polymers: Paramagnetic Solid-State NMR Characterization and Heterogeneous Catalysis, *Dalton Transactions*, **2024**.

Dalton Transactions

ROYAL SOCIETY OF CHEMISTRY

PAPER

View Article Online
View Journal

Cite this: DOI: 10.1039/d4dt01305k

Complex isomerism influencing the textural properties of organometallic [Cu(salen)] porous polymers: paramagnetic solid-state NMR characterization and heterogeneous catalysis†

David Šorm, *[a] Jan Blahut, *[b] Bogdana Bashta,[a] Ivana Císařová,[c] Eva Vrbková,[d] Eliška Vyskočilová[d] and Jan Sedláček[a]

Received 2nd May 2024,
Accepted 24th June 2024

DOI: 10.1039/d4dt01305k

rsc.li/dalton

Although organometallic porous polymer networks are recognized as promising heterogeneous catalysts, the relationship between ligand/monomer geometry and network parameters is usually not well understood due to the lack of atom-resolved characterization methods for the amorphous network matrix. In this work, a series of copper(II) salen-type metal complexes was synthesized, using *trans*- and *cis*-1,2-diaminocyclohexane segments, and thoroughly characterized by single-crystal X-ray diffraction and solution- and solid-state NMR spectroscopy. Terminal ethynyl groups of the complexes were then transformed into polyacetylene chains by coordination chain-growth homopolymerization, resulting in highly porous (458–655 m^2 g^{-1}) organometallic polymer networks with a copper(II) ion content of about 12 wt%. The presence of paramagnetic copper(II) moieties in these complexes and respective polymer networks required the application of tailored NMR techniques, which together with X-ray crystallography and DFT calculations of the paramagnetic NMR shifts made it possible to investigate the differences in the complex geometry in liquid, powder and crystalline form and compare it with the complex geometry in polymer networks. All prepared organometallic polymer networks were also tested as heterogeneous catalysts for styrene oxidation with uncommonly high substrate conversions and compared with their low-molecular-weight analogues. The high reusability of such heterogeneous polymer-based catalysts was also proven.

Introduction

Salen-type metal complexes, generally prepared by condensation of salicylaldehydes with various diamines followed by complexation of (usually) transition metal ions, are widely studied for their broad range of applications.[1,2] For instance, metal salen complexes are used in various bioinorganic and medicinal applications,[3] other metal salen complexes have been tested for their optical properties leading to the development of new LED systems[4–7] and multimetallic salen particles are studied for their magnetic properties.[8,9] However, by far the most widespread utilization of salen-type metal complexes is in the field of catalysis.[1,10,11] Although diverse organometallic Schiff base complexes of various compositions have been reported,[12–15] the Schiff base complexes with salen-type ligands strongly prevail in catalytic applications. A binuclear titanium(IV) salen complex was used for the cyanation of aldehydes,[16] a cobalt(II) salen complex was employed for benzoyl fluoride promoted ring opening of epoxides,[17] a chromium(III) salen complex was tested for nitroalkylation of aldehydes *via* the Henry reaction,[18] an iron(III) salen complex was applied for sulfide oxidation,[19] and a nickel(II) salen complex was utilized for Michael addition.[20] Another widely studied reaction is the addition of CO_2 to epoxides, resulting in the formation of cyclic carbonates. Various salen-type complexes with a wide spectrum of metal ions (Co, Cr, Zn, Cu, Ti, V, Sc, and Y) have been reported as effective catalysts of this addition.[21–27]

Anchoring metal salen complexes to diverse, mostly porous supporting materials leads to the "heterogenization" of these catalysts resulting in their good separability from the reaction

---

[a] *Department of Physical and Macromolecular Chemistry, Faculty of Science, Charles University, Hlavova 2030, Prague 2, 128 43, Czech Republic.*
E-mail: david.sorm@natur.cuni.cz
[b] *Institute of Organic Chemistry and Biochemistry of the Czech Academy of Sciences, Flemingovo náměstí 542/2, Prague 6, 160 00, Czech Republic.*
E-mail: blahutj89@gmail.com
[c] *Department of Inorganic Chemistry, Faculty of Science, Charles University, Hlavova 2030, Prague 2, 128 43, Czech Republic*
[d] *Department of Organic Technology, University of Chemistry and Technology Prague, Technická 5, Prague 6, 166 28, Czech Republic*

† Electronic supplementary information (ESI) available: NMR characterization, X-ray structures, UV/Vis and CD spectra, and reuse of the catalyst. CCDC 2333975 (**Cu-L1**) and 2333976 (**Cu-L3**). For ESI and crystallographic data in CIF or other electronic format see DOI: https://doi.org/10.1039/d4dt01305k

mixture, reusability, and sometimes enhanced selectivity or stability.[28,29] In numerous instances, metal salen complexes were immobilized on porous supports like nanocomposites,[30,31] polymer resins,[32] heterostructured clays,[33] graphene oxides[34] or widely used mesoporous silica-based supports.[35–39] Other complexes directly participated in the formation of porous solids while maintaining their catalytic activity. In these cases, metal salen complexes were integral components of porous materials such as covalent organic frameworks.[40] The special category is represented by metal salen complexes incorporated as building blocks of porous organic polymers (POPs).[41] POPs are a class of amorphous polymers characterized by a three-dimensional network structure possessing large specific surface areas given by permanent micro/mesoporosity. These characteristics arise from the rigidity of the network segments coupled with extensive cross-linking.[42–46] An essential study in this field was published by Xie *et al.* in 2013: a metallosalen-containing POP was prepared by Sonogashira–Hagihara cross-coupling of a dibrominated cobalt(III) salen-based complex with a 1,3,5-triethynylbenzene cross-linker and subsequently used as a CO_2 sorbent and at the same time as a heterogeneous catalyst for the transformation of CO_2 into a cyclic carbonate.[47] Subsequently, Xie *et al.* continued with a follow-up study using a POP based on a zinc (II) salen-type complex.[48] Other authors inspired by these works prepared zinc(II) or cobalt(III) salen-based POPs with ionic imidazolium groups tested as heterogeneous catalysts for CO_2 conversions.[49,50] Another catalytic utilization of metallosalen-containing POPs was in halogenation,[51] the Henry reaction[52] or epoxide hydration.[53]

The characteristics and the catalytic activity of salen-type complexes can be influenced by the type of complexed metal ion, the substituents on the salicylidene segments of the ligand, and the character of the central diamine part of the ligand. The diamine part of the ligand can significantly affect the geometry of the complex. The most common diamines used for the synthesis of salen-type metal complexes are 1,2-ethylenediamine, 1,2-phenylenediamine, and 1,2-diaminocyclohexane.[7,16–18,21,26,27] The last one can exist in two stereoisomers, *cis* and *trans*. Moreover, the *trans* stereoisomer is a chiral compound having two enantiomers with 1*S*,2*S* and 1*R*,2*R* configuration (Fig. 1). The enantiomerically pure *trans*-1,2-cyclohexanediamine can be used for the preparation of chiral salen-type metal complexes applied in enantioselective catalysis.[16–18] Many authors referring to heterogenized salen-type metal complexes containing 1,2-diaminocyclohexane used mostly the enantiomerically pure *trans* variant or a racemic mixture.[29] However, the effect of 1,2-diaminocyclohexane isomerism on the structure, texture, morphology, and catalytic properties of resulting materials was not studied. For these purposes, various NMR techniques represent powerful tools for the characterization of organometallic complexes in both solution and the solid state. Special NMR methods have proven to be effective even in the characterization of paramagnetic organometallic complexes. However, due to fast paramagnetically induced relaxations, a wide range of paramagnetically induced shifts, and their anisotropy, conventionally used pulse sequences typically fail. Thus, multiple experiments tailored to application on paramagnetic materials have been recently proposed.[54] In particular, under fast magic-angle-spinning (MAS) conditions where ^1H nuclei can be directly detected, the HSQC experiment with TEDOR recoupling provides excellent resolution and sensitivity.[55] Additionally, a ^1H–^1H correlation experiment can be conducted on paramagnetic samples, under MAS conditions, correlating either single-quantum coherence with another single-quantum coherence (SQ–SQ) or with double-quantum coherence (SQ–DQ).[56,57] The second approach is recommended for paramagnetic samples with broad resonances[58] because of their diagonal-free properties. This means that the signal on the SQ–DQ diagonal appears only when multiple chemically equivalent atoms experience mutual dipolar couplings (*e.g.* the signal on the diagonal appears for a CH_3 group but not for isolated CH). Back-to-back mixing using four phase-shifted 90° pulses in a rotor period (BaBa) is typically used for the SQ–DQ correlation in paramagnetic systems due to its extensive bandwidth.[59]

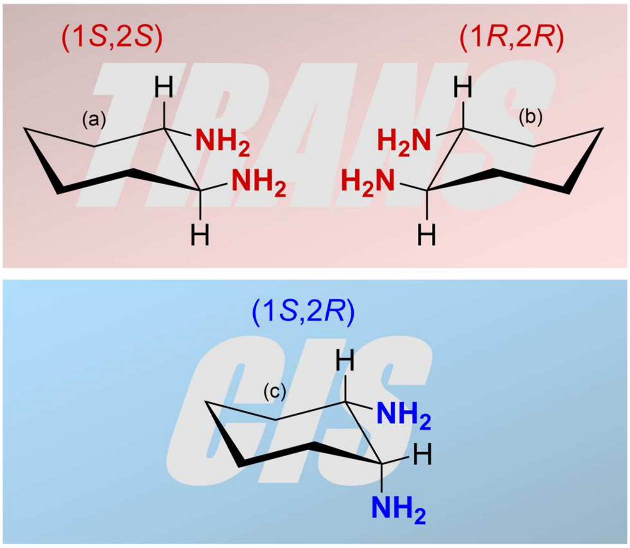

Fig. 1 Three isomers of 1,2-diaminocyclohexane: (a) (1*S*,2*S*)-1,2-diaminocyclohexane, (b) (1*R*,2*R*)-1,2-diaminocyclohexane (both *trans*) and (c) (1*S*,2*R*)-1,2-diaminocyclohexane (*cis*).

The vast majority of salen-based metal complexes containing POPs were prepared by step-growth copolymerization of the metal complexes with cross-linking comonomers.[60] This approach introduces into the structure of the POP catalytically inactive chemical blocks (derived from cross-linking molecules) the only task of which is to form a network structure and help achieve a porous texture. Herein, we propose the concept of POP-type organometallic networks prepared by direct chain-growth insertion coordination homopolymerization of copper(II) salen-type complexes without using any supportive cross-linkers. Complexes used for this homopolymerization were prepared using isomerically well-defined 1,2-diaminocyclohexane building blocks, namely (i) enantiomerically pure *trans*-(1*S*,2*S*)-1,2-diaminocyclohexane, (ii) racemic *trans*-1,2-diaminocyclohexane and (iii) *cis*-1,2-diaminocyclohexane. The influence of isomerism of 1,2-diaminocyclohexane building blocks on the structure and properties of both paramagnetic copper(II) salen-type organometallic complexes and final POPs prepared from these complexes was investigated particularly by the abovementioned advanced NMR spectroscopy based on HSQC-TEDOR and BaBa SQ-DQ correlation combined with the quantum chemical prediction of paramagnetically induced shifts.[55,61] In addition other characterization methods were used, namely, single-crystal X-ray diffraction, FTIR spectroscopy, circular dichroism, and N_2 adsorption/desorption isotherms. The combination of a facile polymerization technique with a dexterous organometallic system led to the emergence of new, thoroughly characterized heterogeneous catalysts that are highly active in the oxidation of styrene.

Experimental

Materials

Acetylacetonate(norbornadiene)rhodium(I) [Rh(nbd)acac] (>98%), (1*S*,2*S*)-1,2-diaminocyclohexane (>98%), *cis*-1,2-diaminocyclohexane (>97%), and *trans*-1,2-diaminocyclohexane (>97%) (all from TCI Europe); 5-ethynyl-2-hydroxybenzaldehyde (95%, Advanced ChemBlocks Inc.); copper(II) acetate, $Cu(OAc)_2$ (98%), *tert*-butylhydroperoxide solution (70 wt% in water), and styrene (≥99%, all from Merck); and dichloromethane (anhydrous, max. 0.001% of water, sealed under septum), ethanol (99.8%), methanol (≥99%), and dimethylformamide (99.8%) (all from VWR International) were used as obtained.

Synthesis of *N*,*N*′-bis(5-ethynylsalicylidene)-1,2-diaminocyclohexane-type ligands

Triblock ligands consisting of two blocks of 5-ethynylsalicylaldehyde binding with one block of 1,2-diaminocyclohexane were synthesized as follows: 1 mmol of specific isomer of 1,2-diaminocyclohexane, either (i) (1*S*,2*S*)-1,2-diaminocyclohexane, (ii) *trans*-1,2-diaminocyclohexane or (iii) *cis*-1,2-diaminocyclohexane was dissolved in 1.5 ml of methanol and 2.4 mmol of 5-ethynyl-2-hydroxybenzaldehyde was dissolved in 9 ml of methanol. Both solutions were mixed together in a glass vial and the reaction mixture was stirred using a magnetic stirrer for 24 hours at room temperature. After that, the solvent was evaporated. The solid product was dissolved in 10 ml of pure ethanol and purified by recrystallization in a mixture of ethanol/water (2 : 1, v/v). The crystals were separated by filtration, washed with ethanol/water (2 : 1, v/v) mixture, and dried under vacuum. Three different ligands were prepared using this synthetic process: (i) (1*S*,2*S*)-*N*,*N*′-bis(5-ethynylsalicylidene)-1,2-diaminocyclohexane (92% yield), **L1**, (ii) *trans*-*N*,*N*′-bis(5-ethynylsalicylidene)-1,2-diaminocyclohexane (81% yield), **L2** and (iii) *cis*-*N*,*N*′-bis(5-ethynylsalicylidene)-1,2-diaminocyclohexane (73% yield), **L3**.

Synthesis of [Cu(*N*,*N*′-bis(5-ethynylsalicylidene)-1,2-diaminocyclohexane)] complexes

1 mmol of respective ligand, **L1**, **L2**, or **L3** was dissolved in 24 ml of methanol and 1 mmol of copper(II) acetate was dissolved in 4 ml of distilled water. Both solutions were mixed together in a glass vial and stirred for 48 hours at room temperature. During this time a solid product was formed. The precipitate was filtered off and washed with methanol/water (6 : 1, v/v). The product was dried under vacuum. By following this procedure, three different complexes were synthesized: [Cu((1*S*,2*S*)-*N*,*N*′-bis(5-ethynylsalicylidene)-1,2-diaminocyclohexane)], **Cu-L1**, where the complex was prepared in 93% yield; [Cu(*trans*-*N*,*N*′-bis(5-ethynylsalicylidene)-1,2-diaminocyclohexane)], **Cu-L2**, where the complex was prepared in 98% yield; and [Cu(*cis*-*N*,*N*′-bis(5-ethynylsalicylidene)-1,2-diaminocyclohexane)], **Cu-L3**, where the complex was prepared in 96% yield. Crystals for single-crystal X-ray diffraction were grown by slow evaporation from a concentrated dimethylformamide solution (~4 mg ml^{-1}).

Transformation of [Cu(*N*,*N*′-bis(5-ethynylsalicylidene)-1,2-diaminocyclohexane)] complexes into organometallic polymer networks

Cu-L1, **Cu-L2**, and **Cu-L3** complexes were transformed into organometallic polymer networks by homopolymerization. The overall polymerization concentrations were 0.05 mol dm^{-3} for the monomer and 0.007 mol dm^{-3} for the polymerization initiator. A typical polymerization procedure was as follows: 0.5 mmol of monomer (**Cu-L1**, **Cu-L2**, and **Cu-L3**) was dissolved in 9 ml of dry dichloromethane and 0.07 mmol of polymerization initiator [Rh(nbd)acac] was dissolved in 1 ml of dry dichloromethane. The solution of the monomer and solution of the polymerization initiator were mixed in a crimping vial, thoroughly stirred, blown by argon, and crimped under an argon atmosphere. The polymerization proceeded at 75 °C for 5 days, after which a gel-like solid block appeared. The solid product was separated by filtration, washed with dichloromethane, and dried under vacuum. Organometallic polymer networks **P-Cu-L1**, **P-Cu-L2**, and **P-Cu-L3** were prepared in quantitative yields.

Testing the catalytic activity of organometallic polymer networks

A glass vial was loaded with an organometallic polymer network applied as a catalyst (10 mg), styrene (1 mmol), *tert*-butylhydroperoxide solution (3 mmol), and dichloromethane (3 ml). The sealed glass vial was placed onto a magnetic stirrer equipped with a heating block and the reaction mixture was heated to 60 °C for 6 hours. In the case of the reuse experiment, the reaction mixture was centrifuged, the catalyst was removed, washed with dichloromethane three times, and used in the following experiment. Samples from the reaction mixture were filtered (0.45 μm filter) and analyzed by gas chromatography coupled with mass spectrometry.

Techniques

The textural properties of the polymer networks were obtained by measuring N_2 adsorption/desorption isotherms at 77 K. The measurement itself was preceded by degassing the sample (6 h temperature ramp to 383 K) using a Micromeritics SmartVacPrep instrument. The subsequent measurement of isotherms was carried out using Triflex V4.02 apparatus (Micromeritics). Adsorption and desorption isotherms were measured from $p/p_0 = 0$ to $p/p_0 = 0.99$ ($p_0 = 101\,325$ Pa). The Brunauer, Emmett and Teller method was applied to obtain the value of the BET surface area, S_{BET}, calculated from the amount of adsorbed nitrogen in the p/p_0 range from 0.05 to 0.20, the volume of micropores, V_{mi}, was determined from the adsorbed amount of nitrogen at $p/p_0 = 0.1$ and the total pore volume, V_{tot}, was determined from the adsorbed amount of nitrogen at $p/p_0 \sim 0.99$. Pore size distribution was determined using the N_2-DFT model (calculation by density functional theory). The density of liquid nitrogen at 77 K considered for the calculation was $\rho = 0.806$ g cm^{-3}. The morphology was studied by scanning electron microscopy using a Tescan Lyra3 microscope (accelerating voltage 10 kV). The content of copper(II) ions was determined by atomic absorption spectroscopy (the samples were mineralized in a Biotage Initiator microwave reactor using $HNO_3/HClO_4$ medium and then measured using a PerkinElmer model 3110 instrument). Diffuse reflectance infrared Fourier transform spectra were recorded using a Nicolet Magna IR 760 spectrometer with KBr background. A Bruker Q-TOF Compact instrument was used to obtain spectra from high-resolution mass spectrometry (HR-MS). UV/Vis and CD spectra were recorded on a J-810 spectrometer (Jasco, Japan) using a 1 mm cuvette. Specific optical rotation, $[\alpha]$, was measured using an Anton Paar MCP 5100 polarimeter at 293 K and wavelength 589 nm in CH_2Cl_2 solution. Single-crystal X-ray diffraction was measured on a Bruker D8 VENTURE Kappa Duo PHOTONIII with an IμS micro-focus sealed tube CuKα ($\lambda = 1.54178$) source at a temperature of 120(2) K. The structures were solved by direct methods[62] and refined by full-matrix least squares based on F^2 (ref. 63). The hydrogen atoms on carbon were fixed at idealized positions (riding model) and assigned temperature factors $H_{\mathrm{iso}}(\mathrm{H}) = 1.2U_{\mathrm{eq}}$ (pivot atom). Gas chromatography-mass spectrometry was performed using a GC-2010 Plus chromatograph (Shimadzu) equipped with a non-polar DB-5MS column (35 m, 0.2 μm i.d., 0.33 μm d.f.) coupled with a GCMS-QP 2010 Ultra (Shimadzu) mass spectrometer. The ^{1}H and ^{13}C solution-state NMR spectra of diamagnetic samples were acquired using a Bruker Avance III 400 MHz spectrometer. The ^{1}H and ^{13}C solution-state NMR spectra of paramagnetic samples were acquired on a Bruker Avance III 600 MHz spectrometer by conducting a direct-excitation spin-echo-detected experiment. The chemical shift was referenced to the residual signal of the solvent.[64] The solid-state NMR spectra were acquired using a JEOL ECZ 600 MHz spectrometer with 3.2 mm and 1.0 mm HX MAS probes for slow and fast MAS experiments, respectively, both operating at room temperature (corresponding to 38–42 °C and 34–43 °C temperature gradients within the sample due to frictional heating under MAS conditions at 18 and 60 kHz in 1.0 and 3.2 mm rotors, respectively). A repetition time of 50 ms was used in all solid-state experiments and was demanded by hardware duty cycles rather than by the T_1 value of the sample, which was typically an order of magnitude faster. The chemical shift of the adamantane CH_2 peak (37.8 ppm) was used as an external secondary reference for calibration of the ^{13}C spectra. The same correction of chemical shifts was used for ^{1}H spectra as well. The 1D ^{1}H and ^{13}C NMR spectra were acquired by following a direct-excitation spin-echo-detected experiment with echo duration of a single rotor period. The nutation frequencies of the ^{1}H/^{13}C pulses of 350/290 kHz and 100/112 kHz were used with 1.0 mm and 3.2 mm probes, respectively.[65] The ^{1}H–^{13}C 2D correlation experiments were conducted using the HSQC-TEDOR experiment[55] with a dephasing and refocusing time of two rotor periods (32 μs) each. The ^{1}H SQ-DQ experiment was performed using BaBa16 mixing[59] with a dephasing and refocusing time of 128 μs each. The theoretical build-up curve of this experiment was calculated in SIMPSON.[65] The DFT-based prediction of NMR shifts was calculated for geometries optimized at the deg-TZVP/pbe0 level in Turbomole 7.1 [66] either *in vacuo* with the frozen position of non-hydrogen atoms on the position obtained from X-ray diffraction or using a COSMO/$CHCl_3$ solvent model with the released coordinates of all atoms. The NMR shifts of nucleus K were calculated by the following equation (in ppm):

$$\delta_{\mathrm{K}} = \sigma_{\mathrm{ref}} - \sigma_{\mathrm{dia,K}} + \frac{\mu_{\mathrm{B}} S(S+1)}{3k_{\mathrm{B}} T\hbar\gamma_{\mathrm{K}}} \frac{\mathrm{Tr}(\boldsymbol{g}\boldsymbol{A}_{\mathrm{K}})}{3} \cdot 1 \times 10^6$$

where orbital ("diamagnetic") shielding ($\sigma_{\mathrm{dia,K}}$), hyperfine coupling tensor ($\boldsymbol{A}_{\mathrm{K}}$) and copper(II) *g*-tensor ($\boldsymbol{g}$) were calculated (with ORCA 5.0.3)[67] using the PBE functional with a variable admixture of Hartree–Fock exchange (HFX, 10–40%) with IGLO-III (H, N, C) and def2-TZVPD (Cu, O) base sets employing the auxiliary default base set RIJK def2/JK as well. TightSCF convergence criteria were used. The orbital shielding was calculated using the GIAO method. Hyperfine-coupling-tensor calculations called for both isotropic and dipolar contributions (aiso, adip flags) giving the origin of the Fermi contact and pseudo-contact shift, respectively. The first one strongly dominates in the studied system (Tables S1 and S2†). Because the electronic spin of copper is $S = 1/2$, no zero-field splitting is present in the system. Temperature (T) was set to 298.15 K unless stated otherwise. The shielding of the reference molecule (TMS) was calculated in the same way using 25% HFX.

Results and discussion

This study deals with copper(II) organometallic complexes with various *N*,*N*′-bis(5-ethynylsalicylidene)-1,2-diaminocyclohexane (SALDAC) ligands. The SALDAC ligands were prepared by condensation of two molecules of 5-ethynyl-2-hydroxybenzaldehyde and one molecule of 1,2-diaminocyclohexane. Based on the mutual orientation of $-NH_2$ groups, 1,2-diaminocyclohexane has *trans* and *cis* stereoisomers. The *trans* isomer is a chiral compound and can exist in the form of two enantiomers with configurations on their chiral centres 1*S*,2*S* and 1*R*,2*R* (Fig. 1). For the purposes of this study, we chose (i) the enantiomerically pure *trans* isomer, (1*S*,2*S*)-1,2-diaminocyclohexane, (ii) the racemic mixture of both *trans* enantiomers, *trans*-1,2-diaminocyclohexane and (iii) the *cis* isomer, *cis*-1,2-diaminocyclohexane. These were used to synthesize **L1**, **L2**, and **L3** ligands (Scheme 1 and Fig. S1–S3†).

The SALDAC ligands have a unique combination of functional groups suitable for the complexation of divalent metal ions (two imine groups and two hydroxy groups per molecule) and for polymerization into organometallic polymer networks (two terminal ethynyl groups per molecule). All three SALDAC ligands, **L1**, **L2**, and **L3**, were prepared in yields ranging from 73 to 92% and their proposed structures were confirmed by ^1H and $^{13}C\{^1H\}$ NMR spectroscopy (Fig. S4–S9†), FTIR spectroscopy (Fig. 2) and HR-MS (see the ESI†).

Synthesis and characterization of copper(II) complexes

The prepared SALDAC ligands underwent complexation with copper(II) ions to form organometallic complexes. One molecule of **L1**, **L2**, and **L3**, respectively, reacted with one molecule of copper(II) acetate and formed **Cu-L1**, **Cu-L2**, and **Cu-L3** complexes (Scheme 1). The reaction took place at room temperature in a mixture of methanol/water (6 : 1, v/v). All three complexes were prepared in yields above 90% (see the Experimental section).

FTIR spectroscopy confirmed the successful metalation of all three ligands: bands of $-HC{=}N-$ stretching were shifted from ~1633 cm^{-1} (in the FTIR spectra of ligands **L1**, **L2**, and **L3**) to ~1628 cm^{-1} (in the FTIR spectra of complexes **Cu-L1**, **Cu-L2** and **Cu-L3**) (Fig. 2). This shift is frequently discussed and reported upon the introduction of metal ions into Schiff base-type complexes.[12,68] On the other hand, two bands proving the presence of ethynyl groups visible in the spectra of all three ligands (2100 cm^{-1} due to $-C{\equiv}C-$ stretching and 3300 cm^{-1} due to $\equiv C-H$ stretching) also remained in the spectra of all three complexes. This confirmed that ethynyl groups of **L1**, **L2**, and **L3** persist unaffected (after metalation) in **Cu-L1**, **Cu-L2**, and **Cu-L3** complexes. Interestingly, the FTIR band at 3300 cm^{-1} was split in some spectra. In FTIR spectra of ligands **L1** and **L2**, the bands of $\equiv C-H$ stretching were split by 18 cm^{-1}. This may reflect the conformational changes of **L1** and **L2** and the existence of two conformers of these *trans*-1,2-diaminocyclohexane-based ligands. The central cyclohexane segments of these conformers have both azomethine-linked substituents in either axial or equatorial positions. The conformational changes are, however, blocked once **L1** and **L2** are transformed into organometallic complexes **Cu-L1** and **Cu-L2**. In the respective organometallic complexes, both substituents on the cyclohexane ring are locked in equatorial positions (confirmed by X-ray crystallography, Fig. S12†). This is consistent with the fact that the splitting of the $\equiv C-H$ stretching band was not observed in FTIR spectra of **Cu-L1** and **Cu-L2** complexes. A different situation was observed in FTIR spectra of ligand **L3** and complex **Cu-L3**. The *cis* isomer of the 1,2-disubstituted cyclohexane segment has one substituent in the equatorial and one in the axial position and its conformational change leads to an identical molecule. This is why in the spectrum of the **L3** ligand only a single band of $\equiv C-H$ stretching from ethynyl groups was visible. The splitting of the band of the $\equiv C-H$ group in the spectrum of the **Cu-L3** complex was most probably due to the fact that two ethynylsalicylidene segments present in the **Cu-L3** complex were not identical as confirmed by the ^1H-detected HSQC-TEDOR spectrum (*vide infra*, Fig. 4).

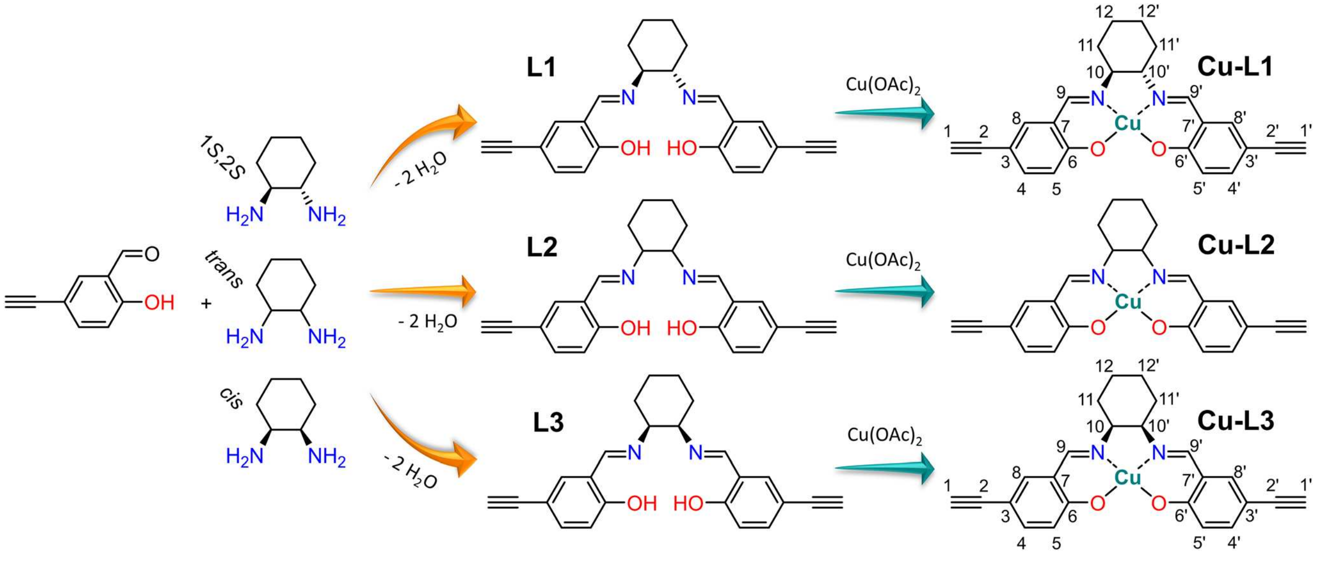

Scheme 1 Synthesis of **L1**, **L2** and **L3** ligands by condensation of 5-ethynylsalicylaldehyde with the respective 1,2-diaminocyclohexane isomer, and their subsequent metalation with copper(II) ions upon the formation of **Cu-L1**, **Cu-L2** and **Cu-L3** complexes.

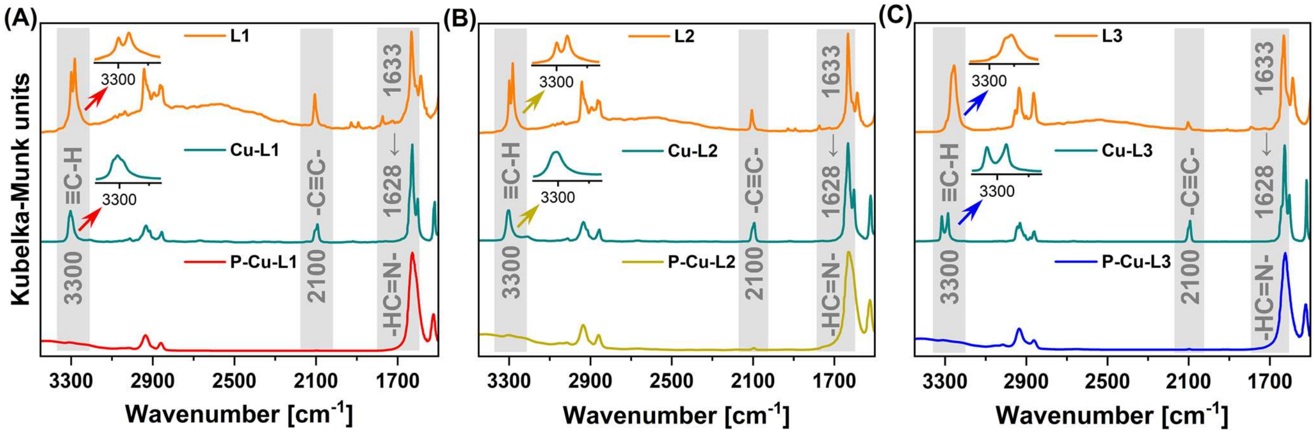

Fig. 2 FTIR spectra of series (A) **L1**, **Cu-L1** and **P-Cu-L1**, (B) **L2**, **Cu-L2** and **P-Cu-L2** and (C) **L3**, **Cu-L3** and **P-Cu-L3**.

The UV/Vis spectra of ligands **L1**, **L2**, and **L3** showed the absorption band of the n → π*/π → π* transition belonging to the –HC═N– group at λ = 333 nm. This band was red-shifted in UV/Vis spectra of complexes **Cu-L1**, **Cu-L2**, and **Cu-L3** to λ = 377 nm (measured in dichloromethane, Fig. S10†). Similar spectroscopic behaviour was reported in our previous work.[12] The circular dichroism (CD) spectra revealed the chiral character of the **L1** ligand and the **Cu-L1** complex, while no CD signals were observed for *trans* racemates **L2** and **Cu-L2** and *cis* isomers **L3** and **Cu-L3**. The CD spectra in Fig. S11† showed signals at λ = 354 nm (spectrum of **L1**) and λ = 417 nm (spectrum of **Cu-L1**) relating to the chirality associated with the cyclohexane ring. Moreover, the CD spectrum of **Cu-L1** displayed a positive Cotton effect (with a positive-to-negative CD couplet) in the range of λ = 430–680 nm, which can be ascribed to the presence of torsional helicity of the chiral organometallic complex.[69] Along with that, a significant increase of specific rotation $[\alpha]_D$ was observed when comparing **L1** and **Cu-L1** (from 19° to 632°, respectively, measured at 20 °C in dichloromethane, 1 mg ml^{-1}).

Crystals for single-crystal X-ray diffraction were grown by slow evaporation from concentrated (~4 mg ml^{-1}) dimethylformamide solutions. Crystals of enantiomerically pure *trans* **Cu-L1** (Fig. S12†) and *cis* **Cu-L3** (Fig. S13†) complexes (see more details in the ESI†) were obtained and measured. The racemic *trans* **Cu-L2** complex did not crystallize. Measured single-crystal X-ray diffraction confirmed the proposed structures (Scheme 1) of organometallic complexes. For the **Cu-L1** complex, two symmetrically independent molecules were observed (space group $P2_1$). This is a typical phenomenon for enantiomerically pure substances.[70,71] Crystals of **Cu-L3** were also formed by two molecules. Conformational changes of the *cis*-**L3** ligand (from configuration 1*S*,2*R* to configuration 1*R*,2*S* and *vice versa*) were locked once the ligand was transformed into organometallic complex **Cu-L3**. This led to a racemic mixture of two centrosymmetric *cis* complexes (space group $P2_1/n$). The complexes differed in configuration on chiral centres (1*S*,2*R* *vs.* 1*R*,2*S*). Similar conformational locking of (non-metalated) *cis*-1,2-diaminocyclohexane-based compounds was described by van Beek and Samoshin.[72] The structures of complexes **Cu-L1** and **Cu-L3** obtained from X-ray diffraction showed in both cases good steric accessibility of terminal ethynyl groups, promising for their efficient polymerization, together with good steric accessibility of coordinated copper(II) ions for substrate molecules, promising for catalytic application. The coplanarity of the cyclohexane ring within the **Cu-L1** complex with the phenyl rings resulted in a reduced spatial occupancy of the entire complex in comparison with the **Cu-L3** complex, in which the cyclohexane ring exhibited an out-of-plane orientation relative to the phenyl rings.

NMR spectroscopy provides a sensitive tool for comparison of organometallic complexes in the liquid state, in the solid form, as well as, within the polymer network. For the purpose of this advanced NMR analysis, only enantiomerically pure *trans* isomer **Cu-L1** and *cis* isomer **Cu-L3** were studied. The solution-state ^{1}H spectrum of **Cu-L1** (Fig. 3B) exhibited typical features of the paramagnetic compounds: we observed four distinct signals between 25 and −6.6 ppm with linewidths ranging from 22 Hz to 7.5 kHz and extremely short T_1 relaxation times of ~2 ms (global $T_1(^1H)$ at 70 kHz MAS). Surprisingly, the ^{1}H spectrum of solid **Cu-L1** measured under fast MAS conditions (70 kHz, Fig. 3A) presents a similar resolution to the spectrum in solution with similar NMR shifts of all four observed signals. The structure of **Cu-L1** therefore remained similar upon dissolution in aprotic solvents. Under the conditions of fast MAS, an irregular line-shape of resonance at 25 ppm was observed indicating the overlap of several lines (in contrast to the spectra at slower MAS; see Fig. S14†). Additionally, two bands between 10 and 0 ppm were composed of several overlapping signals. Similarly, the comparison between the solid-state ^{1}H spectrum of **Cu-L3** with its solution-state spectra indicates a similar structure in both phases (Fig. S15†). However, extensive signal overlap of multiple signals occurred in this case in the region between 15 and −10 ppm.

Fortunately, signal overlaps were efficiently resolved using ^{1}H-detected 2D ^{1}H–^{13}C correlation experiments (HSQC-TEDOR).[55] This 2D experiment can be readily

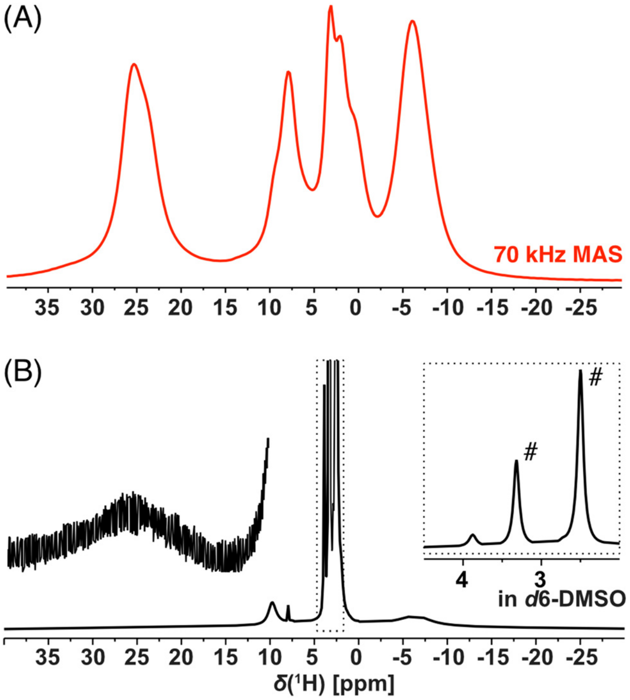

Fig. 3 ^{1}H NMR spectra (14.09 T) of **Cu-L1** acquired by the spin-echo experiment (A) on a solid-state powder sample under 70 kHz MAS conditions and (B) on the d$_6$-DMSO solution (# indicate solvent and residual water signals).

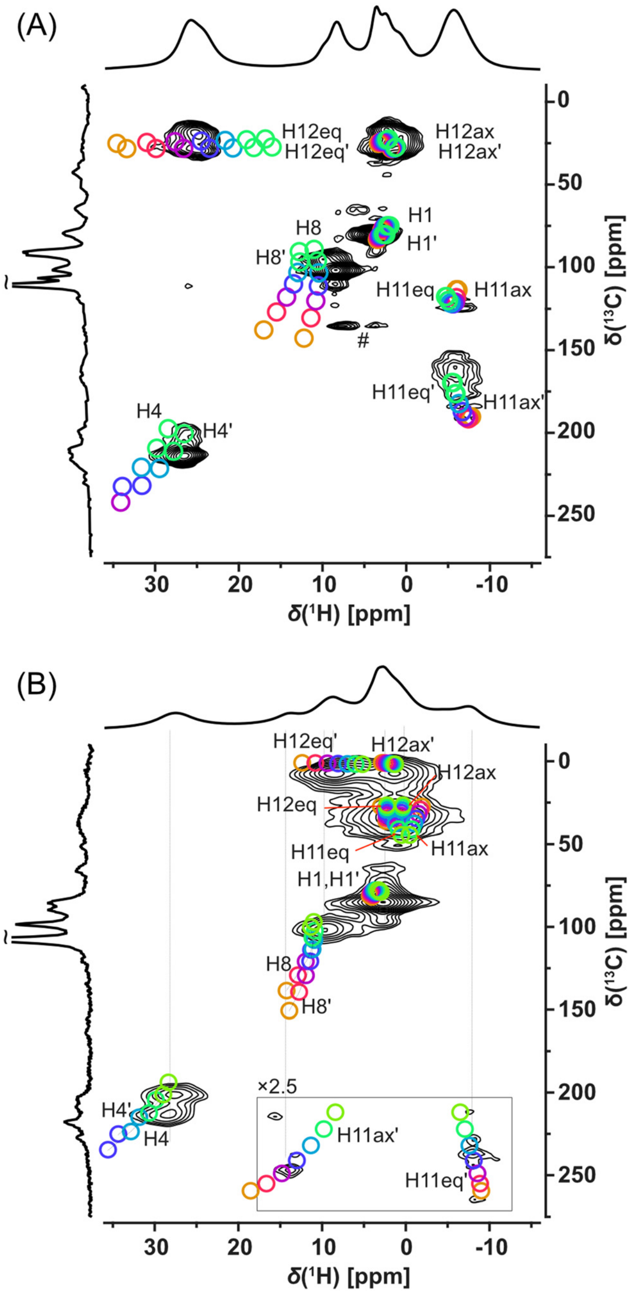

Fig. 4 ^{1}H-detected HSQC-TEDOR spectra of (A) **Cu-L1** and (B) **Cu-L3** acquired at 62.5 kHz MAS and 14.09 T using a 1 mm rotor (black) compared with calculated ^{1}H–^{13}C signals using a variable Hartree–Fock exchange admixture for hyperfine coupling (from orange 10% to green 40% in 5% steps) for X-ray-based structure with reoptimized hydrogen position (# indicated an on-resonance T_1 artefact).

measured (typically after approximately 4 h of experimental time) in the ^{13}C natural abundance even for paramagnetic compounds (Fig. 4). This excellent sensitivity is mainly caused by a short T_1 relaxation allowing short repetition time (here 55 ms due to limited hardware duty cycle) as well as strong ^{1}H–^{13}C dipolar interaction, which allows extremely short dephasing and rephasing times for the coherence transfer (2 × rotor period = 32 μs each). Extensive improvement of resolution is, for example, demonstrated in the signal at 25 ppm in the ^{1}H spectrum of **Cu-L1**, which was clearly separated into the correlation of two CH pairs with very distinct ^{13}C shifts (225 and 25 ppm).

Additionally, these correlation experiments can be readily compared with DFT calculations providing unambiguous spectral assignment. Signals of all inequivalent CH pairs were detected for **Cu-L1**, apart from signals of the CH pair number 5, 9, and 10, which were too close to the copper(II) ion and were not detected due to fast T_2 relaxation and extreme ^{1}H and/or ^{13}C NMR shifts predicted by calculation (Fig. S16 and S17;† see numbering of atoms in Scheme 1). Interestingly, the signals of equatorial and axial H12 appear at very distinct NMR shifts of 25 ppm and 3 ppm, respectively, which indicate the stronger contact shift for H12eq located in-plane with the paramagnetic copper(II) ion. The resolution was also extensively enhanced for the **Cu-L3** sample using a 2D HSQC-TEDOR experiment (Fig. 4B).

Due to crystal packing, molecule **Cu-L1** is not perfectly C_2-symmetric in the solid state. This is most pronounced on different C11 and C11′ shifts but also other CH correlations are slightly split into pairs of overlapping signals. Compared to **Cu-L1** with *trans* conformation, the *cis* conformation of the cyclohexane ring in **Cu-L3** results in a much stronger deviation from the C_2 symmetry of the complex, which was particularly emphasized by a distinct ^{13}C NMR shift of C11 and C11′ (50 and 250 ppm). The difference in the ^{13}C shift was also observable for C12 and C12′ as well as for C4 and C4′. In all cases, the calculated differences between NMR shifts of the primed and non-primed C–H pairs corresponded well to the experimental one.

Here, we recommend critical precautions during the analysis of the calculated NMR shift. The hyperfine coupling constant (which is the most critical parameter for paramagnetic-shift calculations in a system with a dominant Fermi-contact shift mechanism, as in this case, see Tables S1 and S2†) changes significantly with the variation of the exact Hartree–Fock exchange (HFX) admixture to the used density functional.[55,73] On the one hand, for 10% HFX, the difference in the NMR shift of the C8 and C8′ was predicted to be almost 12 ppm while for 40% HFX the predicted difference was only about 3 ppm. The absence of splitting of the C8 signal in the experimental 2D spectra indicates that the admixture with higher HFX content provided a more realistic prediction for this nucleus. Also, the absolute value of the NMR shift was in better agreement with the admixture having the higher HFX content. On the other hand, the ^{1}H shift of the equatorial H12 was best predicted with HFX about 25%. Therefore, several calculations in a range of HFX concentrations are recommended for appropriate sampling of this inaccuracy as indicated by our "rainbow plots" shown in Fig. 4.

The excellent resolution of the ^{1}H spectra and completed assignment allowed us to fully understand the homonuclear ^{1}H–^{1}H SQ–DQ correlation spectra as well (Fig. 5 and Fig. S20†). The efficiency of double-quantum build-up and subsequent intensity of the observed signals of the SQ–DQ correlation depends on the strength of a dipolar coupling between correlated nuclei. The dipolar coupling decreases with the 3rd power of interatomic distance and therefore, for a given mixing time, the intensity of the SQ–DQ correlation signal steeply decreases with distance (inset of Fig. 5). Using a short mixing time (128 µs) the intensity of the SQ–DQ correlation signal for atoms separated by more than 5 Å decreases to below 10% of its maximal value making them effectively undetectable. However, experimental data show multiple correlations between ^{1}H atoms separated by a distance longer than 5 Å within the **Cu-L1** molecule – in an extreme case 17.9 Å for H1–H1′ correlation (intramolecular distances indicated as black values in Fig. 5). Observed correlations, therefore, indicate dense crystal packing of **Cu-L1** and subsequent *inter*-molecular contacts. This is in excellent agreement with the crystal structure detected by X-ray diffraction: close intermolecular proximities of involved ^{1}H nuclei smaller than 5 Å were detected in the crystal structure for all observed SQ–DQ correlations (minimal distances indicated as red values in Fig. 5).

The ^{1}H–^{1}H SQ–DQ correlation spectrum was also acquired for **Cu-L3** (Fig. S20†) where, however, stronger signal overlaps hid most of the potential fine detail. The only two well-resolved correlations that indicated crystal packing *via* intermolecular proximities were between H4–H11ax′ and H4–H11eq′, which corresponded to distances of 2.4 and 3.5 Å in the single-crystal X-ray structure.

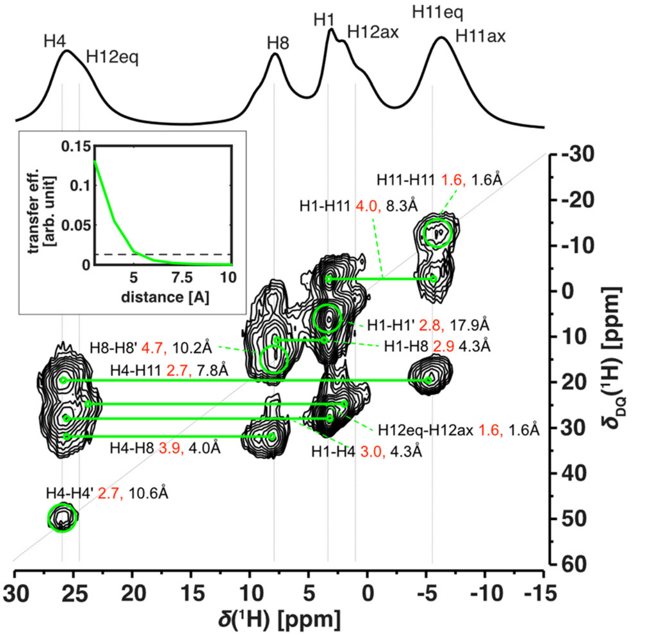

Fig. 5 Homonuclear BaBa16 ^{1}H single–double quantum (SQ–DQ) correlation of **Cu-L1** (62.5 kHz MAS, 14.09 T). Green lines and circles indicate assigned correlations. Shown distances correspond to the shortest distance found in the crystal structure (red) and the shortest intramolecular distance (black). The inset shows the simulated efficiency of the BaBa16 recoupling sequence with a recoupling time of 128 µs (similar to the experiment) as a function of ^{1}H–^{1}H distance with an indicated level of 10% efficiency (dashed line).

Altogether, we may conclude that ^{1}H-detected solid-state NMR uniquely matches the structures in the single-crystal, in the powder sample, and in solution showing that the structure of these studied copper(II) complexes remained unchanged. This was also in line with calculation. The predicted NMR shifts of the structure fully optimized in the PCM solvent model match well with the predicted NMR shifts for the single-crystal structure (with reoptimized ^{1}H positions), apart from subtle effects caused by the decrease of local symmetry due to crystal packing. This is true for both **Cu-L1** and **Cu-L3** (Fig. S16 and S18†).

Transformation of copper(II) complexes into organometallic polymer networks

Organometallic complexes **Cu-L1**, **Cu-L2**, and **Cu-L3** were polymerized (in a chain-growth manner) by the transformation of their terminal ethynyl groups into polyacetylene main chains.[45,46] The polymerizations were initiated by [Rh(nbd)acac] at 75 °C.[74] As all three organometallic complexes had two polymerizable terminal ethynyl groups per molecule, their homopolymerization led to the formation of completely insoluble organometallic polymer networks **P-Cu-L1**, **P-Cu-L2**, and **P-Cu-L3** (Scheme 2, all networks were prepared in quantitative yields).

All three networks contained almost the same amount of copper(II) ions, ranging from 12.0 to 12.2 wt% (Table 1). The

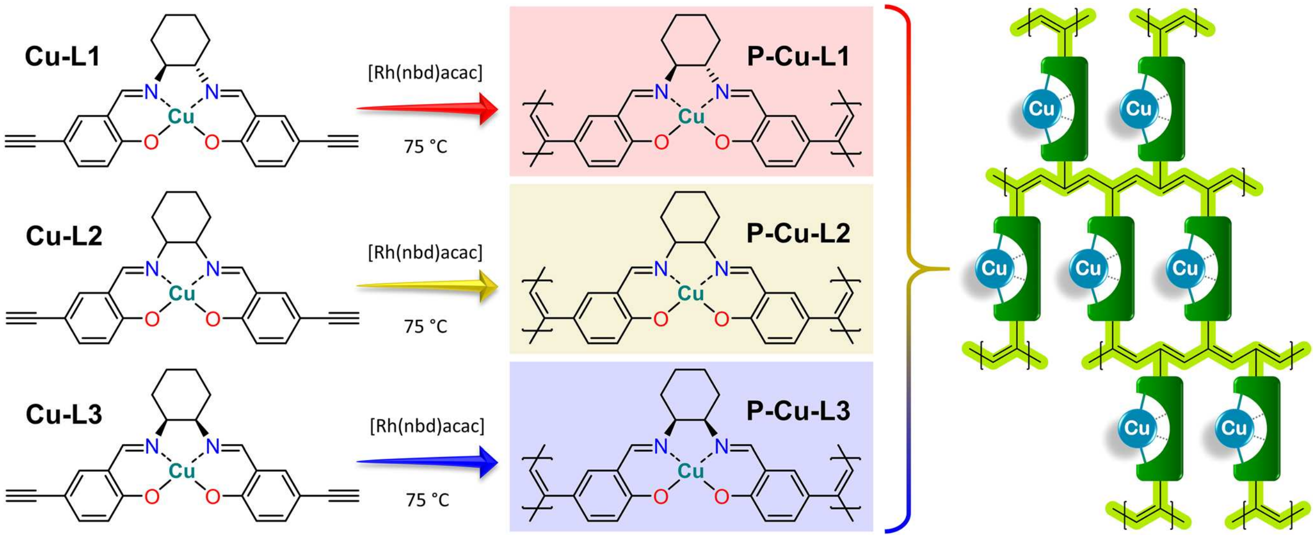

Scheme 2 Homopolymerization of **Cu-L1**, **Cu-L2** and **Cu-L3** complexes leading to organometallic polymer networks **P-Cu-L1**, **P-Cu-L2** and **P-Cu-L3** and schematic representation of the incorporation of organometallic complexes as cross-linking-type building blocks into networks with conjugated polyene chains.

Table 1 Networks **P-Cu-L1**, **P-Cu-L2**, and **P-Cu-L3**: content of copper (II) ions; BET areas, S_{BET}; micropore volume, V_{mi}; and total pore volume, V_{tot}

Network	SALDAC isomer	Copper content [wt%]	S_{BET} [m^2 g^{-1}]	V_{mi} [cm^3 g^{-1}]	V_{tot} [cm^3 g^{-1}]	V_{mi}/V_{tot}
P-Cu-L1	*trans* enantiomer	12.2	522	0.22	0.39	0.56
P-Cu-L2	*trans* racemate	12.1	458	0.19	0.34	0.57
P-Cu-L3	*cis*	12.0	655	0.26	0.71	0.36

FTIR spectra in Fig. 2 showed that roughly all terminal ethynyl groups of **Cu-L1**, **Cu-L2**, and **Cu-L3** complexes were transformed upon polymerization into polymer networks **P-Cu-L1**, **P-Cu-L2** and **P-Cu-L3** (the bands at 3300 cm^{-1} and 2100 cm^{-1} were no more visible in their spectra). The band of –HC=N– stretching at ~1628 cm^{-1} from spectra of complexes remained at the same position in the spectra of all three polymer networks proving that the organometallic cores persist unaffected during polymerization. The polymer networks **P-Cu-L1** and **P-Cu-L3** were also studied by solid-state NMR. On comparing the ^1H–^{13}C correlation spectra of the polymer networks and related monomeric organometallic complexes (Fig. 6), the broadening of signals typical of the transformation of microcrystalline monomers into polymers can be seen. Additionally, the narrow signal of the acetylenic CH1 disappeared and was replaced by a broad resonance at 125 and 6.5 ppm in ^{13}C and ^1H spectra, respectively, which correspond to the vinylene groups in the polymer chains. The position of the most shifted CH4 resonance was the same in the spectra of complexes and final networks. This was another confirmation that the structure of the copper coordination environment remained unaltered upon polymerization.

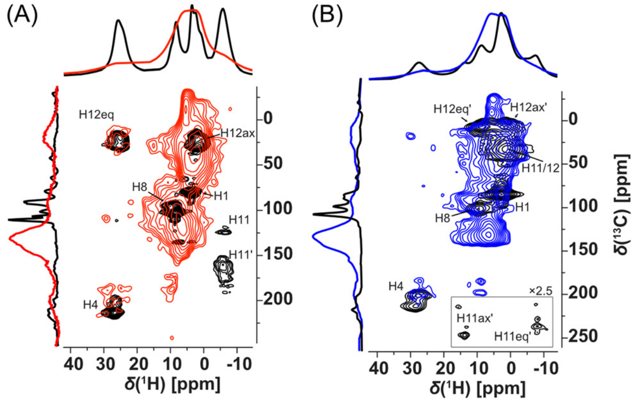

Fig. 6 ^1H-detected HSQC-TEDOR spectra (62.5 kHz MAS, 14.09 T) of (A) **Cu-L1** (black) *vs.* **P-Cu-L1** (red) and (B) **Cu-L3** (black) *vs.* **P-Cu-L3** (blue). 1D horizontal and vertical traces show direct-excitation spin-echo detected ^1H and ^{13}C spectra acquired at 62.5 and 18 kHz, respectively.

The results of FTIR and solid-state NMR spectroscopies agreed with the proposed structures (Scheme 2) of organometallic polymer networks **P-Cu-L1**, **P-Cu-L2**, and **P-Cu-L3**. All networks were composed exclusively of respective *N*,*N*′-bis(5-ethynylsalicylidene)-1,2-diaminocyclohexane ligands coordinating copper(II) ions (one ligand coordinated one metal ion) and polyacetylene chains.

Despite the fact that **P-Cu-L1**, **P-Cu-L2**, and **P-Cu-L3** were cross-linked exclusively by metalated SALDAC segments (and no other cross-linker was used for the preparation), all these networks exhibited a micro/mesoporous texture and quite high BET areas (458–655 m^2 g^{-1}, Table 1). It is thus evident that organometallic segments not only introduced functionality into the networks but also served as rigid building blocks contributing to the formation of porous textures. The rigidity of the metalated copper(II) complex was essential to achieve porous textures with large BET areas. To prove this fact, we homopolymerized the non-metalated ligands, **L1**, **L2**, and **L3**, in the same way. Homopolymerization provided networks in quantitative yields, which were, however, non-porous.

Remarkably, the textural properties differed depending on the used SALDAC isomer. Networks **P-Cu-L1** and **P-Cu-L2** built from enantiomerically pure **Cu-L1** and racemic **Cu-L2** segments (both with *trans* configurations) showed BET areas of 522 and 458 $m^2 g^{-1}$, respectively. The N_2 adsorption/desorption isotherms of both networks shown in Fig. 7 were similar with a pronounced N_2 adsorption at low relative pressures ($p/p_0 < 0.1$, filling of micropores), followed by only a small increase in the adsorbed amount of N_2 as the relative pressure reached $p/p_0 \sim 1$. This shape of the N_2 adsorption/desorption isotherms is characteristic for prevailingly microporous materials with a low content of mesopores. The characteristics of N_2-DFT pore size distribution curves shown in Fig. 7 confirmed this finding, pointing to a high content of micropores (pore width < 2 nm) and a low contribution of mesopores (pore width > 2 nm) to the total porosity. In contrast, network **P-Cu-L3** built from a segment with *cis* configuration showed a larger BET area (655 $m^2 g^{-1}$). The N_2 adsorption/desorption isotherms on **P-Cu-L3** (Fig. 7) again showed a pronounced N_2 adsorption in the $p/p_0 < 0.1$ region, which was followed by a continuous N_2 trapping up to a relative pressure of $p/p_0 \sim 1$. Isotherms of this type are typical for micro/mesoporous materials with a significant contribution of mesopores. This was in good accordance with the N_2-DFT pore size distribution shown in Fig. 7, indicating an increased contribution of mesopores to the total porosity. The differences in textural properties between networks with *trans* configuration, **P-Cu-L1** and **P-Cu-L2**, and the network with *cis* configuration, **P-Cu-L3**, are noticeable also from total pore volumes (Fig. 7 and Table 1). Whilst the volume of micropores, V_{mi}, differed only slightly (0.19–0.26 $cm^3 g^{-1}$), the total pore volume, V_{tot}, showed more fundamental differences. Networks **P-Cu-L1** and **P-Cu-L2** had similar V_{tot} values (0.39 and 0.34 $cm^3 g^{-1}$, respectively). A much higher V_{tot} was observed for network **P-Cu-L3** (0.71 $cm^3 g^{-1}$). The explanation for these disparities in textural properties can be based on single-crystal X-ray structures of organometallic complexes (Fig. S12 and S13†). We presume (based on FTIR and NMR results) that the geometries of organometallic segments remain unaffected by polymerization. The geometry of organometallic complex **Cu-L1** detected by single-crystal X-ray diffraction is more planar and may result in a tighter packing of organometallic segments in the resulting polymer network, which does not mediate the formation of larger pores (mesopores) to such an extent. This organometallic segment and its racemic mixture are built into networks **P-Cu-L1** and **P-Cu-L2**. In contrast, organometallic complex **Cu-L3** showed a spatially more demanding geometry, which does not allow such a tight arrangement of organometallic segments, resulting in the formation of a wider range of pore sizes (high extent of micropores and mesopores) in network **P-Cu-L3**.

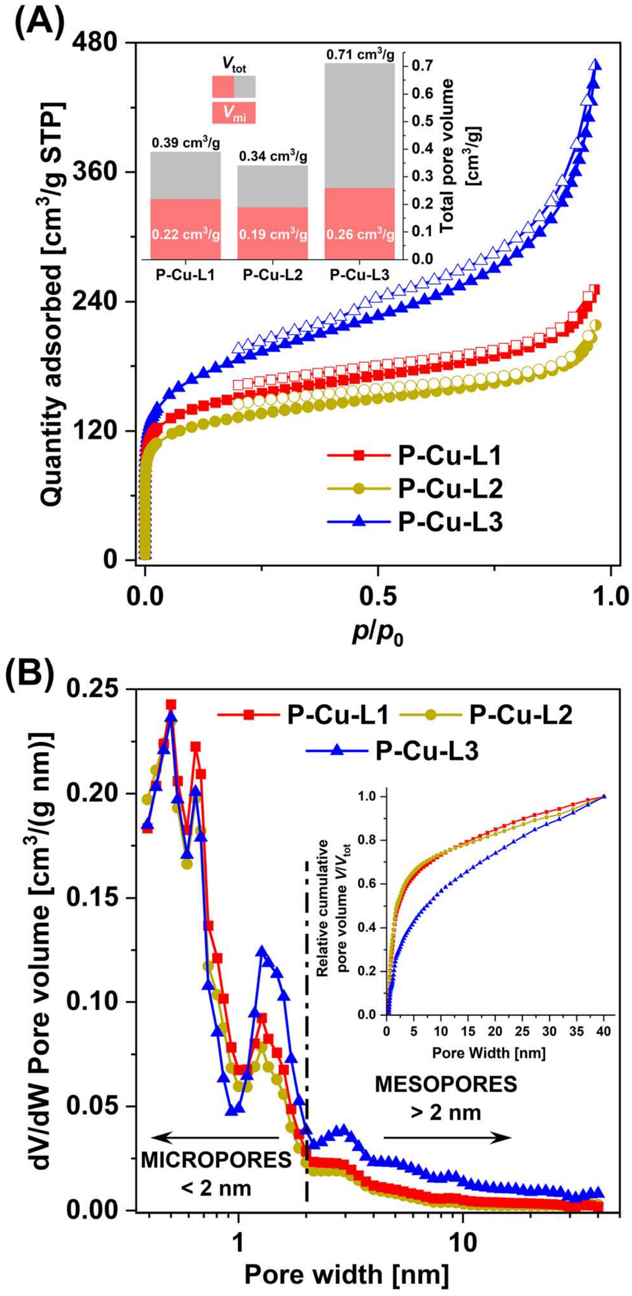

Fig. 7 (A) N_2 adsorption (full symbols) and desorption (empty symbols) isotherms with pore volumes of micropores, V_{mi}, and total pore volumes, V_{tot}, for **P-Cu-L1**, **P-Cu-L2** and **P-Cu-L3**. (B) N_2-DFT calculated pore size distributions with relative cumulative pore volume, V/V_{tot}, for **P-Cu-L1**, **P-Cu-L2** and **P-Cu-L3**.

The type of SALDAC isomer used for the synthesis also affected the morphology of the resulting polymer networks. Scanning electron microscopy (SEM) confirmed the morphological similarity of networks **P-Cu-L1** and **P-Cu-L2** and dissimilarity with network **P-Cu-L3**. SEM images in Fig. 8 display rod-like particles of **P-Cu-L1** and **P-Cu-L2** networks, whereas partly aggregated spherically shaped particles were detected for network **P-Cu-L3**.

Moreover, network **P-Cu-L1** was characterized by powder X-ray diffraction (pXRD, Fig. S21†). The pXRD pattern showed

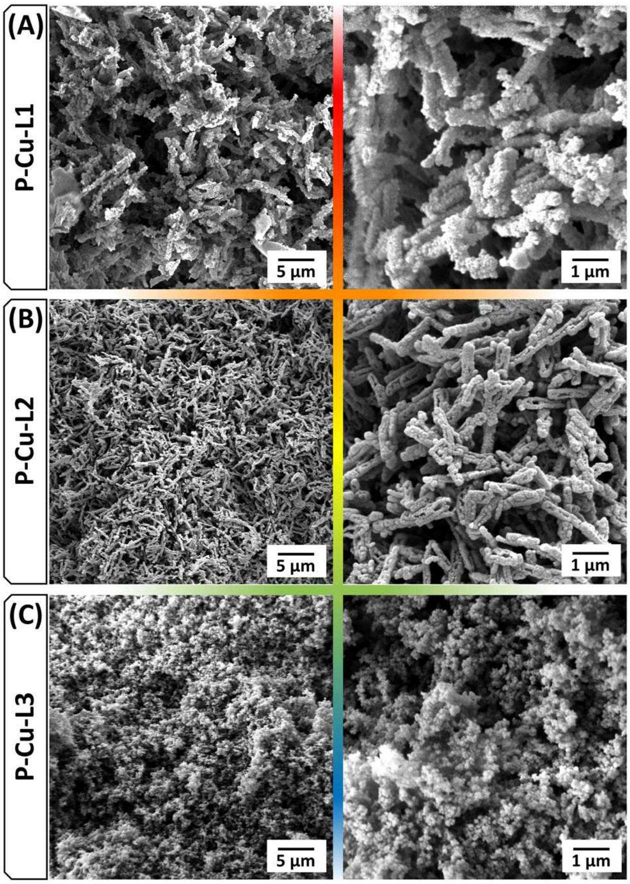

Fig. 8 SEM images of **P-Cu-L1** (A), **P-Cu-L2** (B) and **P-Cu-L3** (C).

Table 2 Results of styrene oxidation catalyzed by organometallic complexes and polymer networks (1 mmol styrene, 3 mmol *tert*-butylhydroperoxide, 10 mg of the catalyst, 3 ml of dichloromethane, 60 °C, 6 h)

Catalyst	Styrene conversion [%]	Styrene oxide selectivity [%]	Benzaldehyde selectivity [%]	TON [mol mol_{Cu}^{-1}]
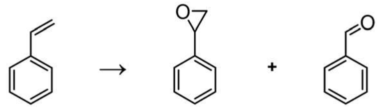				
Cu-L1	89	5	21	34
P-Cu-L1	80	41	40	56
Cu-L2	91	4	25	35
P-Cu-L2	86	24	50	45
Cu-L3	87	2	32	34
P-Cu-L3	90	28	44	48

no distinct signal, indicating the absence of long-range order and confirming the amorphous character of these networks. This finding was fully consistent with the formation of irregular cross-linking during the network formation *via* chain-growth polymerization.

Catalytic activity of organometallic polymer networks in styrene oxidation

The catalytic activity of the prepared organometallic polymer networks **P-Cu-L1**, **P-Cu-L2**, and **P-Cu-L3** was evaluated in styrene oxidation, and compared with the catalytic activity of monomeric complexes **Cu-L1**, **Cu-L2**, and **Cu-L3** (Table 2). In all cases, high styrene conversion was observed (80–91%, 6 h). Benzaldehyde was the most abundant product of all reactions. In the case of monomeric complexes used as catalysts, the selectivity to benzaldehyde was 21–32%. When polymer networks were used as catalysts the selectivity to benzaldehyde increased up to 50%. Another product that formed with remarkable selectivity was styrene oxide. In all cases, the selectivity to styrene oxide increased significantly when polymer networks were used as catalysts instead of monomeric complexes. We observed the increase from 5 to 41%, from 4 to 24% and from 2 to 28% using **P-Cu-L1**, **P-Cu-L2**, and **P-Cu-L3**, respectively. The increase in the selectivity after monomer polymerization was also observed in our previous study.[12] In the case of polymer network **P-Cu-L1**, an interestingly high selectivity to benzaldehyde and styrene oxide (both 40 and 41%) was observed. This network was prepared from the enantiomerically pure complex with the chiral segment (1*S*,2*S*)-1,2-diaminocyclohexane. However, the enantioselectivity of **P-Cu-L1** was not observed (styrene oxide was formed as a racemate). For verification, styrene oxidation was also performed (i) without a catalyst and (ii) with a non-metalated polymer network prepared by polymerization of **L1**. In both cases, no conversion of the substrate was observed. Similar types of materials have already been studied in styrene oxidation using H_2O_2 as an oxidizing agent. Maurya *et al.* studied the catalytic activity of similar copper(II) salen-type complexes encapsulated in zeolite-Y. In this case, a high selectivity to benzaldehyde was obtained (67%), however at low conversion of styrene (only 22%).[75] Even higher selectivity to benzaldehyde (81%) was obtained using half-sandwich C-scorpionate copper(II) complexes on hydrochars, but again under lower styrene conversion (43%).[76] Thus, our materials exhibited higher activity than those mentioned in previous studies and relatively high selectivity to benzaldehyde and, especially in the case of **P-Cu-L1**, also high selectivity to styrene oxide.

The advantage of heterogeneous catalysts based on organometallic polymer networks is their possible reuse in the reaction mixture. We tested the reusability of polymer network **P-Cu-L1** in three consecutive cycles (Table S3†). The catalyst was simply removed from the reaction mixture, washed three times with dichloromethane, and used again as the catalyst for styrene oxidation. The possibility of catalyst reuse was confirmed and, moreover, an increase in styrene conversion in subsequent cycles was observed, accompanied by an increase in selectivity to benzaldehyde.

Conclusions

To summarize this work, three trios of a salen-type ligand, respective copper(II) complex, and organometallic polymer network were developed and prepared, namely (i) ligand **L1**, complex **Cu-L1** and polymer network **P-Cu-L1** were based on enantiomerically pure *trans*-(1*S*,2*S*)-1,2-diaminocyclohexane, (ii) **L2**, **Cu-L2** and **P-Cu-L2** were based on racemic *trans*-1,2-diaminocyclohexane and (iii) **L3**, **Cu-L3** and **P-Cu-L3** were based on the *cis*-1,2-diaminocyclohexane segment. The use of different isomers affected the final textural properties of the prepared polymer networks (microporous *vs.* micro/mesoporous texture, S_{BET} 458–655 $\text{m}^2\ \text{g}^{-1}$). The structures, geometries, and packings of organometallic complexes in solid states (crystal *vs.* powder) were investigated by single-crystal X-ray diffraction and advanced NMR techniques for paramagnetic compounds. The comparison with solid-state NMR spectra of polymer networks revealed the similar geometry of organometallic segments also in the networks and reflected the differences between individual isomers and their influence on the formation of the porous texture. Less spatially demanding *trans* isomers allowed tighter packing leading to lower S_{BET} values, while the more voluminous *cis* isomer formed a polymer network with higher S_{BET}. Finally, the catalytic activity of the prepared organometallic polymer networks was tested. Heterogeneously catalyzed styrene oxidation exhibited remarkably high styrene conversions (well above 80%) with high selectivity to the desired products (up to 41% to styrene oxide and up to 50% to benzaldehyde). All networks showed significantly increased selectivity compared to respective low-molecular organometallic complexes. Good reusability results in catalytic testing pointed to the promising potential of these materials.

Author contributions

DŠ: investigation (development and synthesis of the materials), conceptualization, visualization, and writing – original draft; JB: formal analysis (NMR spectroscopy) and data curation; BB: formal analysis (nitrogen adsorption) and writing – review and editing; IC: formal analysis (X-ray crystallography) and data curation; EVr: investigation (catalysis); EVy: conceptualization (catalysis) and writing – review and editing; JS: conceptualization (development and synthesis of the materials), supervision, and writing – review and editing.

Data availability

All results and experimental data are available in the manuscript and ESI.† The crystallographic data were deposited with the CCDC under numbers 2333975 and 2333976† for **Cu-L1** and **Cu-L3**, respectively. Raw NMR data as well as I/O files from DFT calculations and SIMPSON simulations can be found in the Zenodo repository at **https://doi.org/10.5281/zenodo.10973432**.

Conflicts of interest

There are no conflicts to declare.

Acknowledgements

This work was supported by the Czech Science Foundation (project no. 21-02183S, J. Sedláček; and project no. 24-10843S, J. Blahut) and the Science Foundation of Charles University (project no. 193223, D. Šorm). Computational resources were provided by the e-INFRA CZ project (ID: 90254), supported by the Ministry of Education, Youth and Sports of the Czech Republic. The authors kindly acknowledge the provided financial support.

Notes and references

1 Y.-C. Yuan, M. Mellah, E. Schulz and O. R. P. David, *Chem. Rev.*, 2022, **122**, 8841–8883.
2 P. G. Cozzi, *Chem. Soc. Rev.*, 2004, **33**, 410–421.
3 A. Erxleben, *Inorg. Chim. Acta*, 2018, **472**, 40–57.
4 A. M. G. Mutti, F. S. M. Canisares, W. B. S. Machini, A. M. Pires, M. F. S. Teixeira and S. A. M. Lima, *Optik*, 2021, **243**, 167454.
5 G. Yu, Y. Liu, Y. Song, X. Wu and D. Zhu, *Synth. Met.*, 2001, **117**, 211–214.
6 O. Lavastre, I. Illitchev, G. Jegou and P. H. Dixneuf, *J. Am. Chem. Soc.*, 2002, **124**, 5278–5279.
7 A. C. W. Leung, J. H. Chong, B. O. Patrick and M. J. MacLachlan, *Macromolecules*, 2003, **36**, 5051–5054.
8 T. Glaser, M. Heidemeier, R. Fröhlich, P. Hildebrandt, E. Bothe and E. Bill, *Inorg. Chem.*, 2005, **44**, 5467–5482.
9 T. Glaser, M. Heidemeier, S. Grimme and E. Bill, *Inorg. Chem.*, 2004, **43**, 5192–5194.
10 N. S. Venkataramanan, G. Kuppuraj and S. Rajagopal, *Coord. Chem. Rev.*, 2005, **249**, 1249–1268.
11 S. Shaw and J. D. White, *Chem. Rev.*, 2019, **119**, 9381–9426.
12 D. Šorm, B. Bashta, J. Blahut, I. Císařová, L. Dolejšová Sekerová, E. Vyskočilová and J. Sedláček, *Eur. Polym. J.*, 2023, **184**, 111772.
13 W. Al Zoubi and Y. G. Ko, *Appl. Organomet. Chem.*, 2017, **31**, e3574.
14 M. S. More, P. G. Joshi, Y. K. Mishra and P. K. Khanna, *Mater. Today Chem.*, 2019, **14**, 100195.
15 K. C. Gupta and A. K. Sutar, *Coord. Chem. Rev.*, 2008, **252**, 1420–1450.
16 S. Lundgren, E. Wingstrand, M. Penhoat and C. Moberg, *J. Am. Chem. Soc.*, 2005, **127**, 11592–11593.
17 J. A. Kalow and A. G. Doyle, *J. Am. Chem. Soc.*, 2010, **132**, 3268–3269.
18 R. Kowalczyk, P. Kwiatkowski, J. Skarżewski and J. Jurczak, *J. Org. Chem.*, 2009, **74**, 753–756.
19 S. Liao and B. List, *Adv. Synth. Catal.*, 2012, **354**, 2363–2367.

20 E. F. DiMauro and M. C. Kozlowski, *Org. Lett.*, 2001, **3**, 1641–1644.

21 M. North, S. C. Z. Quek, N. E. Pridmore, A. C. Whitwood and X. Wu, *ACS Catal.*, 2015, **5**, 3398–3402.

22 V. Aomchad, S. Del Gobbo, P. Yingcharoen, A. Poater and V. D'Elia, *Catal. Today*, 2021, **375**, 324–334.

23 Y.-M. Shen, W.-L. Duan and M. Shi, *J. Org. Chem.*, 2003, **68**, 1559–1562.

24 A. Vidal-López, S. Posada-Pérez, M. Solà, V. D'Elia and A. Poater, *Green Chem. Eng.*, 2022, **3**, 180–187.

25 F. Della Monica and C. Capacchione, *Asian J. Org. Chem.*, 2022, **11**, e202200300.

26 J. A. Castro-Osma, K. J. Lamb and M. North, *ACS Catal.*, 2016, **6**, 5012–5025.

27 A. Decortes, A. M. Castilla and A. W. Kleij, *Angew. Chem., Int. Ed.*, 2010, **49**, 9822–9837.

28 C. Baleizão and H. Garcia, *Chem. Rev.*, 2006, **106**, 3987–4043.

29 M. Abd El Sater, N. Jaber and E. Schulz, *ChemCatChem*, 2019, **11**, 3662–3687.

30 J. Rakhtshah, *Coord. Chem. Rev.*, 2022, **467**, 214614.

31 J. Min, W. Song, T. Hu, Y. Zhi, Z. Xia, T. Zhang, S. Shan and H. Su, *Ceram. Int.*, 2021, **47**, 35320–35332.

32 T. Maharana, N. Nath, H. C. Pradhan, S. Mantri, A. Routaray and A. K. Sutar, *React. Funct. Polym.*, 2022, **171**, 105142.

33 I. Kuźniarska-Biernacka, C. Pereira, A. P. Carvalho, J. Pires and C. Freire, *Appl. Clay Sci.*, 2011, **53**, 195–203.

34 C. Xing, J. Deng, R. Tan, M. Gao, P. Hao, D. Yin and D. Yin, *Catal. Sci. Technol.*, 2017, **7**, 5944–5952.

35 R. Ji, K. Yu, L.-L. Lou and S. Liu, *J. Mol. Catal. A: Chem.*, 2013, **378**, 7–16.

36 M. Halder, P. Bhanja, Md. M. Islam, A. Bhaumik and Sk. M. Islam, *New J. Chem.*, 2018, **42**, 11896–11904.

37 S. Roy, P. Bhanja, Sk. Safikul Islam, A. Bhaumik and Sk. Manirul Islam, *Chem. Commun.*, 2016, **52**, 1871–1874.

38 Md. M. Islam, P. Bhanja, M. Halder, S. K. Kundu, A. Bhaumik and Sk. M. Islam, *RSC Adv.*, 2016, **6**, 109315–109321.

39 M. Shukla, K. C. Barick, H. G. Salunke and S. Chandra, *Mol. Catal.*, 2021, **502**, 111367.

40 W. Zhou, Q.-W. Deng, H.-J. He, L. Yang, T.-Y. Liu, X. Wang, D.-Y. Zheng, Z.-B. Dai, L. Sun, C. Liu, H. Wu, Z. Li and W.-Q. Deng, *Angew. Chem., Int. Ed.*, 2023, **62**, e202214143.

41 S. Kramer, N. R. Bennedsen and S. Kegnæs, *ACS Catal.*, 2018, **8**, 6961–6982.

42 S. Luo, Z. Zeng, H. Wang, W. Xiong, B. Song, C. Zhou, A. Duan, X. Tan, Q. He, G. Zeng, Z. Liu and R. Xiao, *Prog. Polym. Sci.*, 2021, **115**, 101374.

43 J.-S. M. Lee and A. I. Cooper, *Chem. Rev.*, 2020, **120**, 2171–2214.

44 W. Song, Y. Zhang, C. H. Tran, H. K. Choi, D.-G. Yu and I. Kim, *Prog. Polym. Sci.*, 2023, **142**, 101691.

45 J. Sedláček and H. Balcar, *Polym. Rev.*, 2017, **57**, 31–51.

46 L. Sekerová, M. Lhotka, E. Vyskočilová, T. Faukner, E. Slováková, J. Brus, L. Červený and J. Sedláček, *Chem. – Eur. J.*, 2018, **24**, 14742–14749.

47 Y. Xie, T.-T. Wang, X.-H. Liu, K. Zou and W.-Q. Deng, *Nat. Commun.*, 2013, **4**, 1960.

48 Y. Xie, T.-T. Wang, R.-X. Yang, N.-Y. Huang, K. Zou and W.-Q. Deng, *ChemSusChem*, 2014, **7**, 2110–2114.

49 R. Luo, Y. Chen, Q. He, X. Lin, Q. Xu, X. He, W. Zhang, X. Zhou and H. Ji, *ChemSusChem*, 2017, **10**, 1526–1533.

50 J. Li, Y. Han, H. Lin, N. Wu, Q. Li, J. Jiang and J. Zhu, *ACS Appl. Mater. Interfaces*, 2020, **12**, 609–618.

51 D. Meng, J. Bi, Y. Dong, B. Hao, K. Qin, T. Li and D. Zhu, *Chem. Commun.*, 2020, **56**, 2889–2892.

52 X. Sun, F. Meng, Q. Su, K. Luo, P. Ju, Z. Liu, X. Li, G. Li and Q. Wu, *Dalton Trans.*, 2020, **49**, 13582–13587.

53 H. Li, J. Chen, J. Liu, C. Li, L. Liu and Q. Yang, *ChemNanoMat*, 2022, **8**, e202100386.

54 A. J. Pell, G. Pintacuda and C. P. Grey, *Prog. Nucl. Magn. Reson. Spectrosc.*, 2019, **111**, 1–271.

55 J. Blahut, L. Benda, A. L. Lejeune, K. J. Sanders, B. Burcher, E. Jeanneau, D. Proriol, L. Catita, P.-A. R. Breuil, A.-A. Quoineaud, A. J. Pell and G. Pintacuda, *RSC Adv.*, 2021, **11**, 29870–29876.

56 Y. Nishiyama, G. Hou, V. Agarwal, Y. Su and A. Ramamoorthy, *Chem. Rev.*, 2023, **123**, 918–988.

57 Y. Nishiyama and N. T. Duong, *J. Magn. Reson. Open*, 2022, **10–11**, 100062.

58 V. D'Anna, S. Norsic, D. Gajan, K. Sanders, A. J. Pell, A. Lesage, V. Monteil, C. Copéret, G. Pintacuda and P. Sautet, *J. Phys. Chem. C*, 2016, **120**, 18075–18087.

59 K. Saalwächter, F. Lange, K. Matyjaszewski, C.-F. Huang and R. Graf, *J. Magn. Reson.*, 2011, **212**, 204–215.

60 S. M. Elbert and M. Mastalerz, *Org. Mater.*, 2020, **02**, 182–203.

61 J. Vaara, S. A. Rouf and J. Mareš, *J. Chem. Theory Comput.*, 2015, **11**, 4840–4849.

62 G. M. Sheldrick, *Acta Crystallogr., Sect. A: Found. Adv.*, 2015, **71**, 3–8.

63 G. M. Sheldrick, *Acta Crystallogr., Sect. C: Struct. Chem.*, 2015, **71**, 3–8.

64 G. R. Fulmer, A. J. M. Miller, N. H. Sherden, H. E. Gottlieb, A. Nudelman, B. M. Stoltz, J. E. Bercaw and K. I. Goldberg, *Organometallics*, 2010, **29**, 2176–2179.

65 D. W. Juhl, Z. Tošner and T. Vosegaard, in *Annual Reports on NMR Spectroscopy*, ed. G. A. Webb, Academic Press, 2020, vol. 100, pp. 1–59.

66 *TURBOMOLE V7.1, a development of University of Karlsruhe and Forschungszentrum Karlsruhe GmbH*, 1989–2007.

67 F. Neese, *Wiley Interdiscip. Rev.: Comput. Mol. Sci.*, 2012, **2**, 73–78.

68 W.-K. Dong, J.-G. Duan, Y.-H. Guan, J.-Y. Shi and C.-Y. Zhao, *Inorg. Chim. Acta*, 2009, **362**, 1129–1134.

69 N. Kordestani, H. Amiri Rudbari, G. Bruno, S. Rosario, J. D. Braun, D. E. Herbert, O. Blacque, I. Correia, M. A. Zaman, M. M. Bindu, C. Janiak and M. Enamullah, *Dalton Trans.*, 2020, **49**, 8247–8264.

70 R. K. Hylton, G. J. Tizzard, T. L. Threlfall, A. L. Ellis, S. J. Coles, C. C. Seaton, E. Schulze, H. Lorenz, A. Seidel-Morgenstern, M. Stein and S. L. Price, *J. Am. Chem. Soc.*, 2015, **137**, 11095–11104.

71 O. A. Lodochnikova, V. A. Startseva, L. E. Nikitina, A. V. Bodrov, A. E. Klimovitskii, E. N. Klimovitskii and I. A. Litvinov, *CrystEngComm*, 2014, **16**, 4314–4321.

72 C. van Beek and V. V. Samoshin, *Tetrahedron Lett.*, 2022, **102**, 153930.

73 A. Bertarello, L. Benda, K. J. Sanders, A. J. Pell, M. J. Knight, V. Pelmenschikov, L. Gonnelli, I. C. Felli, M. Kaupp, L. Emsley, R. Pierattelli and G. Pintacuda, *J. Am. Chem. Soc.*, 2020, **142**, 16757–16765.

74 O. Trhlíková, J. Zedník, H. Balcar, J. Brus and J. Sedláček, *J. Mol. Catal. A: Chem.*, 2013, **378**, 57–66.

75 M. R. Maurya, A. K. Chandrakar and S. Chand, *J. Mol. Catal. A: Chem.*, 2007, **270**, 225–235.

76 T. A. G. Duarte, A. P. Carvalho and L. M. D. R. S. Martins, *Catal. Today*, 2020, **357**, 56–63.

Electronic supplementary information (ESI)

Complex Isomerism Influencing the Texture Properties of Organometallic [Cu(salen)] Porous Polymers: Paramagnetic Solid-State NMR Characterization and Heterogeneous Catalysis

David Šorm[a]*, Jan Blahut[b]*, Bogdana Bashta[a], Ivana Císařová[c], Eva Vrbková[d], Eliška Vyskočilová[d] and Jan Sedláček[a]

[a] Department of Physical and Macromolecular Chemistry, Faculty of Science, Charles University, Hlavova 2030, Prague 2, 128 43, Czech Republic

[b] Institute of Organic Chemistry and Biochemistry of the Czech Academy of Sciences, Flemingovo náměstí 542/2, Prague 6, 160 00, Czech Republic

[c] Department of Inorganic Chemistry, Faculty of Science, Charles University, Hlavova 2030, Prague 2, 128 43, Czech Republic

[d] Department of Organic Technology, University of Chemistry and Technology Prague, Technická 5, Prague 6, 166 28, Czech Republic

*corresponding authors

L1:
(1*S*,2*S*)-*N,N’-bis*(5-ethynylsalicylidene)-1,2-diaminocyclohexane

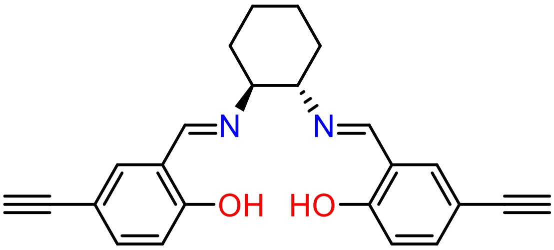

Figure S1: Structure of the ligand **L1**

^{1}H NMR (400 MHz, CD_2Cl_2) δ 13.52 (s, 2H), 8.25 (s, 2H), 7.37 (d, *J* = 2.1 Hz, 2H), 7.34 (s, 2H), 6.82 (d, *J* = 8.7 Hz, 2H), 3.38 – 3.29 (m, 2H), 3.00 (s, 2H), 2.00 – 1.81 (m, 2H), 1.79 – 1.65 (m, 2H), 1.57 – 1.43 (m, 4H).

^{13}C NMR (101 MHz, CD_2Cl_2) δ 164.36, 162.08, 136.13, 135.73, 118.95, 117.57, 112.46, 83.27, 75.88, 72.86, 33.30, 24.52.

HR-MS ESI, measured (calculated) m/z of M+H adduct: 371.174411 (371.175404), $C_{24}H_{23}N_2O_2$

L2:
trans-N,N'-bis(5-ethynylsalicylidene)-1,2-diaminocyclohexane

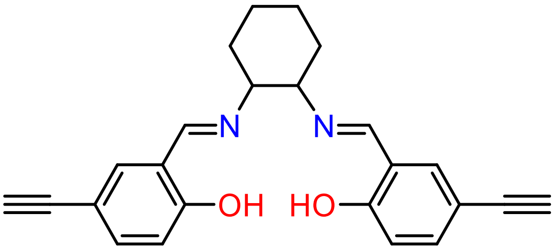

Figure S2: Structure of the ligand **L2**

^{1}H NMR (400 MHz, CD_2Cl_2) δ 13.52 (s, 2H), 8.25 (s, 2H), 7.37 (d, *J* = 2.1 Hz, 2H), 7.34 (s, 2H), 6.82 (d, *J* = 8.8 Hz, 2H), 3.40 – 3.33 (m, 2H), 3.00 (s, 2H), 1.98 – 1.85 (m, 2H), 1.79 – 1.65 (m, 2H), 1.56 – 1.44 (m, 4H).

^{13}C NMR (101 MHz, CD_2Cl_2) δ 164.36, 162.08, 136.13, 135.73, 118.95, 117.57, 112.46, 83.27, 75.88, 72.85, 33.30, 24.52.

HR-MS ESI, measured (calculated) m/z of M+H adduct: 371.174846 (371.175404), $C_{24}H_{23}N_2O_2$

L3:
cis-N,N'-bis(5-ethynylsalicylidene)-1,2-diaminocyclohexane

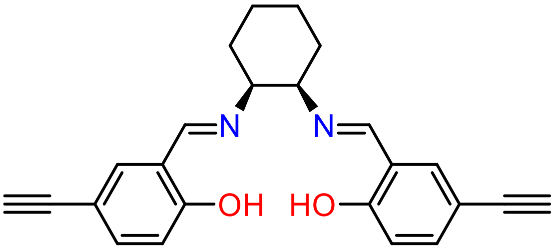

Figure S3: Structure of the ligand **L3**

^{1}H NMR (400 MHz, CD_2Cl_2) δ 13.76 (s, 2H), 8.33 (s, 2H), 7.46 – 7.37 (m, 4H), 6.86 (d, *J* = 8.4 Hz, 2H), 3.66 – 3.58 (m, 2H), 3.03 (s, 2H), 2.02 – 1.73 (m, 4H), 1.67 – 1.51 (m, 4H).

^{13}C NMR (101 MHz, CD_2Cl_2) δ 164.00, 162.40, 136.23, 135.74, 119.10, 117.77, 112.37, 83.38, 75.88, 69.76, 31.10, 22.74.

HR-MS ESI, measured (calculated) m/z of M+H adduct: 371.174930 (371.175404), $C_{24}H_{23}N_2O_2$

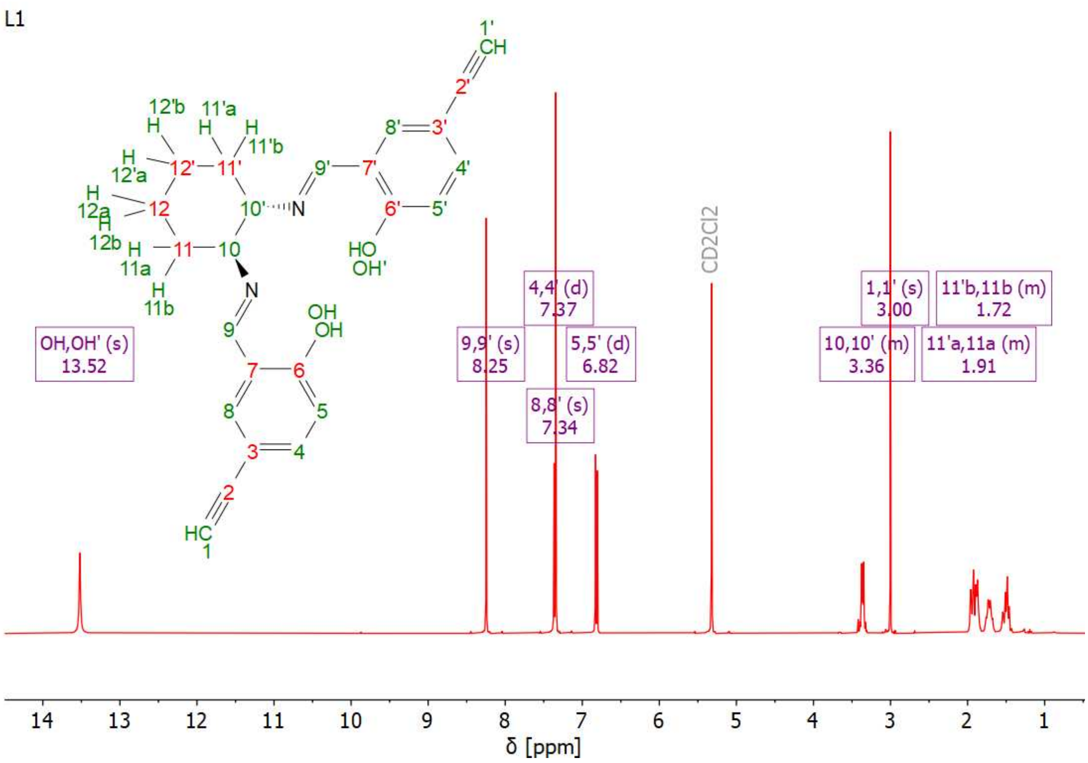

Figure S4: ^{1}H NMR spectrum of **L1** ligand

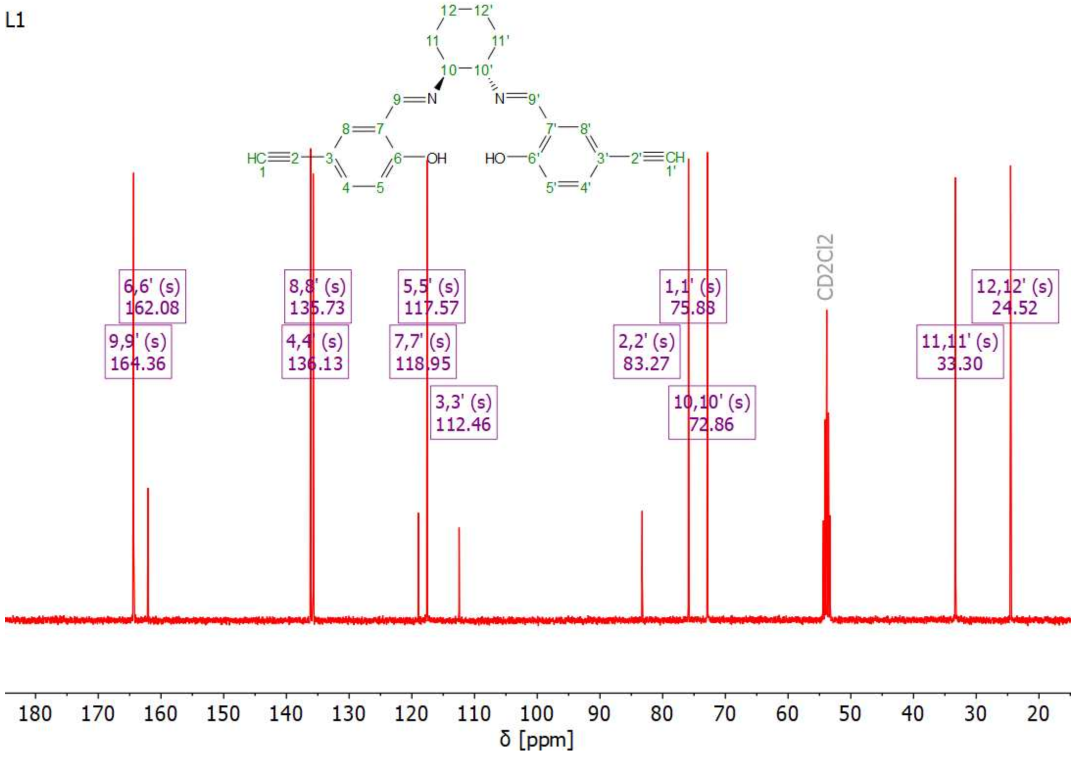

Figure S5: ^{13}C{^{1}H} NMR spectrum of **L1** ligand

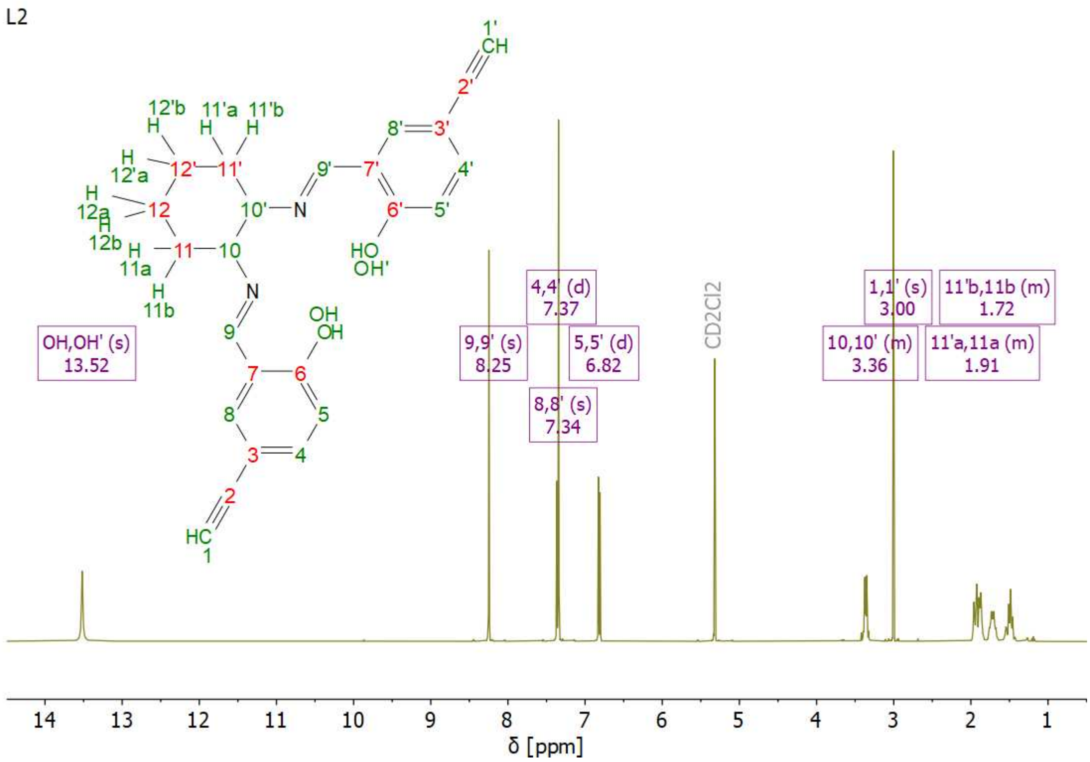

Figure S6: ^{1}H NMR spectrum of **L2** ligand

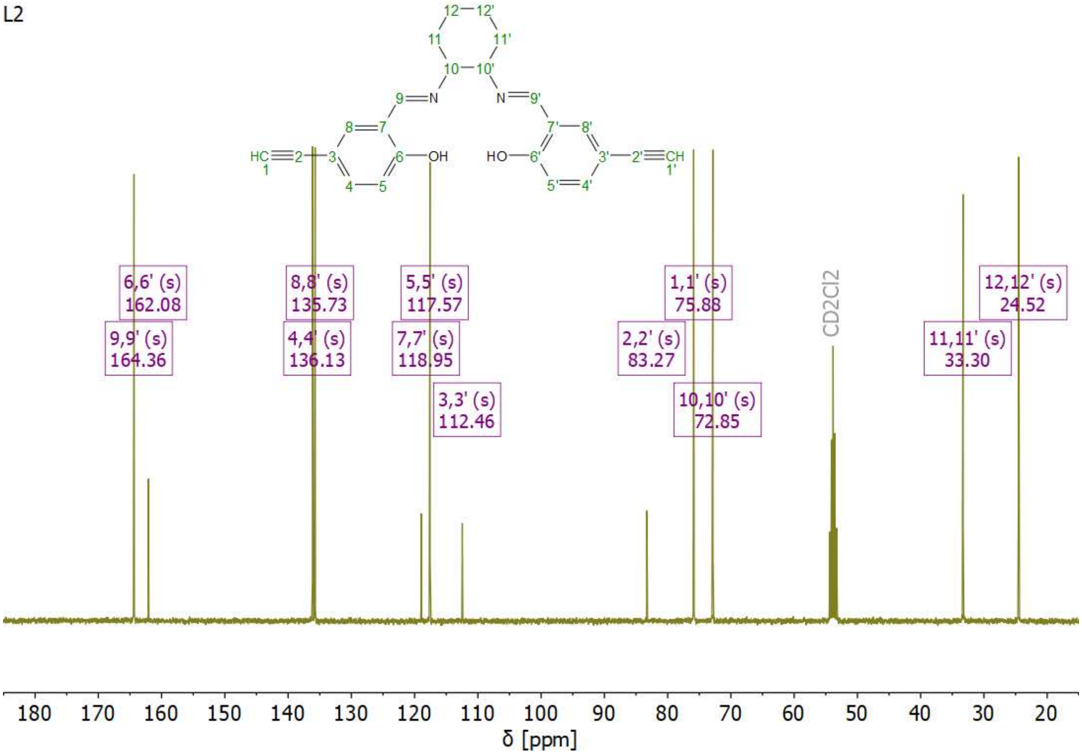

Figure S7: ^{13}C{^{1}H} NMR spectrum of **L2** ligand

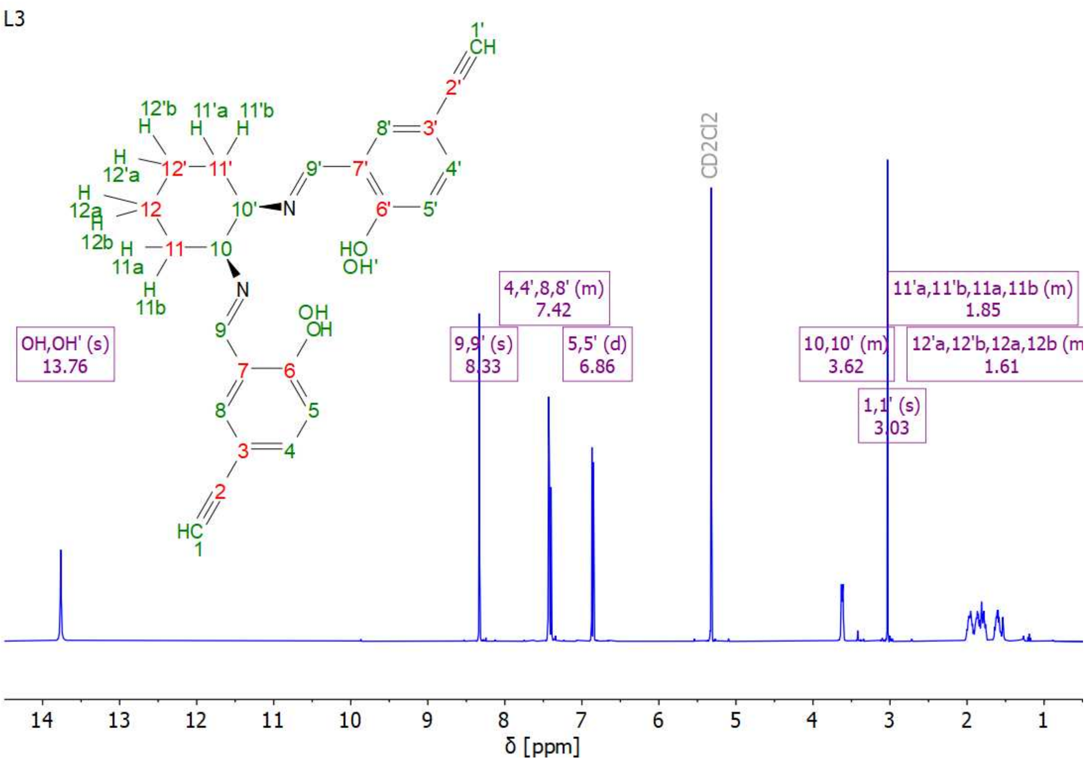

Figure S8: ^{1}H NMR spectrum of **L3** ligand

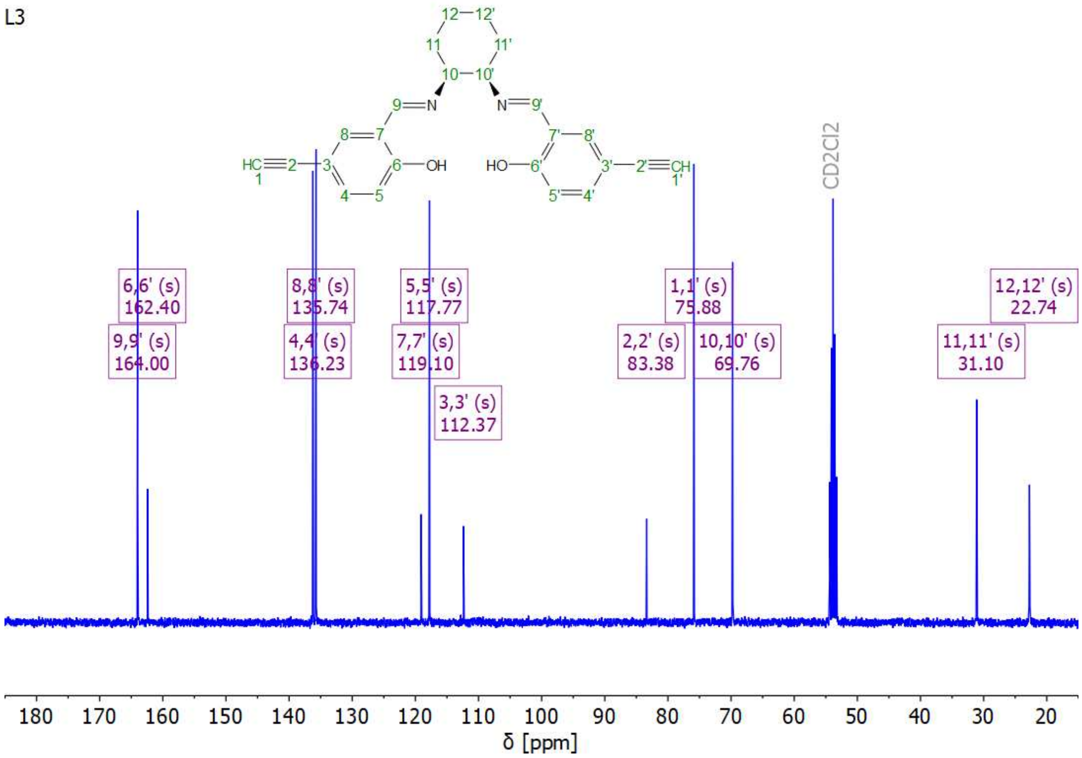

Figure S9: ^{13}C{^{1}H} NMR spectrum of **L3** ligand

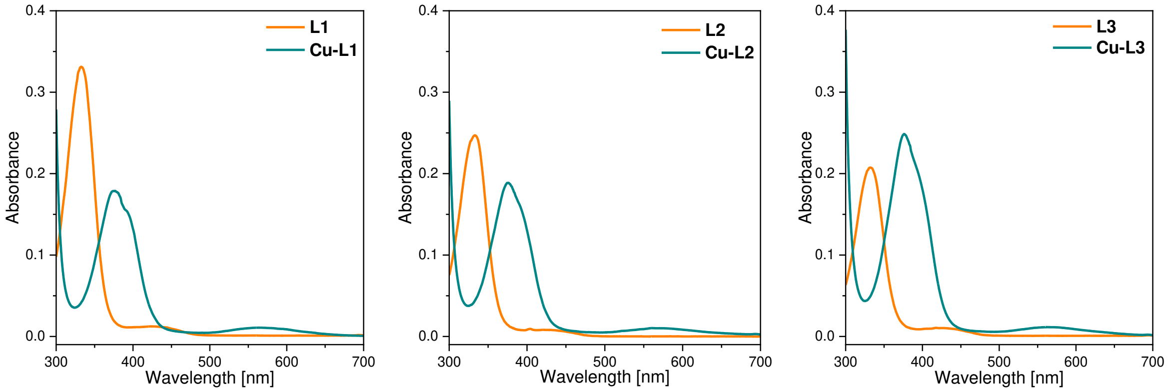

Figure S10: UV/VIS spectra of ligands (**L1**, **L2** and **L3**) and complexes (**Cu-L1**, **Cu-L2** and **Cu-L3**)

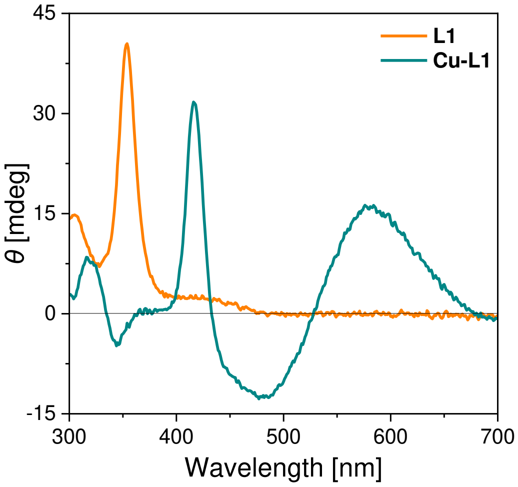

Figure S11: Circular dichroism (CD) spectra of ligand **L1** and complex **Cu-L1**.

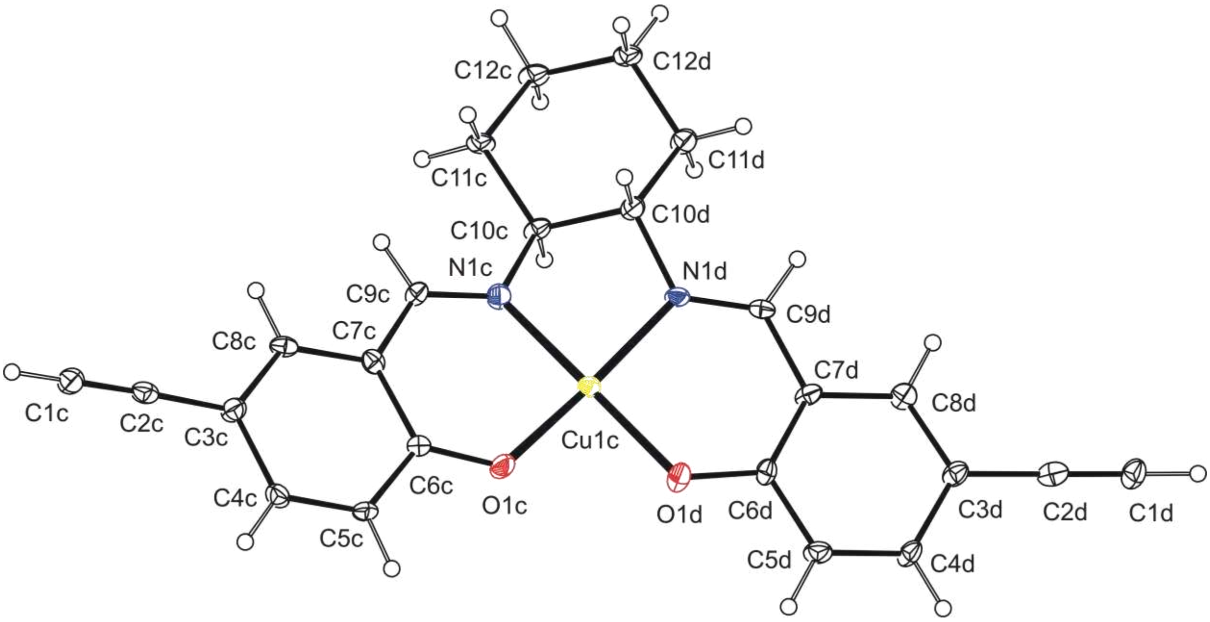

Figure S12: View on the one of two symmetrically independent molecule of **Cu-L1** with the atom numbering schema, the displacement ellipsoids are drawn at 50% probability level.

Crystal data for **Cu-L1**: $C_{24}H_{20}CuN_2O_2\cdot C_3H_7NO$, M_r = 505.05; Monoclinic, $P2_1$, (No 4), a = 8.6380 (3) Å, b = 31.0524 (10) Å, c = 8.6749 (3) Å, β = 90.667 (2), V = 2326.72

(14) Å^3, Z = 4, D_x = 1.442 Mg m^{-3}, brown plate of dimensions 0.28 × 0.16 × 0.03 mm, multi-scan absorption correction (μ = 1.61 mm^{-1}) T_{min} = 0.79, T_{max} = 0.96; a total of 24115 measured reflections (θ_{max}= 68.4˚), from which 8359 were unique (R_{int} = 0.050) and 7893 observed according to the $I > 2\sigma(I)$ criterion. The refinement converged (Δ/σ_{max}= 0.001) to R = 0.061 for observed reflections and w$R(F^2)$ = 0.143, GOF = 1.16 for 617 parameters and all 8359 reflections. The final difference map displayed no peaks of chemical significance ($\Delta\rho_{max}$ = 0.60, $\Delta\rho_{min}$ -0.88 e.Å^{-3}).

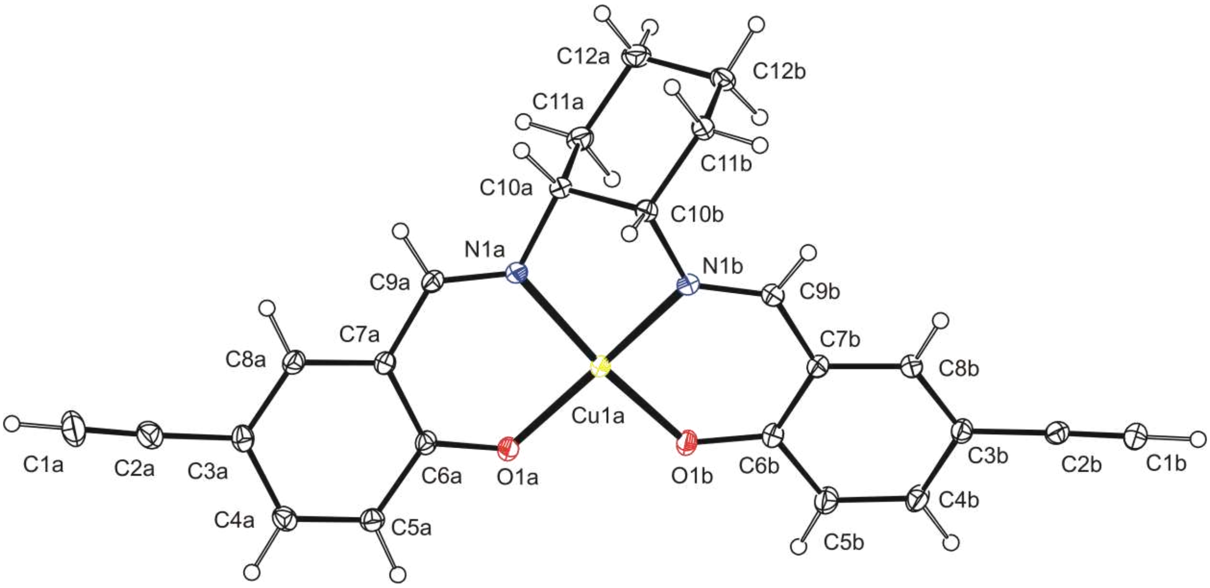

Figure S13: View on molecule of **Cu-L3** with the atom numbering schema, the displacement ellipsoids are drawn at 50% probability level.

Crystal data for **Cu-L3**: $C_{24}H_{20}CuN_2O_2$, M_r = 431.96; Monoclinic, $P2_1/n$, (No 14), a = 14.1633 (10) Å, b = 9.0797 (7) Å, c = 16.0469 (11) Å, β = 112.615 (2), V = 1904.9 (2) Å^3, Z = 4, D_x = 1.506 Mg m^{-3}, green prism of dimensions 0.25 × 0.10 × 0.07 mm, multi-scan absorption correction (μ = 1.81 mm^{-1}) T_{min} = 0.77, T_{max} = 0.89; a total of 57728 measured reflections (θ_{max}= 77.5˚), from which 4036 were unique (R_{int} = 0.031) and 3854 observed according to the $I > 2\sigma(I)$ criterion. The refinement converged (Δ/σ_{max}= 0.001) to R = 0.032 for observed reflections and w$R(F^2)$ = 0.088, GOF = 1.04 for 262 parameters and all 4036 reflections. The final difference map displayed no peaks of chemical significance ($\Delta\rho_{max}$ = 0.67, $\Delta\rho_{min}$ -0.70 e.Å^{-3}).

X-ray crystallographic data have been deposited with the Cambridge Crystallographic Data Centre (CCDC) under deposition number 2333975 and 2333976 for **Cu-L1** and **Cu-L3**, respectively and can be obtained free of charge from the Centre via its website (https://www.ccdc.cam.ac.uk/structures/).

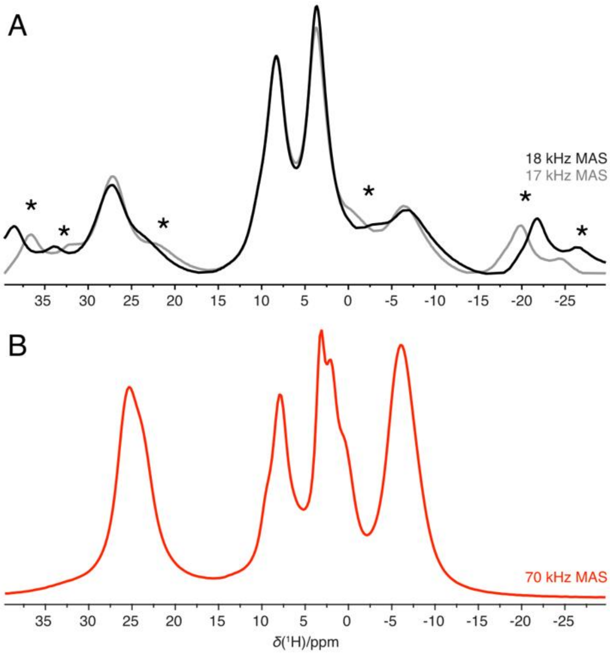

Figure S14: Comparison of slow and fast MAS ^{1}H NMR spectra of **Cu-L1**.

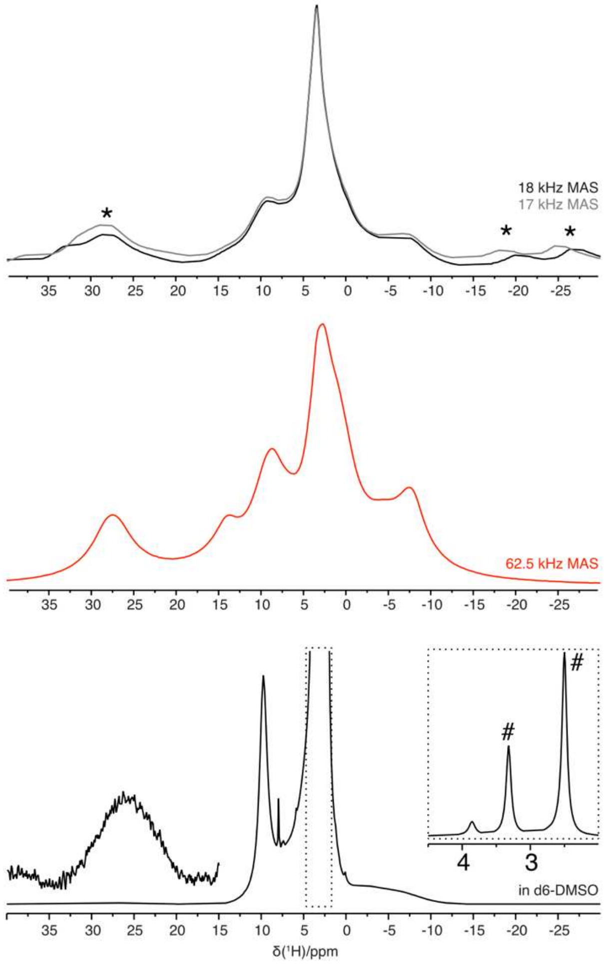

Figure S15: Comparison of slow and fast MAS ^{1}H NMR spectra of **Cu-L3** and solution ^{1}H NMR spectra of **Cu-L3**.

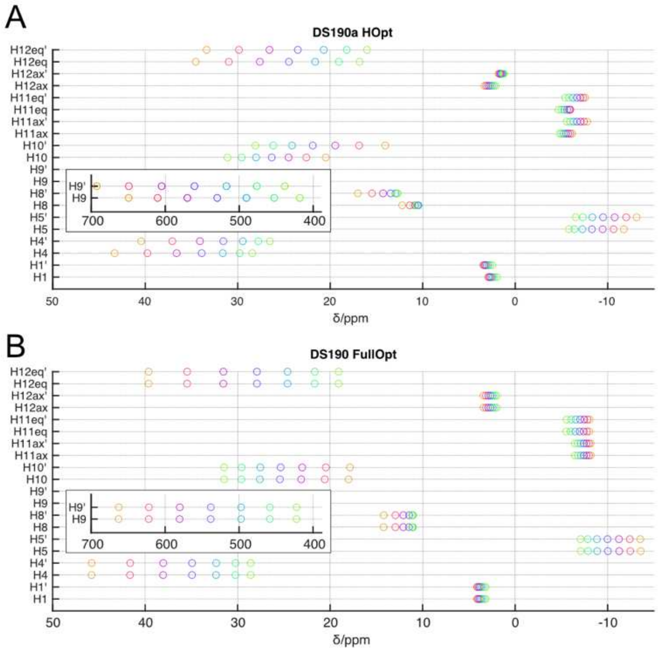

Figure S16: ^{1}H NMR shifts of **Cu-L1** predicted by calculations for X-ray based geometry with refined ^{1}H positions (A) and fully optimized geometry in COSMO/CHCl$_3$ solvent model (B) calculated for range of HFX admixture (from orange 10% for green 40% in 5% steps) (298 K).

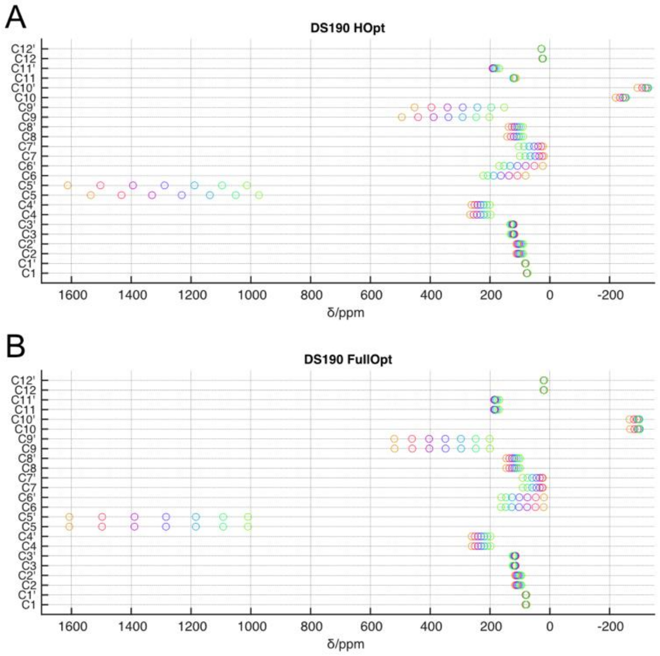

Figure S17: ^{13}C NMR shifts of **Cu-L1** predicted by calculations for X-ray based geometry with refined ^{1}H positions (A) and fully optimized geometry in COSMO/CHCl$_3$ solvent model (B) calculated for range of HFX admixture (from orange 10% for green 40% in 5% steps) (298 K).

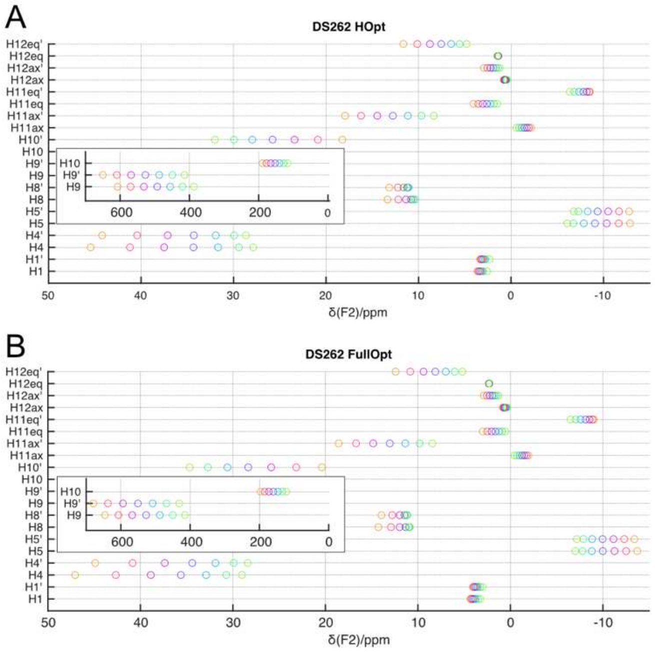

Figure S18: ^{1}H NMR shifts of **Cu-L3** predicted by calculations for X-ray based geometry with refined ^{1}H positions (A) and fully optimized geometry in COSMO/CHCl$_3$ solvent model (B) calculated for range of HFX admixture (from orange 10% for green 40% in 5% steps) (298 K).

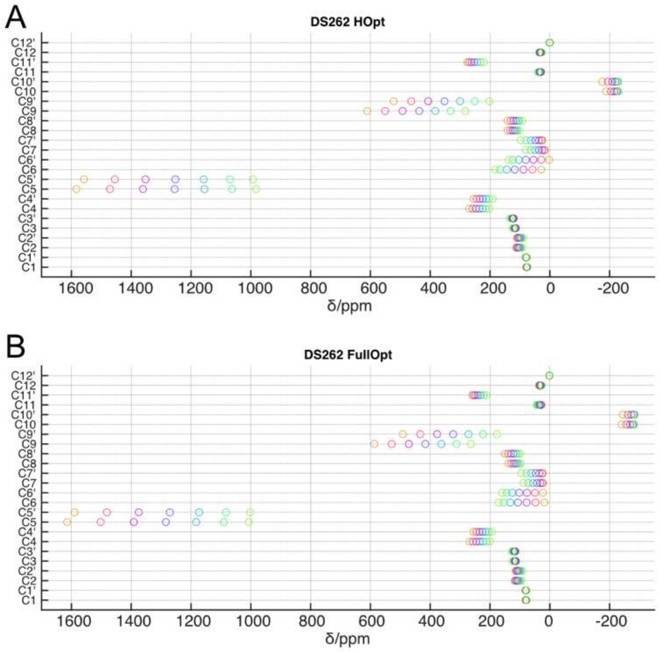

Figure S19: ^{13}C NMR shifts of **Cu-L3** predicted by calculations for X-ray based geometry with refined ^{1}H positions (A) and fully optimized geometry in COSMO/CHCl$_3$ solvent model (B) calculated for range of HFX admixture (from orange 10% for green 40% in 5% steps) (298 K).

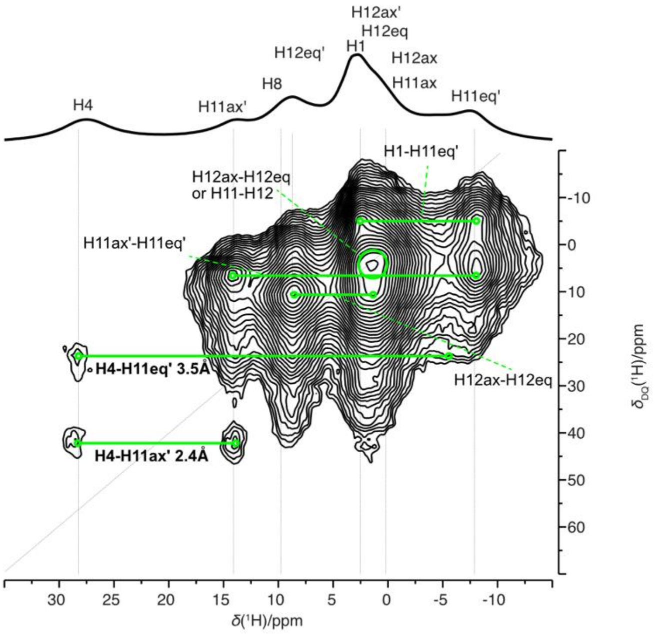

Figure S20: Homonuclear BaBa16 ^{1}H single-double quantum (SQ-DQ) correlation of **Cu-L3**.

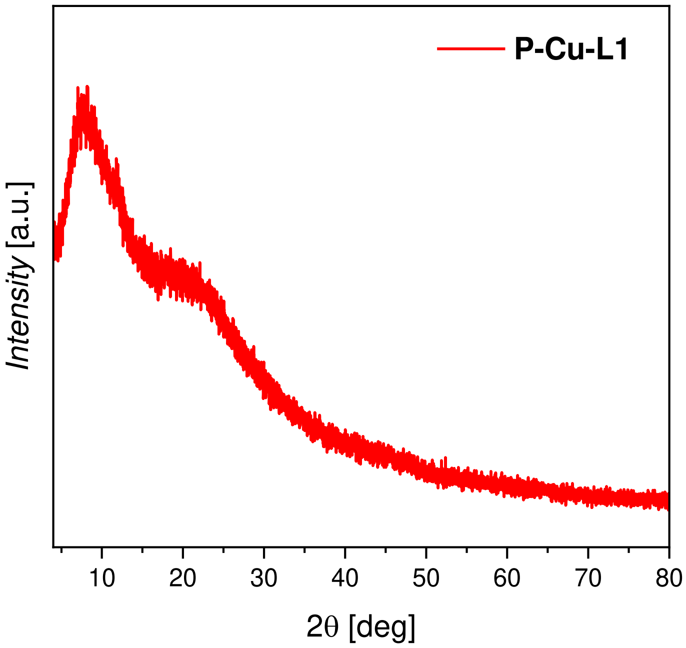

Figure S21: Powder X-Ray Diffraction (pXRD) pattern of network **P-Cu-L1**.

Powder X-ray Diffraction (XRD) pattern was collected using a high-resolution Explorer diffractometer (GNR Analytical Instruments, Italy) equipped with a one-dimensional Mythen 1K silicon strip detector (Dectris, Switzerland). A Cu X-Ray tube (wavelength λ = 1.54 Å) operated at 40 kV and 30 mA and monochromatized with Ni foil (β filter) was used. Measurements were performed in the 2θ range of 5 – 80° with a 0.1° step and 15 s exposure time at each step.

Table S1: Observed ^{1}H and ^{13}C NMR shift from HSQC-TEDOR experiment of **Cu-L1** a related calculated value for 10%, 25% and 40% of Hartee-Fock exchange admixture (at 298 K) and for various temperature 298 K and 323 K (using 25% HFX), as well as decomposition of calculated NMR shift (298 K, 25% HFX) to orbital shift ($\delta_{dia,K} = \sigma_{ref} - \sigma_{dia,K}$), Fermi contact ($\sigma_{FC}$) and spin-dipolar ($\sigma_{SD}$) shielding. All values listed in ppm, for atom label see Scheme 1.

	δ_{exp}	$\delta_{\mathrm{calc}}^{10\%}$	$\delta_{\mathrm{calc}}^{25\%}$	$\delta_{\mathrm{calc}}^{40\%}$	$\delta_{\mathrm{calc}}^{298\mathrm{K}}$	$\delta_{\mathrm{calc}}^{323\mathrm{K}}$	$\delta_{\mathrm{dia},K}$	σ_{FC}	σ_{SD}
H1	3.9	4.13	3.77	3.18	3.77	3.70	2.81	-1.01	0.05
H4	24.5	45.79	34.93	28.59	34.93	32.82	7.76	-27.36	0.20
H5	ND	-13.55	-10.00	-7.08	-10.00	-8.68	7.14	16.51	0.63
H8	8.9	14.21	11.47	11.15	11.47	11.16	7.54	-4.24	0.31
H9	ND	662.79	538.35	422.32	538.35	497.34	8.31	-530.81	0.77
H10	ND	17.93	25.39	31.47	25.39	23.67	3.14	-22.44	0.19
H11ax	-5.8	-8.16	-7.43	-6.45	-7.43	-6.76	1.24	8.34	0.32
H11eq	-5.8	-8.04	-7.00	-5.55	-7.00	-6.27	2.48	9.02	0.46
H12ax	1.6	3.42	2.66	2.00	2.66	2.56	1.36	-1.48	0.18
H12eq	25.0	39.63	27.91	19.09	27.91	25.91	2.02	-26.09	0.19
C1	80.4	81.5	78.8	77.8	78.8	79.0	82.08	3.14	0.17
C2	Q	115.9	105.9	94.4	105.9	104.7	90.16	-15.85	0.10
C3	Q	114.1	117.4	124.3	117.4	117.2	114.34	-3.44	0.38
C4	214	261.0	229.8	198.2	229.8	223.6	149.74	-81.55	1.52
C5	ND	1607.0	1283.6	1009.5	1283.6	1194.4	131.63	-1153.34	1.41
C6	Q	20.2	102.4	162.9	102.4	108.5	180.85	74.40	4.04
C7	Q	23.2	44.8	90.8	44.8	51.0	125.66	78.53	2.37
C8	99	145.7	118.4	99.9	118.4	120.9	150.85	31.31	1.12
C9	NA	519.6	349.0	200.9	349.0	335.3	170.89	-184.00	5.84
C10	NA	-267.7	-298.4	-296.2	-298.4	-269.7	71.59	367.18	2.77
C11	162	184.0	183.7	169.4	183.7	171.9	31.57	-153.36	1.27
C12	24	19.2	20.7	21.3	20.7	21.2	27.85	6.76	0.40

ND – not detected signal, Q - quaternary carbon

Table S2: Observed ^{1}H and ^{13}C NMR shift from HSQC-TEDOR experiment of **Cu-L3** a related calculated value for 10%, 25% and 40% of Hartee-Fock exchange admixture (at 298 K) and for various temperature 298 K and 323 K (using 25% HFX), as well as decomposition of calculated NMR shift (298 K, 25% HFX) to orbital shift ($\delta_{dia,K} = \sigma_{ref} - \sigma_{dia,K}$), Fermi contact ($\sigma_{FC}$) and spin-dipolar ($\sigma_{SD}$) shielding. All values listed in ppm, for atom label see Scheme 1.

Values in ppm:	δ_{exp}	$\delta_{\mathrm{calc}}^{10\%}$	$\delta_{\mathrm{calc}}^{25\%}$	$\delta_{\mathrm{calc}}^{40\%}$	$\delta_{\mathrm{calc}}^{298\mathrm{K}}$	$\delta_{\mathrm{calc}}^{323\mathrm{K}}$	$\delta_{\mathrm{dia},K}$	σ_{FC}	σ_{SD}
H1	2.7	4.32	3.90	3.26	3.90	3.82	2.81	-1.14	0.05
H1'	2.7	4.05	3.67	3.01	3.67	3.61	2.82	-0.90	0.05
H4	27.5	47.06	35.63	29.02	35.63	33.47	7.76	-28.06	0.19
H4'	28.5	44.89	34.39	28.39	34.39	32.33	7.77	-26.83	0.21
H5	ND	-13.70	-9.99	-7.01	-9.99	-8.67	7.13	16.50	0.62
H5'	ND	-13.41	-9.97	-7.17	-9.97	-8.64	7.15	16.46	0.65
H8	9.5	14.27	11.34	11.02	11.34	11.04	7.52	-4.12	0.30
H8'	9.5	13.95	11.44	11.36	11.44	11.14	7.55	-4.22	0.33
H9	ND	645.79	526.92	415.16	526.92	486.79	8.22	-519.47	0.76
H9'	ND	679.57	550.72	431.41	550.72	508.77	8.37	-543.14	0.79
H10	ND	196.70	159.64	122.54	159.64	147.53	3.15	-157.47	0.98
H10'	ND	20.38	28.35	34.68	28.35	26.45	3.84	-24.76	0.26
H11ax	-8.0	-1.93	-1.25	-0.43	-1.25	-0.99	2.08	4.48	-1.15
H11ax'	13.6	18.57	13.04	8.44	13.04	12.15	1.55	-11.91	0.42
H11eq	0.8	2.99	1.62	0.54	1.62	1.62	1.61	0.26	-0.26
H11eq'	0.8	-9.01	-8.11	-6.50	-8.11	-7.29	2.58	10.19	0.51
H12ax	0.8	0.83	0.57	0.35	0.57	0.63	1.36	0.67	0.12
H12ax'	1.1	2.88	1.94	1.29	1.94	1.89	1.30	-0.72	0.07
H12eq	0.8	2.34	2.29	2.26	2.29	2.25	1.82	-0.37	-0.09
H12eq'	8.5	12.40	8.12	5.19	8.12	7.60	1.41	-6.83	0.12
C1	85.3	81.2	78.5	77.7	78.5	78.8	82.2	3.5	0.2

C1'	85.3	81.9	79.4	78.9	79.4	79.6	82.2	2.7	0.2
C2	Q	117.7	107.2	95.2	107.2	105.9	90.1	-17.2	0.1
C2'	Q	114.7	104.7	92.6	104.7	103.5	90.1	-14.7	0.1
C3	Q	113.3	116.6	123.7	116.6	116.4	114.4	-2.6	0.4
C3'	Q	114.9	118.7	126.5	118.7	118.3	114.5	-4.5	0.4
C4	214	268.0	234.5	201.2	234.5	227.9	149.7	-86.3	1.5
C4'	202	255.3	225.0	193.7	225.0	219.2	149.9	-76.7	1.6
C5	ND	1614.5	1284.1	1006.8	1284.1	1194.9	131.6	-1153.8	1.3
C5'	ND	1589.5	1271.0	1002.2	1271.0	1182.9	131.6	-1140.9	1.5
C6	Q	18.2	106.4	171.3	106.4	112.2	181.2	71.0	3.8
C6'	Q	22.9	102.1	159.1	102.1	108.2	180.6	74.2	4.2
C7	Q	22.8	42.6	87.9	42.6	49.0	125.7	80.9	2.3
C7'	Q	23.1	47.2	95.0	47.2	53.2	125.8	76.3	2.4
C8	101	138.5	113.9	97.0	113.9	116.7	150.2	35.2	1.1
C8'	101	150.6	120.8	100.0	120.8	123.1	150.8	28.9	1.2
C9	ND	586.9	416.1	263.5	416.1	397.3	173.0	-248.7	5.6
C9'	ND	491.7	323.1	177.3	323.1	311.5	173.9	-155.3	6.1
C10	ND	-239.3	-276.5	-281.1	-276.5	-249.3	75.1	348.8	2.8
C10'	ND	-244.2	-279.8	-281.8	-279.8	-253.1	65.5	342.6	2.8
C11	33.1	27.4	34.6	44.5	34.6	34.7	35.6	1.3	-0.3
C11'	~240	259.3	241.0	211.8	241.0	224.4	26.5	-215.6	1.1
C12	33.1	36.3	31.1	26.6	31.1	30.9	27.9	-3.2	0.0
C12'	7.8	1.0	1.5	1.9	1.5	2.9	20.3	18.6	0.2

ND – not detected signal, Q - quaternary carbon

Table S3: Results achieved in repeating application of **P-Cu-L1** as heterogeneous catalyst of styrene oxidation.

	Styrene conversion [%]	Selectivity [%]	
		Styrene oxide	Benzaldehyde
1st cycle	80	41	40
2nd cycle	88	30	53
3rd cycle	96	18	51

Příloha číslo 3:

David Šorm, Jiří Brus, Albin Pintar, Jan Sedláček, Sebastijan Kovačič, Hierarchically Porous Polyacetylene Networks: Adsorptive Photocatalysts for Efficient Bisphenol A Removal from Water, *ACS Polymers Au*, **2024**.

ACS
POLYMERS Au
AN OPEN ACCESS JOURNAL OF THE AMERICAN CHEMICAL SOCIETY

pubs.acs.org/polymerau
Article

Hierarchically Porous Polyacetylene Networks: Adsorptive Photocatalysts for Efficient Bisphenol A Removal from Water

David Šorm, Jiří Brus, Albin Pintar, Jan Sedláček, and Sebastijan Kovačič*

Cite This: https://doi.org/10.1021/acspolymersau.4c00032

Read Online

ACCESS | Metrics & More | Article Recommendations | Supporting Information

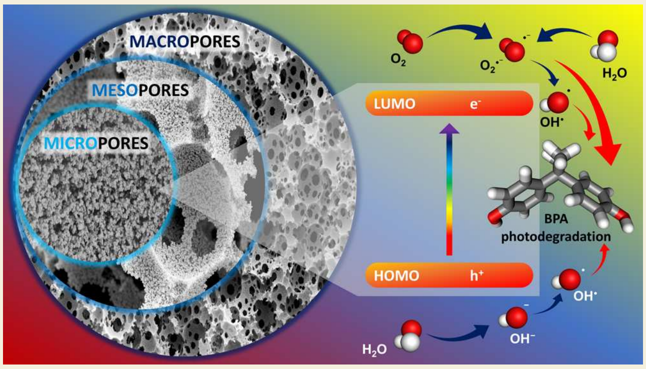

ABSTRACT: In this article, we report a series of functionalized polyacetylene-type networks formed by chain-growth insertion coordination polymerization in high internal phase emulsions (HIPEs). All polymerized HIPEs (polyHIPEs) contain a hierarchically structured, 3D-interconnected porous framework consisting of a micro-, meso- and macropore system, resulting in exceptionally high specific surface areas (up to 1055 $m^2 \cdot g^{-1}$) and total porosities of over 95%. The combination of π-conjugated and hierarchically porous structure in one material enabled the use of these polyacetylene polyHIPEs as adsorptive photocatalysts for the removal of chemical contaminants from water. All polyacetylene polyHIPEs demonstrated high efficiency in the adsorption of bisphenol A from water (up to 48%) and the subsequent photocatalytic degradation. Surprisingly, high adsorption capacity did not affect the photocatalytic efficiency (up to 58%). On the contrary, this dual function seems to be very promising, as some polyacetylene polyHIPEs almost completely removed bisphenol A from water (97%) through the adsorption-photooxidation mechanism. It also appears that the presence of polar functional side groups in the polyacetylene backbone improves the contact of the polyacetylene network with the aqueous bisphenol A solution, which can thus be more easily adsorbed and subsequently oxidized, compensating for the lower specific surface area of some networks, namely, 471 and 308 $m^2 \cdot g^{-1}$ in the case of 3-ethynylphenol- and 3-ethynylaniline-based polyacetylene polyHIPEs, respectively.

KEYWORDS: *polyacetylenes, emulsion-templating, π-conjugated networks, macroporous polymers, heterogeneous photocatalysis*

■ INTRODUCTION

Synthetic chemical contaminants such as per- and polyfluoroalkyl substances (PFAS) or bisphenol A (BPA) and its analogues, to name a few, are persistent, bioaccumulative pollutants found in water resources in low concentrations but with a significant adverse effect on human health.[1] Unless appropriate actions are taken regarding chemical water pollution at both the technological and societal levels, it is estimated that by 2050, more than half of the world's population will be affected by water stress—a situation where demand exceeds the available amount of good quality water.[2]

Considering the environmental persistence, toxicity, and bioaccumulation of synthetic organic contaminants, numerous efforts have been made to remove them from water bodies, including adsorption, filtration, reverse osmosis, enhanced photolysis, electrochemical oxidation, sonochemical destruction, etc.[3] However, many of these methods are expensive or have low removal efficiency due to high energy requirements. The adsorption process remains one of the most cost-effective and environmentally friendly methods. Compared to conventional sorbents, e.g., ion exchange resins, porous material-based adsorbents with a large surface area, large pore volume, and suitable functional groups on the pore surface are the key to success.[4,5] Among them, cryogels have attracted great interest in many studies due to their unique porous structure, high adsorption capacity, and ease of handling, which are valuable properties for various applications, especially for water treatment.[6−9] Another group of porous material-based adsorbents are conjugated porous polymer networks (CPPNs)[10] appear to be very successful in the removal of persistent organic contaminants such as PFAS or bisphenols.[11−13] CPPNs combine attractive properties such as high porosity, large surface area, high stability, and extensive π-conjugation. Since they are predominantly built up using aromatic, rigid monomers as building blocks, their polyarylene-based networks have a sufficient fluorous and hydrophobic affinity, which enables an efficient adsorption capacity, e.g., PFAS or bisphenols,

Received: March 28, 2024
Revised: May 25, 2024
Accepted: May 29, 2024

respectively, through the large surface area.[14,15] In recent years, however, the photocatalytic degradation of water-dissolved synthetic organic contaminants has attracted much attention due to the use of light as a renewable, readily available, and sustainable energy source.[16] In this view, the large π-electron-delocalization of CPPNs is considered key.[17] It enables efficient light absorption and charge carrier transportation, which is advantageous, e.g., for visible-light-driven photocatalysis.[18] When CPPNs are used as photocatalysts, one or more reactive oxygen species, i.e., superoxide radicals ($O_2^{\bullet-}$), hydroxyl radicals ($OH^{\bullet}$), singlet oxygen ($^1O_2$), peroxides (H_2O_2), and photogenerated holes (h^+), are involved in the photooxidation of synthetic organic contaminants.[19] Benefiting from the highly porous and π-electron-delocalized poly(arylene) network structure, CPPNs could therefore be used both as efficient adsorbents for organic contaminants and as heterogeneous photocatalysts for their degradation.[20] This dual function seems to be very promising and offers unprecedented advantages for the treatment of organic contaminants in water. Therefore, it is of utmost interest to design and synthesize novel CPPNs that combine a semiconducting and hierarchically porous framework with various functional groups on the pore surface that facilitate the access of water-dissolved organic contaminants to the interior of the CPPN.

Indeed, conjugated polymerized high internal phase emulsions (HIPEs), referred to as "π-conjugated polyHIPEs",[21,22] are a unique subclass that differs from other CPPNs by having additional porosity on a larger length scale (pore sizes between 1 and 100 μm). PolyHIPEs (PHs) are typically formed by the polymerization of the external (monomeric) phase of HIPEs, resulting in monolithic polymeric materials with unique three-dimensional (3D)-interconnected microcellular morphology.[23−25] Originally, the development of PHs was driven by absorbent applications, in particular the absorption of body fluids,[26,27] and later the adsorption of contaminants from water.[28−31] Recently, however, it has been shown that PHs can be advantageously used as heterogeneous photocatalysts in singlet oxygen generation,[32] organic photoredox reactions,[33,34] photocatalytic sulfoxidation,[35] or as photoinitiators in radical polymerizations.[36] In addition, PHs are also able to photodegrade organic contaminants dissolved in water.[37−39]

Polyacetylene (PA) and its derivatives, $[-HC{=}CR-]_n$ and $[-{}^1RC{=}CR^2-]_n$, are probably the first described well-defined π-conjugated polymers.[40] The π-conjugated nature of these polymers is due to the alternation of single and double bonds between the carbon atoms of the polyene (polyacetylene) main chains. Polyacetylenes are prepared by chain-growth coordination polymerization of acetylene monomers catalyzed by transition-metal complexes operating in metathesis or insertion polymerization mode.[41] The most frequently used Rh(I) insertion catalysts cleave one π bond of the ethynyl group of the monomer, thereby transforming it into an ethenylene group of the monomeric unit incorporated through propagation into a polyene chain.[42−45] The Rh(I) catalysts are highly substrate-selective: they transform only ethynyl groups and, contrary to the metathesis catalysts, do not interact with ethenyl groups. Moreover, the Rh(I) catalysts are well compatible with various heteroatom groups of the components of the polymerization systems and operate well also in the presence of water.[46] As shown earlier, the Rh(I)-catalyzed chain-growth coordination polymerization of acetylene monomers with a higher number of ethynyl groups per molecule leads to the cross-linking of polyacetylene chains and, in optimal cases, also to the formation of a microporous texture of the resulting networks.[47,48]

Herein, we present a simple synthetic strategy that combines high internal phase emulsion (HIPE) templates and rhodium-catalyzed chain-growth coordination polymerization to prepare a series of functionalized conjugated polyacetylene (PA)-based PHs. The rational design of the hierarchically porous framework and the functionalization of the network by incorporating hydrophilic heteroatomic groups enable us the tuning of adsorption capacities and photocatalytic performance of these novel PA−PHs. These bifunctional, i.e., adsorptive and photocatalytically active polymers were then successfully used in the efficient removal of bisphenol A from water.

EXPERIMENTAL METHODS

Materials

The following compounds were used as received: acetylacetonate(norbornadiene)rhodium(I) [Rh(nbd)acac] (>98%), 1,3-diethynylbenzene (>96%), 1,3,5-triethynylbenzene (>98%), 3-ethynylphenol (>98%), 3-ethynylaniline (>98%) (all TCI Europe), Span80 (sorbitan monooleate, MW = 428 g·mol^{-1}, Merck Life Science), calcium chloride dihydrate (99%, Merck Life Science), toluene for analysis (Merck), tetrahydrofuran (≥99%, Sigma-Aldrich), bisphenol A (BPA, c_0 = 10 mg·L^{-1}, 100 mL, Aldrich). *N*-Salicylidene(3-ethynylaniline) was prepared according to ref 49 from 3-ethynylaniline and salicylaldehyde (≥99%, Merck Life Science).

Synthesis of PA−PH Networks

(Co)monomer(s) was/were dissolved in dry toluene ($c_{monomer}$ = 1.7 mol·dm^{-3}). Surfactant Span80 (sorbitan monooleate, MW = 428 g·mol^{-1}) was added to the solution of (co)monomer(s) and properly stirred on the magnetic stirrer. The amount of the surfactant was 15 wt % of the whole solution of (co)monomer(s), including the weight of the solvent. Solution of 1 wt % $CaCl_2$ in H_2O was added dropwise into the solution of (co)monomer(s) (for amount, see the Result and Discussion section) accompanied by intensive stirring. The reaction mixture was stirred for another 20 min to form a uniform emulsion. After that, the stirrer bar was removed and the solution of polymerization initiator [Rh(nbd)acac] in toluene was added to the emulsion. The emulsion was immediately smoothly shaken and the whole reaction mixture was put into the oven at 75 °C for 48 h. During this period, the solid polymer network occurred as a monolith. It should be noted that the HIPEs stopped flowing within minutes of adding the initiator, indicating that gelation occurred very quickly. The gelation was followed by using the vial inversion method. The monolith was isolated and washed in tetrahydrofuran by diffusion for 48 h with frequent exchanges of the solvent. In the end, the product was dried on air at room temperature.

Adsorption of Bisphenol A

The BPA adsorption was carried out in a batch slurry reactor (Lenz, Wertheim, Germany, model LF60, 250 mL) equipped with a heating/cooling jacket. PA−PH samples were put in contact with 100 mL of aqueous solution, containing the known concentration of BPA (c_0 = 10 mg·L^{-1}) wherein 12.5 mg of PA−PH pieces were suspended. The vessel content was thermostated (Julabo F25/ME) at a selected constant temperature (15 °C) with intermittent mixing until equilibration (∼16 h). The BPA concentration in the supernatant was determined with an HPLC instrument (Thermo Scientific, Waltham, MA, model Spectra). The BPA concentration as a function of time was followed at the characteristic BPA wavelength (λ = 210 nm).

Photocatalytic Degradation of Bisphenol A

Photocatalytic experiments were performed in a batch slurry reactor (Lenz, Wertheim, Germany, model LF60, 250 mL). In all runs, an aqueous solution (ultrapure water, 18.2 MΩ·cm) of bisphenol A (BPA, c_0 = 10 mg·L^{-1}, Aldrich) was used. The concentration of the added catalyst was 125 mg·L^{-1}. In the middle of the batch slurry reactor, a

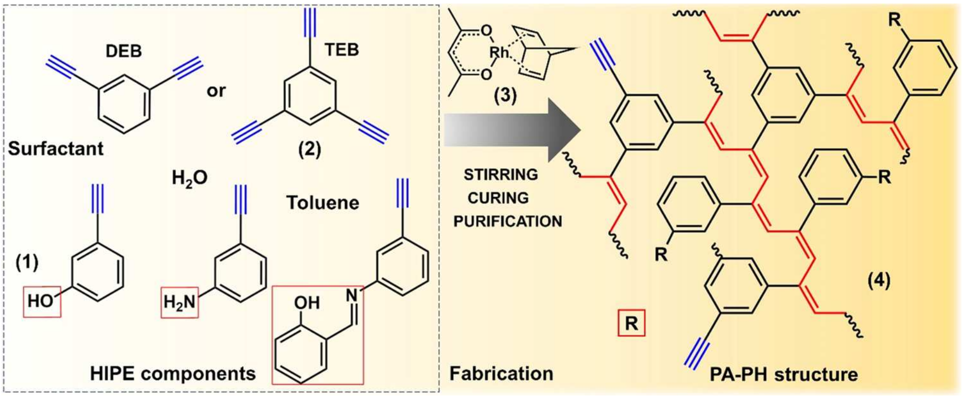

Figure 1. Schematic illustrations of the synthesis of PA−PH networks.

water-cooled quartz jacket with a visible lamp (Philips 150 W halogen lamp, λ_{max} = 520 nm) was immersed vertically. This enabled us to completely illuminate the BPA solution. To ensure that the catalyst was illuminated only by visible light, a UV cutoff filter at λ = 410 nm from Rosco (E-Color #226: U.V. filter) was used. The degradation of BPA was analyzed with an HPLC instrument (Thermo Scientific, Waltham, MA, model Spectra). The chemical robustness of PA-TEB network was investigated, and the mm-sized pieces were suspended in water purged with air and illuminated with a visible lamp for 24 h. The polymer pieces were then filtered and dried. The water was analyzed by HPLC, while the polymer pieces were subjected to ^{13}C CP/MAS NMR.

The amount of BPA adsorbed or oxidized was expressed as the removal percentage and calculated by the equation:

$$\%\text{removal} = [(C_i - C_f)/C_i]\cdot 100$$

where C$_i$ and C$_f$ are the initial and final concentrations of contaminants, respectively.

Methods of Characterization

The ^{13}C CP/MAS spectra were recorded at 16.4 T using a Bruker Avance NEO 700 SB NMR spectrometer (Karlsruhe, Germany, 2021) with a 3.2 mm probe head. The MAS frequency was set to 18−20 kHz. The cross-polarization contact time was usually 2 ms, and the dipolar decoupling SPINAL64 was applied during the data acquisition. The number of scans was 256−4000 to reach an acceptable signal-to-noise ratio. The ^{13}C scale is referenced to crystalline γ-glycine (176.03 ppm for ^{13}C). Considering that the cross-polarization efficiency for a given CP contact time is different for different functional groups, the presented quantitative analysis is subject to a certain error (uncertainty). The test based on the comparison of the routinely recorded ^{13}C CP/MAS NMR spectrum with the spectrum recorded with a single-pulse excitation (duration of the ^{13}C 90deg pulse was 3 μs) and a very long repetition delay (60 s) showed that this experimental error is about ±5−6%. A PerkinElmer FTIR spectrometer (model Frontier) was used for measurements of FTIR spectra. The spectra (average of 32 scans, resolution 4 cm^{-1}) were recorded using attenuated total reflection (ATR) in the range of 400−4000 cm^{-1}. Scanning electron microscopy images (SEM) were performed on a JWS-7515, JEOL Ltd. scanning electron microscope. The samples were attached to a carbon tab for better conductivity, and afterward, a thin layer of Pt was sputtered on a sample's surface prior to scanning analysis (for SEM investigations). SEM micrographs were taken at a magnification of 5000 times, at a 7 mm working distance, and 20 kV voltage applied. The adsorption and desorption isotherms of N$_2$ were obtained at −196 °C using a Micromeritics TriStar II 3020 instrument. Prior to measurements, the samples were degassed under N$_2$ stream (purity 6.0) using a programmed bilevel heating, with the first heating stage at 90 °C for 60 min, followed by the second heating stage at 110 °C for 240 min. The specific surface area of the samples was calculated by applying the BET theory to the nitrogen adsorption data within the 0.06−0.30 p/p_0 range. The polyHIPE densities (ρ_{PH}) were determined gravimetrically and then the porosities were calculated assuming a polymer (skeletal) density (ρ_P) of 1.13 g·cm^{-3} according to the following equation:

$$P = (1 - \rho_{PH}/\rho_P)\cdot 100$$

UV−vis DR spectroscopy was performed on a PerkinElmer Lambda 35 UV−vis spectrophotometer equipped with the RSA-PE-19 M Praying Mantis accessory for powdered samples in order to record the UV−vis diffuse reflectance spectra of the prepared materials. The background correction was performed with a white reflectance standard Spectralon© (range of 200−900 nm). The optical band gap energies were determined using the Kubelka−Munk theory and Tauc plot as described by Macyk et al.[50]

■ RESULTS AND DISCUSSION

Synthesis of Polyacetylene-Based PolyHIPE Networks

Building on our previous work incorporating 1,3-diethynylbenzene into a conjugated polyHIPE network,[22] we set out to synthesize a library of polyacetylene-based polyHIPEs (PA−PH). 1,3-Di- and 1,3,5-triethynylbenzene monomers were homopolymerized to form nonfunctionalized PA−PH networks, abbreviated as PA-DEB and PA-TEB, respectively, while 3-ethynylphenol, 3-ethynylaniline, or *N*-salicylidene(3-ethynylaniline) monomers were copolymerized with two equivalents of 1,3,5-triethynylbenzene and formed networks, abbreviated as PA-OH, PA-NH$_2$, and PA-SAL, respectively (Figure 1). The chain-growth coordination polymerization was used as polymerization chemistry with the mononuclear Rh(I) complex as the initiator. The networks produced consisted of π-conjugated PA chains hyper-cross-linked by benzenediyl and benzenetriyl links. To optimize the emulsion polymerization using the Rh(I)-catalyzed polymerization chemistry, a series of experimental parameters were investigated, such as the toluene−water phase ratio (set to ∼0.80), concentrations of the (co)monomers (1.7 mol·dm^{-3}), initiator loading the (total concentration of the initiator differed according to the average number of ethynyl groups per (co)monomer molecule, so in all cases, 0.03 mol of initiator per mole of ethynyl groups were used), and the amount of surfactant (15 wt % according to the continuous phase of HIPE). The polymerization between (**1**) and (**2**) in the external (monomeric) phase took place immediately after the addition of (**3**) to the HIPE and resulted in a polyacetylene-based PH network (**4**) (Figure 1). In all cases, gelation was very rapid, with the HIPEs stopped to flow within minutes, even at room temperature. Due to the rapid gelation, the catalyst solution was only added at the end of the emulsion preparation, which gave us a few extra minutes to homogenize the HIPE and transfer it into a suitable mold. Final curing at 75 °C and subsequent purification/drying resulted in a brown, lightweight, and monolithic PA−PH. The gel formation was additionally confirmed by immersing the selected samples in liquid nitrogen when a point of apparent gelation had reached (the HIPEs stopped flowing) and then adding a large amount of dichloromethane. The samples did not dissolve, clearly indicating the formation of a chemically cross-linked gel. The polymerization yields were evaluated by setting the mass of dried monoliths relative to the mass of monomers and all PA−PH networks were prepared in quantitative yields, indicating a highly efficient Rh(I)-initiated polymerization in a two-phase HIPE system (Table 1).

Table 1. Characterization Data of Polyacetylene-Based PolyHIPEs

sample	PA-OH	PA-NH$_2$	PA-SAL	PA-TEB	PA-DEB
P [%][a]	95	96	95	97	96
ρ_{PH} [g·cm^{-3}][b]	0.05	0.04	0.05	0.03	0.04
d_V [μm][c]	24 ± 5	23 ± 4	16 ± 3	24 ± 3	15 ± 2
S_{BET} [m^2·g^{-1}][d]	471	308	273	1055	449
V_{mic} [cm^3·g^{-1}][e]	0.18	0.12	0.11	0.41	0.18

[a] Porosity. [b] PH density. [c] Av. void size estimated from SEM images. [d] Specific surface area. [e] Volume of micropores determined from the N_2 physisorption analysis.

Molecular and Porous Structure

As evidenced by FTIR and ^{13}C CP/MAS NMR analyses, all PA−PHs consist of a typical arene-linked polyacetylene network motif. The FTIR spectra (Figure S1) show the bands associated with the benzene cross-linking and side units and the ethenylene units of the main chains in the range of 500−900 cm^{-1} and 1500−1600 cm^{-1}, respectively. The presence of a certain amount of unconverted ethynyl side groups in the PA−PH networks was clearly confirmed by the bands at around 3300 cm^{-1} (and 2110 cm^{-1}). ^{13}C CP/MAS NMR spectra of all PA−PH networks together with their structures are shown in Figure 2. All networks showed broad, partially resolved signals in the region 115−150 ppm corresponding to aromatic carbons and carbons of the polyene main chain. The ^{13}C CP/MAS NMR further confirmed the presence of substituents (−OH, −NH$_2$, −CH═N−) attached to the benzene rings in copolymer networks by the characteristic signals of the aromatic carbon atoms in the vicinity of these groups: in PA-OH spectrum at 156 ppm ($\underline{C}_{Ar}$−OH) and 115 ppm ($\underline{C}_{Ar}$-C_{Ar}−OH), in PA-NH$_2$ spectrum shoulder at 146 ppm ($\underline{C}_{Ar}$−NH$_2$) and 114 ppm ($\underline{C}_{Ar}$-C_{Ar}-NH$_2$) and in PA-SAL spectrum at 161 ppm (−H$\underline{C}$═N−C_{Ar}) and 119 ppm ($\underline{C}_{Ar}$-C_{Ar}−OH). In the ^{13}C CP/MAS NMR spectra of all networks obtained with TEB, a signal at about 83 and 76 ppm is clearly visible, which is due to the unreacted ethynyl carbon atoms. The average content was estimated to be 0.8 unreacted ethynyl groups per 1,3,5-triethynylbenzene monomer unit in PA-TEB. In contrast, almost complete conversion of ethynyl groups was observed in PA-DEB (Figure 2). In both systems, a new signal appears at δ = 140 ppm, which can be attributed to the carbons in the polyene backbone (Figure S2).

The porous structures typical of PHs are shown in Figure 3. Analysis by SEM revealed that the HIPE structure was templated within the PA−PHs and all had a 3D-interconnected microcellular morphology with an average void size between 15 ± 2 and 24 ± 5 μm, respectively. SEM analysis further revealed small macropores with diameters of about 200 nm within the polymer matrix, forming a hierarchical porous system (Figure S3). The PH densities (ρ_{PH}) were relatively low and varied between 0.03 and 0.05 g·cm^{-3}, suggesting the presence of even smaller pores, i.e., in the meso- or microlength scale (vide infra) (Table 1). The total porosities (P) of the PA−PHs were calculated from the ρ_{PH} by assuming a skeletal density (ρ_P) of 1.13 g·cm^{-3} for trans-PA[51] and were surprisingly high for 80% of the internal phase content, i.e., ≥95% (Table 1). The porous properties and associated specific surface areas (S_{BET}) were further analyzed using nitrogen adsorption−desorption measurements. All PA−PHs showed a typical type II isotherm with a steep increase at $p/p_0 \approx 1$ due to the presence of macropores, and an additional increase in N_2 uptake up to 0.1 p/p_0, indicating the presence of micropores. The volume of the micropores was determined between 0.11 and 0.41 cm^3·g^{-1} (derived from the N_2 isotherms; Table 1) and, as expected, reflected in the S_{BET}. The highly cross-linked PA-TEB network, which had the highest micropore volume (0.41 cm^3·g^{-1}), exhibited S_{BET} of 1055 m^2·g^{-1} while approximately half S_{BET} (449 m^2·g^{-1}) and half micropore volume (0.18 cm^3·g^{-1}) was found for PA-DEB. Functionalized

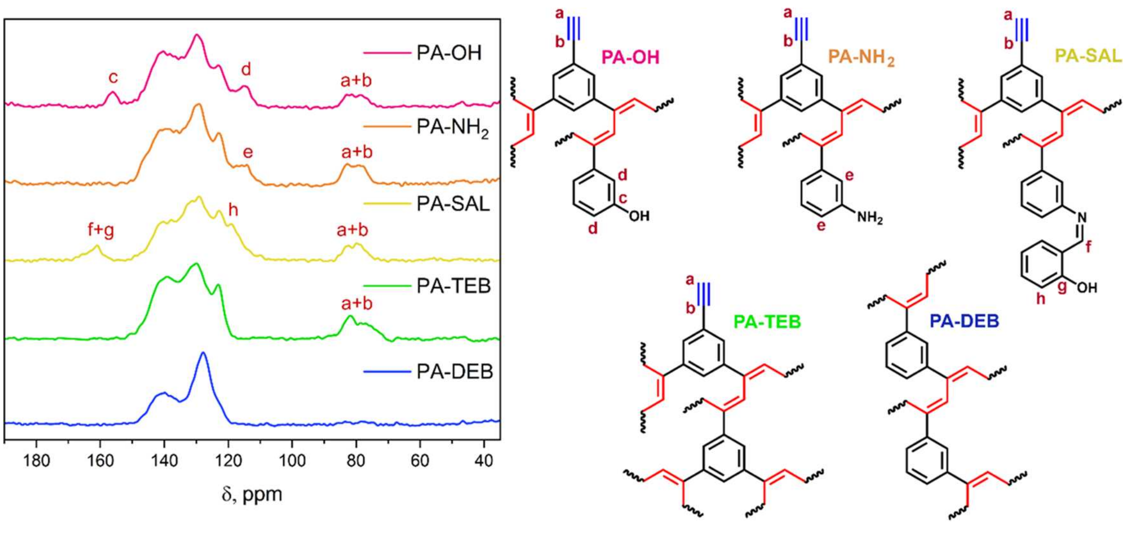

Figure 2. ^{13}C CP/MAS NMR spectra of prepared PA−PH networks.

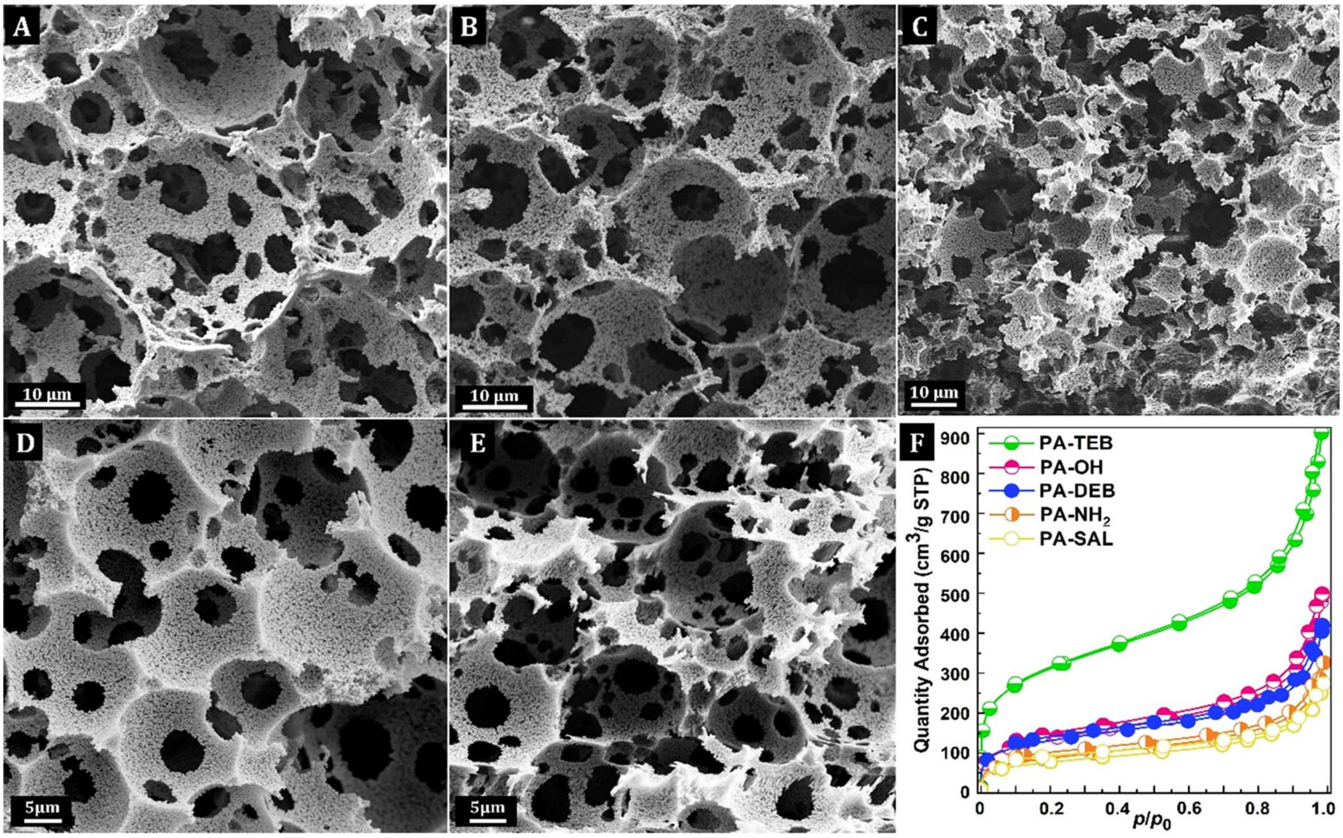

Figure 3. Porous structures (SEM) of (A) PA-OH; (B) PA-NH_2; (C) PA-SAL; (D) PA-TEB; (E) PA-DEB; and (F) N_2 adsorption−desorption isotherms of PA−PHs.

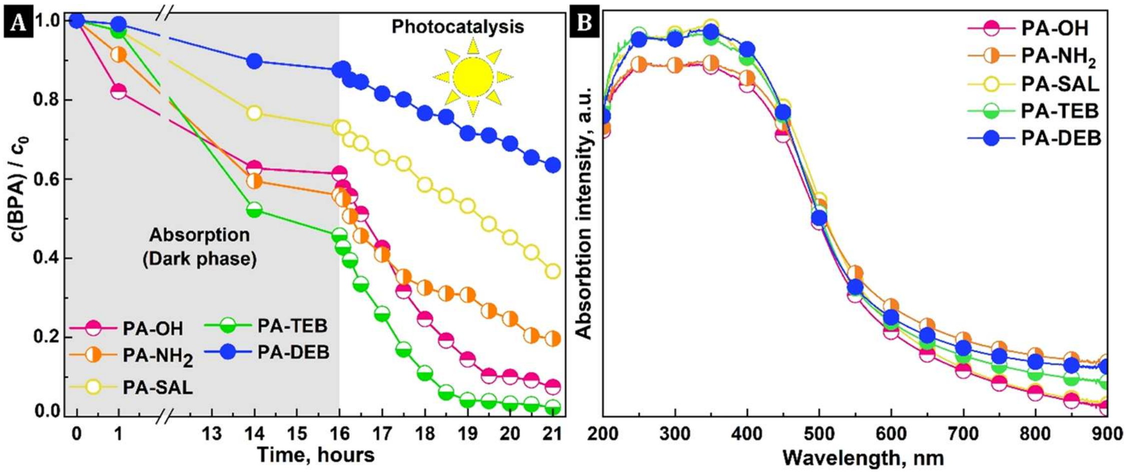

Figure 4. (A) Adsorption and visible-light-driven photooxidation of water-dissolved BPA and (B) UV−vis DRS analysis of the PA−PHs.

copolymer networks PA-OH, PA-NH_2, and PA-SAL revealed S_{BET} of up to 471 $m^2 \cdot g^{-1}$ with micropore volumes between 0.11 and 0.18 $cm^3 \cdot g^{-1}$ (Figure 3F).

Removal of Bisphenol A (BPA) by Adsorption and Photooxidation

The high surface area and the π-conjugated nature of the polyacetylene networks enable PA−PHs to function as an adsorptive photocatalyst, i.e., simultaneously as an adsorbent and photocatalyst (Figure S4). To investigate the adsorption performance of PA−PHs, we first carried out an adsorption test in which the BPA concentrations in the supernatant were measured at different time intervals, as shown in Figure 4A (dark adsorption phase). The removal of BPA for PA-DEB, PA-TEB, PA-SAL, PA-NH_2, and PA-OH reached about 1, 2, 3, 9, and 18% within the first hour and 11, 48, 24, 41, and 38% within 14 h when we are slowly reaching the adsorption plateau (except for PA-TEB which probably requires more time for adsorption equilibrium). Adsorption tests suggest that the specific surface area, π-conjugation, and the functional groups on the pore surface affect the amount of adsorbed BPA. The first rationale for the BPA adsorption on the surface of PA-DEB and PA-TEB, which is particularly high in the case of PA-TEB, is as follows. In addition to the strong hydrophobic effect, that often drives the adsorption of pure hydrocarbon networks, the high π-electron polarizability at the surfaces, similar to the PA network, has also proven to be an important factor in the adsorption of aromatic organic pollutants. In the literature, this phenomenon is known as $\pi-\pi$ electron donor−acceptor (EDA) interaction[52−55] and is based on the interaction between the π-electron-poor regions (considered as π-acceptors) and electron-rich aromatic organic molecules (considered as π-donors). The high adsorption of BPA on the surface of PA-TEB is therefore mostly due to the $\pi-\pi$ electron coupling between the π-electron-rich region in the PA network and the electron-poor benzene rings of BPA. On the other hand, adsorption in the case of PA-OH, PA-NH_2, and PA-SAL is driven by other mechanisms. It is interesting that PA-OH (471 $m^2 \cdot g^{-1}$) and PA-NH_2 (308 $m^2 \cdot g^{-1}$) have a similar S_{BET} to the PA-DEB network (449 $m^2 \cdot g^{-1}$), but their adsorption capacities are similar to those of PA-TEB. Apparently, the N- and O-heteroatoms in the PA-NH_2 and PA-OH networks function as active sites on the surface that enable efficient BPA removal by combining $\pi-\pi$ electron coupling with the (weak) hydrogen bonding interaction mechanism.[48,56−59]

Next, PA−PHs were investigated as heterogeneous photocatalysts for visible-light-driven photooxidation of BPA dissolved in water. First, UV−vis diffuse reflectance spectroscopy was used to study the light-harvesting ability of PA−PHs and revealed that all are visible-light-active materials. The UV−vis DRS spectra display a broad band with a maximum of around 350 nm and corresponding optical absorption band edges between 612 and 630 nm (Figure 4B). The band gaps were determined through Kubelka−Munk transformed reflectance spectra. The Tauc plots depicted in Figure S5 indicate that the optical band gaps are in the range of 2.2−2.3 eV. The photocatalytic activities of the PA−PH networks in the BPA photooxidation were then investigated as shown in Figure 4A. A typical photocatalysis experiment was performed with the addition of 12.5 mg of a network as a catalyst to 100 mL of aqueous BPA solution (c_{BPA} = 10 $mg \cdot dm^{-3}$). In the first step (dark adsorption phase), only the adsorption of BPA on the catalyst surface took place, followed by the photocatalysis phase, in which the reaction system was illuminated with visible light (λ > 420 nm). As shown in Figure 4A, PA-DEB, PA-TEB, PA-SAL, PA-NH_2, and PA-OH showed activity in which 24, 43, 37, 38, and 58% of BPA was removed by oxidation in 5 h of illumination, respectively (decrease of the BPA concentration during the light phase). Since hydroxyl radicals ($OH^\bullet$) are the most reactive oxidizing species in the degradation of organic pollutants, their formation was monitored during the photoexcitation of PA−PHs in the presence of the fluorescent probe molecule coumarin (COUM). COUM reacts with $OH^\bullet$ radicals to form 7-hydroxycoumarin (7-OHC); therefore, the fluorescence intensity of 7-OHC can be related to the amount of $OH^\bullet$ radicals produced by a given catalyst sample.[60] The results of the coumarin oxidation experiments performed by illuminating the PA-OH and PA-NH_2 networks with visible light are shown in Figure S6. The results confirm that both networks can generate $OH^\bullet$ radicals under visible-light illumination. Finally, two control experiments were performed, namely, COUM oxidation in the absence of the polyHIPE photocatalyst and the stability of the polyHIPE photocatalyst under photooxidation conditions (see the Experimental Section). The control experiment without PA-OH and PA-NH_2 photocatalyst showed no photooxidation of COUM to 7-OHC, while the PA-TEB network exhibited high chemical robustness, as HPLC and ^{13}C CP/MAS NMR analyses confirmed that neither segments were leached from the network into the water, nor the covalent structure was altered under photooxidation conditions.

Considering both the adsorption and photooxidation activity (Figure 4), all PA−PHs are excellent adsorptive photocatalysts. The adsorption of BPA on the pore surface had no effect on the further photocatalytic efficiency, and in the case of PA-TEB, we even succeeded in completely removing BPA from the aqueous solution.

CONCLUSIONS

In summary, a series of polyacetylene-based polyHIPEs were prepared by insertion coordination polymerization of HIPE templates. All were hierarchically porous polymers with micropore volumes between 0.11 and 0.41 $cm^3 \cdot g^{-1}$ and exhibited high S_{BET} values (273−1055 $m^2 \cdot g^{-1}$). All PA−PHs also exhibit significant semiconducting properties, such as a strong light-harvesting ability in the visible-light region with optical band gaps in the range of 2.20−2.33 eV. The porosity and electronic properties can be adjusted by selecting suitable building blocks. The PA−PHs were then used to remove BPA from water and achieved near-quantitative adsorption/photooxidation efficiency. The PA-TEB, a pure hydrocarbon network, with the highest S_{BET} (1055 $m^2 \cdot g^{-1}$) showed the highest BPA adsorption activity. On the other hand, PA-OH and PA-NH_2 networks with significantly lower S_{BET} (471 and 308 $m^2 \cdot g^{-1}$, respectively) revealed similar adsorption capacities, which can be attributed to the polar functional groups on the pore surface. Importantly, this high adsorption capacity did not affect the subsequent photocatalytic activity. All PA−PHs were also used effectively for BPA photooxidation in water, with between 24 and 58% of BPA being successfully degraded. Due to their highly porous and π-electron-delocalized polyacetylene network structure, PA−PHs have therefore been successfully used both as an efficient adsorbent for BPA and as a heterogeneous photocatalyst for its degradation.

ASSOCIATED CONTENT

Supporting Information

The Supporting Information is available free of charge at https://pubs.acs.org/doi/10.1021/acspolymersau.4c00032.

Procedures and details about characterization and description of adsorption/photooxidation (PDF)

AUTHOR INFORMATION

Corresponding Author

Sebastijan Kovačič − *Department of Inorganic Chemistry and Technology, National Institute of Chemistry, SI-1001 Ljubljana, Slovenia; Faculty of Chemistry and Chemical Engineering, University of Maribor, SI-2000 Maribor, Slovenia;* orcid.org/0000-0003-2664-9791; Email: sebastijan.kovacic@um.si

Authors

David Šorm − *Department of Physical and Macromolecular Chemistry, Faculty of Science, Charles University, Prague 2 128 43, Czech Republic;* orcid.org/0000-0001-9969-322X

Jiří Brus − *Institute of Macromolecular Chemistry, Czech Academy of Sciences, 162 00 Prague, Czech Republic;* orcid.org/0000-0003-2692-612X

Albin Pintar − *Department of Inorganic Chemistry and Technology, National Institute of Chemistry, SI-1001 Ljubljana, Slovenia*

Jan Sedláček − *Department of Physical and Macromolecular Chemistry, Faculty of Science, Charles University, Prague 2 128 43, Czech Republic*

Complete contact information is available at:
https://pubs.acs.org/10.1021/acspolymersau.4c00032

Author Contributions

The manuscript was written through contributions of all authors. All authors have given approval to the final version of the manuscript.

Notes

The authors declare no competing financial interest.

■ ACKNOWLEDGMENTS

This work was supported by the Ministry of Higher Education, Science and Innovation of the Republic of Slovenia and the Slovenian Research and Innovation Agency (grant P2-0150). J.S. acknowledges the financial support from the Czech Science Foundation (project no. 21-02183S). S.K. acknowledges the financial support of Horizon Europe project UPSTREAM (GA 10112877).

■ REFERENCES

(1) Fang, W.; Peng, Y.; Muir, D.; Lin, J.; Zhang, X. A Critical Review of Synthetic Chemicals in Surface Waters of the US, the EU and China. *Environ. Int.* **2019**, *131*, No. 104994.

(2) Dolan, F.; Lamontagne, J.; Link, R.; Hejazi, M.; Reed, P.; Edmonds, J. Evaluating the Economic Impact of Water Scarcity in a Changing World. *Nat. Commun.* **2021**, *12* (1), No. 1915, DOI: 10.1038/s41467-021-22194-0.

(3) Yadav, S.; Ibrar, I.; Al-Juboori, R. A.; Singh, L.; Ganbat, N.; Kazwini, T.; Karbassiyazdi, E.; Samal, A. K.; Subbiah, S.; Altaee, A. Updated Review on Emerging Technologies for PFAS Contaminated Water Treatment. *Chem. Eng. Res. Des.* **2022**, *182*, 667−700.

(4) Wu, J.; Xu, F.; Li, S.; Ma, P.; Zhang, X.; Liu, Q.; Fu, R.; Wu, D. Porous Polymers as Multifunctional Material Platforms toward Task-Specific Applications. *Adv. Mater.* **2019**, *31* (4), No. 1802922.

(5) Waheed, A.; Baig, N.; Ullah, N.; Falath, W. Removal of Hazardous Dyes, Toxic Metal Ions and Organic Pollutants from Wastewater by Using Porous Hyper-Cross-Linked Polymeric Materials: A Review of Recent Advances. *J. Environ. Manage.* **2021**, *287*, No. 112360.

(6) Plieva, F. M.; Kirsebom, H.; Mattiasson, B. Preparation of Macroporous Cryostructurated Gel Monoliths, Their Characterization and Main Applications. *J. Sep. Sci.* **2011**, *34* (16−17), 2164−2172.

(7) Türkmen, D.; Bakhshpour, M.; Akgönüllü, S.; Aşır, S.; Denizli, A. Heavy Metal Ions Removal From Wastewater Using Cryogels: A Review. *Front. Sustainability* **2022**, *3*, No. 126382, DOI: 10.3389/frsus.2022.765592.

(8) Baimenov, A.; Berillo, D. A.; Poulopoulos, S. G.; Inglezakis, V. J. A Review of Cryogels Synthesis, Characterization and Applications on the Removal of Heavy Metals from Aqueous Solutions. *Adv. Colloid Interface Sci.* **2020**, *276*, No. 102088.

(9) Loo, S.-L.; Lim, T.-T.; Krantz, W. B.; Fane, A. G.; Hu, X. Potential Evaluation and Perspectives on Using Sponge-like Superabsorbent Cryogels for Onsite Water Treatment in Emergencies. *Desalination Water Treat* **2015**, *53* (6), 1506−1515.

(10) Yang, L.; Peng, Y.; Luo, X.; Dan, Y.; Ye, J.; Zhou, Y.; Zou, Z. Beyond C3N4 π-Conjugated Metal-Free Polymeric Semiconductors for Photocatalytic Chemical Transformations. *Chem. Soc. Rev.* **2021**, *50* (3), 2147−2172.

(11) Xiao, L.; Ling, Y.; Alsbaiee, A.; Li, C.; Helbling, D. E.; Dichtel, W. R. β-Cyclodextrin Polymer Network Sequesters Perfluorooctanoic Acid at Environmentally Relevant Concentrations. *J. Am. Chem. Soc.* **2017**, *139* (23), 7689−7692.

(12) Ji, W.; Xiao, L.; Ling, Y.; Ching, C.; Matsumoto, M.; Bisbey, R. P.; Helbling, D. E.; Dichtel, W. R. Removal of GenX and Perfluorinated Alkyl Substances from Water by Amine-Functionalized Covalent Organic Frameworks. *J. Am. Chem. Soc.* **2018**, *140* (40), 12677−12681.

(13) Klemes, M. J.; Ling, Y.; Ching, C.; Wu, C.; Xiao, L.; Helbling, D. E.; Dichtel, W. R. Reduction of a Tetrafluoroterephthalonitrile-β-Cyclodextrin Polymer to Remove Anionic Micropollutants and Perfluorinated Alkyl Substances from Water. *Angew. Chem., Int. Ed.* **2019**, *58* (35), 12049−12053.

(14) Sapurina, I. Yu.; Shishov, M. A.; Ivanova, V. T. Sorbents for Water Purification Based on Conjugated Polymers. *Russ. Chem. Rev.* **2020**, *89* (10), 1115.

(15) Su, Y.; Wang, F.; Wu, S.; Fan, Y.; Bai, W.; Wang, S.; Sun, H.; Zhu, Z.; Liang, W.; Li, A. Template-Assisted Preparation of Conjugated Microporous Polymers Membranes for Selective Separation. *Sep. Purif. Technol.* **2021**, *259*, No. 118203.

(16) Wang, T.-X.; Liang, H.-P.; Anito, D. A.; Ding, X.; Han, B.-H. Emerging Applications of Porous Organic Polymers in Visible-Light Photocatalysis. *J. Mater. Chem.* **2020**, *8* (15), 7003−7034.

(17) Zhang, T.; Xing, G.; Chen, W.; Chen, L. Porous Organic Polymers: A Promising Platform for Efficient Photocatalysis. *Mater. Chem. Front.* **2020**, *4* (2), 332−353.

(18) Byun, J.; Zhang, K. A. I. Designing Conjugated Porous Polymers for Visible Light-Driven Photocatalytic Chemical Transformations. *Mater. Horiz.* **2020**, *7* (1), 15−31.

(19) Chen, W.; Chen, P.; Zhang, G.; Xing, G.; Feng, Y.; Yang, Y.-W.; Chen, L. Macrocycle-Derived Hierarchical Porous Organic Polymers: Synthesis and Applications. *Chem. Soc. Rev.* **2021**, *50* (20), 11684−11714.

(20) Wang, B.; Xie, Z.; Li, Y.; Yang, Z.; Chen, L. Dual-Functional Conjugated Nanoporous Polymers for Efficient Organic Pollutants Treatment in Water: A Synergistic Strategy of Adsorption and Photocatalysis. *Macromolecules* **2018**, *51* (9), 3443−3449.

(21) Zhang, K.; Vobecka, Z.; Tauer, K.; Antonietti, M.; Vilela, F. π-Conjugated PolyHIPEs as Highly Efficient and Reusable Heterogeneous Photosensitizers. *Chem. Commun.* **2013**, *49* (95), 11158−11160.

(22) Slováková, E.; Ješelnik, M.; Žagar, E.; Zedník, J.; Sedláček, J.; Kovačič, S. Chain-Growth Insertion Polymerization of 1,3-Diethynylbenzene High Internal Phase Emulsions into Reactive π-Conjugated Foams. *Macromolecules* **2014**, *47* (15), 4864−4869.

(23) Cameron, N. R.; Sherrington, D. C. High Internal Phase Emulsions (HIPEs)—Structure, Properties and Use in Polymer Preparation. In *Biopolymers Liquid Crystalline Polymers Phase Emulsion*; Springer Berlin Heidelberg: Berlin, Heidelberg, 1996; pp 163−214 DOI: 10.1007/3-540-60484-7_4.

(24) Stubenrauch, C.; Menner, A.; Bismarck, A.; Drenckhan, W. Emulsion and Foam Templating—Promising Routes to Tailor-Made Porous Polymers. *Angew. Chem., Int. Ed.* **2018**, *57* (32), 10024−10032.

(25) Zhang, T.; Sanguramath, R. A.; Israel, S.; Silverstein, M. S. Emulsion Templating: Porous Polymers and Beyond. *Macromolecules* **2019**, *52* (15), 5445−5479.

(26) Mork, S. W.; Malone, B. A. Continuous Process for Polymerizing, Curing and Drying High Internal Phase Emulsions Background of the Invention. US6299808B1, 2001.

(27) Barby, D.; Haq, Z. Low Density Porous Cross-Linked Polymeric Materials and Their Preparation. EP0060138B1, 1986.

(28) Kovačič, S.; Silverstein, M. S. Superabsorbent, High Porosity, PAMPS-Based Hydrogels through Emulsion Templating. *Macromol. Rapid Commun.* **2016**, *37* (22), 1814−1819.

(29) Kovačič, S.; Drašinac, N.; Pintar, A.; Žagar, E. Highly Porous Cationic Polyelectrolytes via Oil-in-Water Concentrated Emulsions: Synthesis and Adsorption Kinetic Study. *Langmuir* **2018**, *34* (35), 10353−10362.

(30) Cegłowski, M.; Schroeder, G.; Hoogenboom, R. Porous Poly(2-Oxazoline)-Based Polymers for Removal and Quantification of Phenolic Compounds. *Chem. Mater.* **2020**, *32* (15), 6425−6436.

(31) Jurjevec, S.; Žagar, E.; Kovačič, S. Functional Macroporous Amphoteric Polyelectrolyte Monoliths with Tunable Structures and Properties through Emulsion-Templated Synthesis. *J. Colloid Interface Sci.* **2020**, *575*, 480−488.

(32) Tobin, J. M.; McCabe, T. J. D.; Prentice, A. W.; Holzer, S.; Lloyd, G. O.; Paterson, M. J.; Arrighi, V.; Cormack, P. A. G.; Vilela, F. Polymer-Supported Photosensitizers for Oxidative Organic Transformations in Flow and under Visible Light Irradiation. *ACS Catal.* **2017**, *7* (7), 4602−4612.

(33) Wang, Z. J.; Ghasimi, S.; Landfester, K.; Zhang, K. A. I. A Conjugated Porous Poly-Benzobisthiadiazole Network for a Visible Light-Driven Photoredox Reaction. *J. Mater. Chem.* **2014**, *2* (44), 18720−18724.

(34) Wang, Z. J.; Ghasimi, S.; Landfester, K.; Zhang, K. A. I. Highly Porous Conjugated Polymers for Selective Oxidation of Organic Sulfides under Visible Light. *Chem. Commun.* **2014**, *50* (60), 8177−8180.

(35) Kotnik, T.; Žerjav, G.; Pintar, A.; Žagar, E.; Kovačič, S. Highly Porous Poly(Arylene Cyano-Vinylene) Beads Derived through the Knoevenagel Condensation of the Oil-in-Oil-in-Oil Double Emulsion Templates. *ACS Macro. Lett.* **2021**, *10* (10), 1248−1253.

(36) Wang, Z. J.; Landfester, K.; Zhang, K. A. I. Hierarchically Porous π-Conjugated PolyHIPE as a Heterogeneous Photoinitiator for Free Radical Polymerization under Visible Light. *Polym. Chem.* **2014**, *5* (11), 3559−3562.

(37) Jurjevec, S.; Žerjav, G.; Pintar, A.; Žagar, E.; Kovačič, S. Tunable Poly(Aryleneethynylene) Networks Prepared by Emulsion Templating for Visible-Light-Driven Photocatalysis. *Catal. Today* **2021**, *361*, 146−151.

(38) Kotnik, T.; Žerjav, G.; Pintar, A.; Žagar, E.; Kovačič, S. Azine- and Imine-Linked Conjugated PolyHIPEs through Schiff-Base Condensation Reaction. *Polym. Chem.* **2022**, *13* (4), 474−478.

(39) Ballai, G.; Kotnik, T.; Finšgar, M.; Pintar, A.; Kónya, Z.; Sápi, A.; Kovačič, S. Highly Porous Polymer Beads Coated with Nanometer-Thick Metal Oxide Films for Photocatalytic Oxidation of Bisphenol A. *ACS Appl. Nano Mater.* **2023**, *6* (21), 20089−20098.

(40) Shirakawa, H.; Louis, E. J.; MacDiarmid, A. G.; Chiang, C. K.; Heeger, A. J. Synthesis of Electrically Conducting Organic Polymers: Halogen Derivatives of Polyacetylene, (CH). *J. Chem. Soc. Chem. Commun.* **1977**, No. No. 16, 578−580.

(41) Masuda, T. Substituted Polyacetylenes: Synthesis, Properties, and Functions. *Polym. Rev.* **2017**, *57* (1), 1−14.

(42) Ke, Z.; Abe, S.; Ueno, T.; Morokuma, K. Rh-Catalyzed Polymerization of Phenylacetylene: Theoretical Studies of the Reaction Mechanism, Regioselectivity, and Stereoregularity. *J. Am. Chem. Soc.* **2011**, *133* (20), 7926−7941.

(43) Kishimoto, Y.; Eckerle, P.; Miyatake, T.; Kainosho, M.; Ono, A.; Ikariya, T.; Noyori, R. Well-Controlled Polymerization of Phenylacetylenes with Organorhodium(I) Complexes: Mechanism and Structure of the Polyenes. *J. Am. Chem. Soc.* **1999**, *121* (51), 12035−12044.

(44) Trhlíková, O.; Zedník, J.; Balcar, H.; Brus, J.; Sedláček, J. [Rh(Cycloolefin)(Acac)] Complexes as Catalysts of Polymerization of Aryl- and Alkylacetylenes: Influence of Cycloolefin Ligand and Reaction Conditions. *J. Mol. Catal.* **2013**, *378*, 57−66.

(45) Balcar, H.; Sedláček, J.; Čejka, J.; Vohlídal, J. MCM-41-Immobilized [Rh(Cod)OCH3]2 Complex − A Hybrid Catalyst for the Polymerization of Phenylacetylene and Its Ring-Substituted Derivatives. *Macromol. Rapid Commun.* **2002**, *23* (1), 32−37.

(46) Sedláček, J.; Balcar, H. Substituted Polyacetylenes Prepared with Rh Catalysts: From Linear to Network-Type Conjugated Polymers. *Polym. Rev.* **2017**, *57* (1), 31−51.

(47) Sekerová, L.; Lhotka, M.; Vyskočilová, E.; Faukner, T.; Slováková, E.; Brus, J.; Červený, L.; Sedláček, J. Hyper-Cross-Linked Polyacetylene-Type Microporous Networks Decorated with Terminal Ethynyl Groups as Heterogeneous Acid Catalysts for Acetalization and Esterification Reactions. *Chem. - Eur. J.* **2018**, *24* (55), 14742−14749.

(48) Havelková, L.; Bashta, B.; Vaňková, M.; Zedník, J.; Brus, J.; Svoboda, J.; Vagenknechtová, A.; Sedláček, J. Functionalized Hyper-Cross-Linked Porous Homopolymers of Ring-Substituted 1,3-Diethynylbenzenes and Their Physisorption Activity. *Microporous Mesoporous Mater.* **2024**, *365*, No. 112908.

(49) Šorm, D.; Bashta, B.; Blahut, J.; Císařová, I.; Dolejšová Sekerová, L.; Vyskočilová, E.; Sedláček, J. Porous Polymer Networks Cross-Linked by Novel Copper Schiff Base Complex: From Synthesis to Catalytic Activity. *Eur. Polym. J.* **2023**, *184*, No. 111772.

(50) Makuła, P.; Pacia, M.; Macyk, W. How To Correctly Determine the Band Gap Energy of Modified Semiconductor Photocatalysts Based on UV−Vis Spectra. *J. Phys. Chem. Lett.* **2018**, *9* (23), 6814−6817.

(51) Mark, H. F. *Encyclopedia of Polymer Science and Technology, Concise*, 3rd ed.; John Wiley & Sons, 2013; Vol. *1*.

(52) Chen, W.; Duan, L.; Wang, L.; Zhu, D. Adsorption of Hydroxyl- and Amino-Substituted Aromatics to Carbon Nanotubes. *Environ. Sci. Technol.* **2008**, *42* (18), 6862−6868.

(53) Ji, L.; Chen, W.; Duan, L.; Zhu, D. Mechanisms for Strong Adsorption of Tetracycline to Carbon Nanotubes: A Comparative Study Using Activated Carbon and Graphite as Adsorbents. *Environ. Sci. Technol.* **2009**, *43* (7), 2322−2327.

(54) Sun, Z.; Zhao, L.; Liu, C.; Zhen, Y.; Ma, J. Fast Adsorption of BPA with High Capacity Based on π-π Electron Donor-Acceptor and Hydrophobicity Mechanism Using an in-Situ Sp2 C Dominant N-Doped Carbon. *J. Chem. Eng.* **2020**, *381*, No. 122510.

(55) Yi, L.; Zuo, L.; Wei, C.; Fu, H.; Qu, X.; Zheng, S.; Xu, Z.; Guo, Y.; Li, H.; Zhu, D. Enhanced Adsorption of Bisphenol A, Tylosin, and Tetracycline from Aqueous Solution to Nitrogen-Doped Multiwall Carbon Nanotubes via Cation-π and π-π Electron-Donor-Acceptor (EDA) Interactions. *Sci. Total Environ.* **2020**, *719*, No. 137389.

(56) Xu, J.; Wang, L.; Zhu, Y. Decontamination of Bisphenol A from Aqueous Solution by Graphene Adsorption. *Langmuir* **2012**, *28* (22), 8418−8425.

(57) Upoma, B. P.; Yasmin, S.; Ali Shaikh, Md. A.; Jahan, T.; Haque, Md. A.; Moniruzzaman, M.; Kabir, M. H. A Fast Adsorption of Azithromycin on Waste-Product-Derived Graphene Oxide Induced by H-Bonding and Electrostatic Interactions. *ACS Omega* **2022**, *7* (34), 29655−29665.

(58) Ahmed, I.; Hasan, Z.; Lee, G.; Lee, H. J.; Jhung, S. H. Contribution of Hydrogen Bonding to Liquid-Phase Adsorptive Removal of Hazardous Organics with Metal-Organic Framework-Based Materials. *J. Chem. Eng.* **2022**, *430*, No. 132596.

(59) Guo, S.; Zou, Z.; Chen, Y.; Long, X.; Liu, M.; Li, X.; Tan, J.; Chen, R. Synergistic Effect of Hydrogen Bonding and π-π Interaction for Enhanced Adsorption of Rhodamine B from Water Using Corn Straw Biochar. *Environ. Pollut.* **2023**, *320*, No. 121060.

(60) Czili, H.; Horváth, A. Applicability of Coumarin for Detecting and Measuring Hydroxyl Radicals Generated by Photoexcitation of TiO2 Nanoparticles. *Appl. Catal., B* **2008**, *81* (3), 295−302.

Supporting information for paper:

Hierarchically Porous Polyacetylene Networks: Adsorptive Photocatalysts for Efficient Bisphenol A Removal from Water

David Šorm[a], *Jiří Brus*[b], *Albin Pintar*[c], *Jan Sedláček*[a] *and Sebastijan Kovačič*[c,d]*

a) Department of Physical and Macromolecular Chemistry, Faculty of Science, Charles University, Hlavova 2030, Prague 2, 128 43, Czech Republic

b) Institute of Macromolecular Chemistry, Czech Academy of Sciences, Heyrovský Sq. 2, 162 00, Prague, Czech Republic

c) Department of Inorganic Chemistry and Technology, National Institute of Chemistry, Hajdrihova 19, SI-1001 Ljubljana, Slovenia

d) University of Maribor, Faculty of Chemistry and Chemical Engineering, Smetanova 17, SI-2000 Maribor, Slovenia; E-mail: sebastijan.kovacic@um.si

FTIR characterization

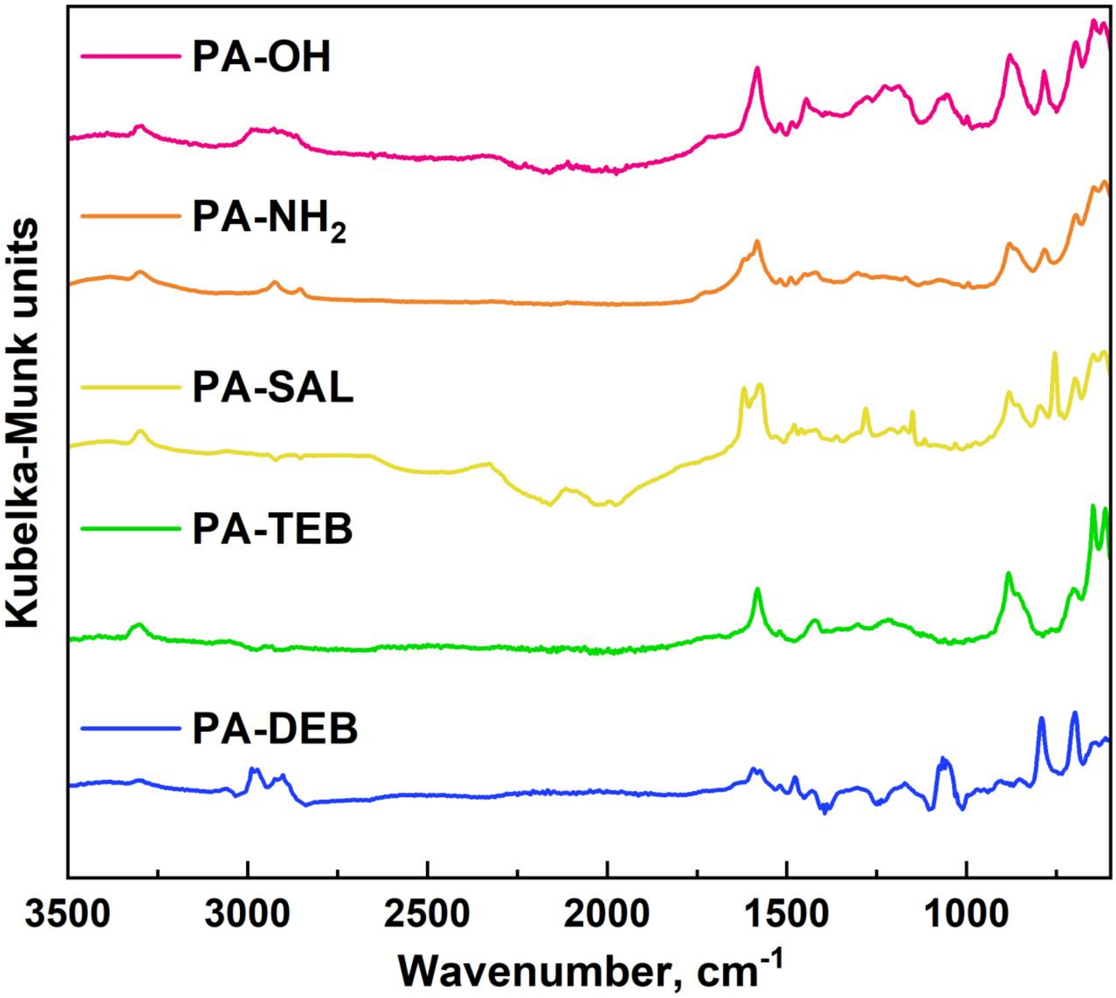

Figure S1. FTIR spectra of PA-PHs: PA-OH, PA-NH$_2$, PA-SAL, PA-TEB and PA-DEB.

^{13}C CP/MAS characterization

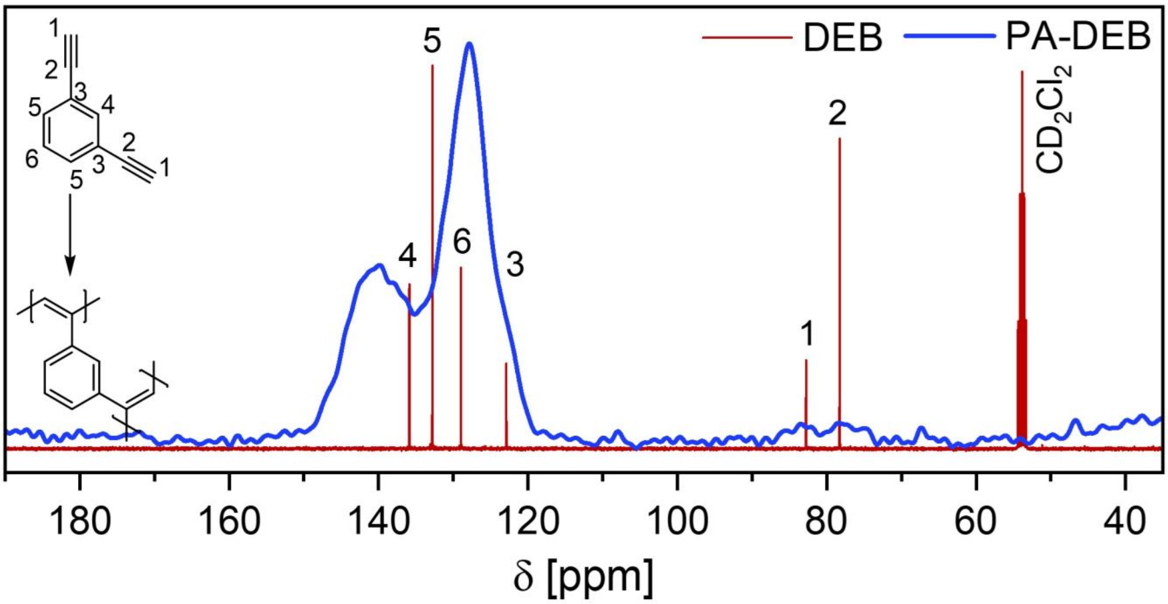

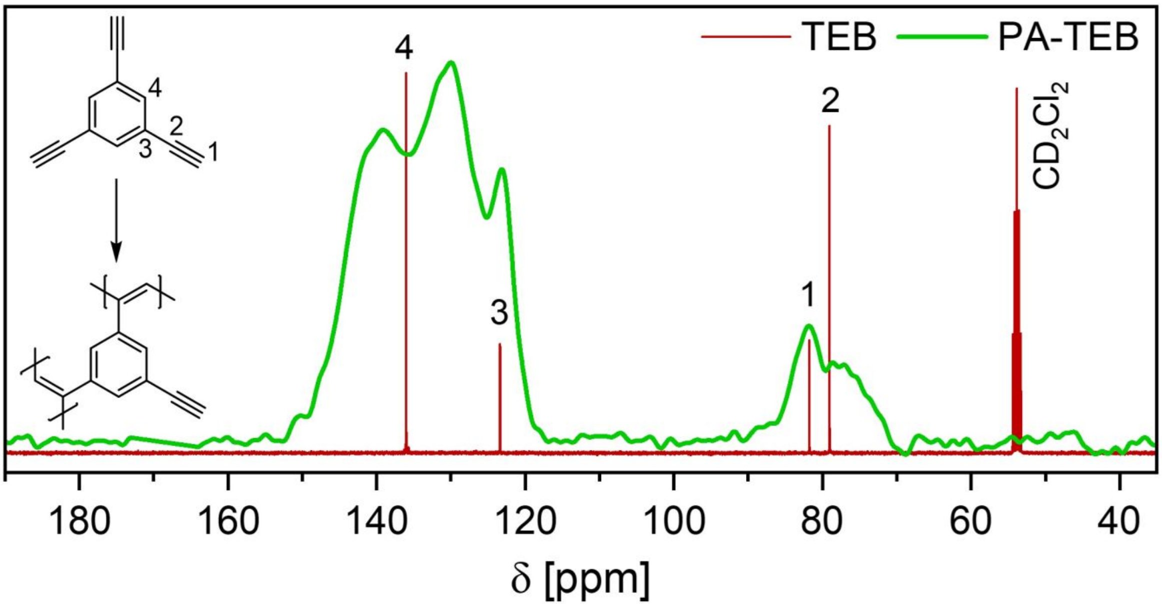

Figure S2. ^{13}C CP/MAS NMR spectra of homopolymers PA-DEB and PA-TEB compared with ^{13}C NMR spectra of respective monomers 1,3-diethynylbenzene and 1,3,5-triethynylbenzene measured in CD_2Cl_2.

High magnification SEM analysis

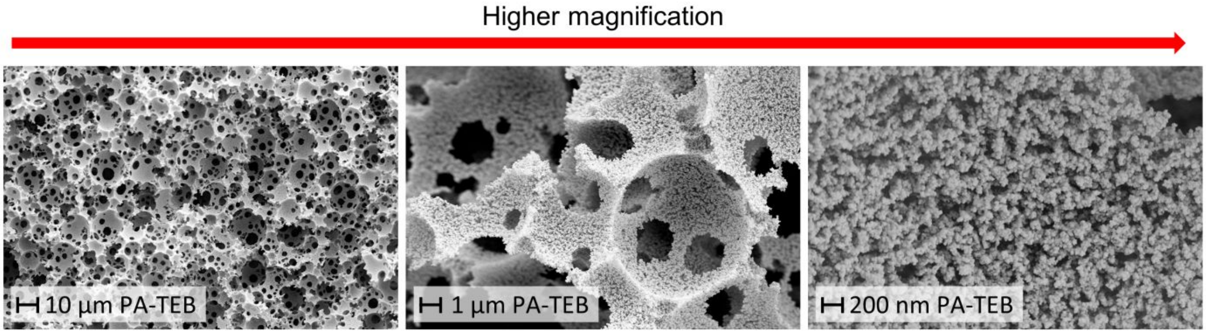

Figure S3. Comparison of different magnification by SEM on network PA-TEB.

Adsorption-&-photodegradation of bisphenol A (BPA) on the PA-PH

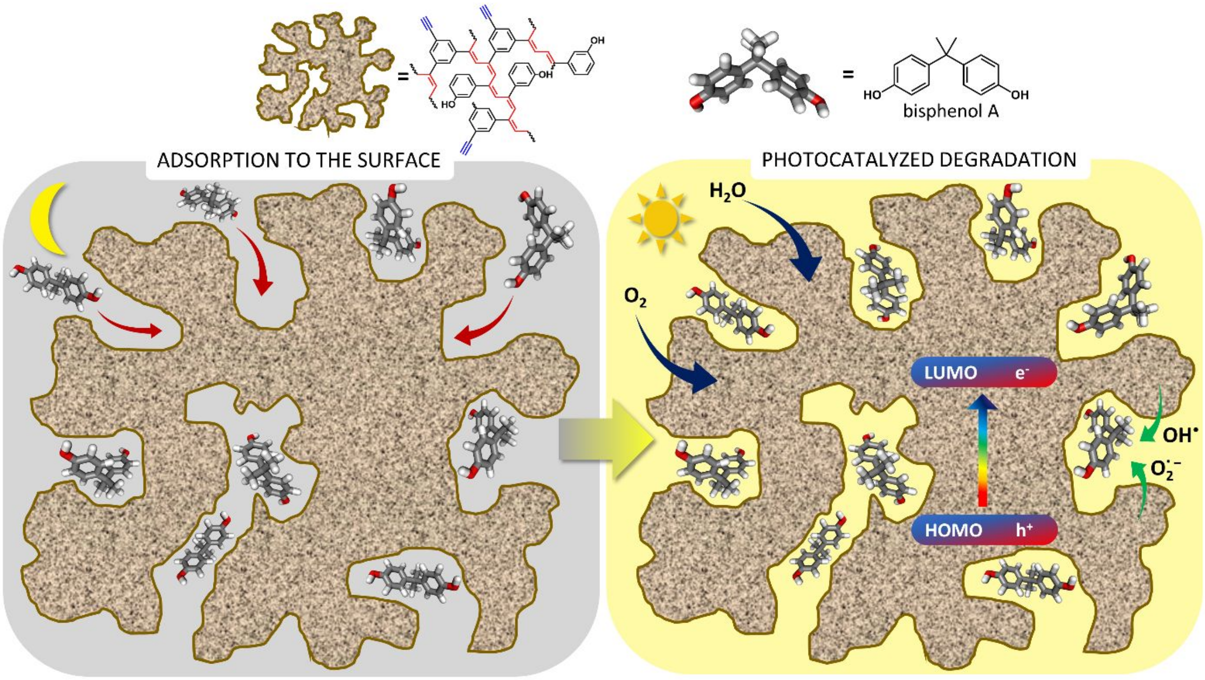

Figure S4. Adsorption of bisphenol A and photocatalytic processes on the surface of polyacetylene-based polyHIPE network.

UV VIS DRS characterization

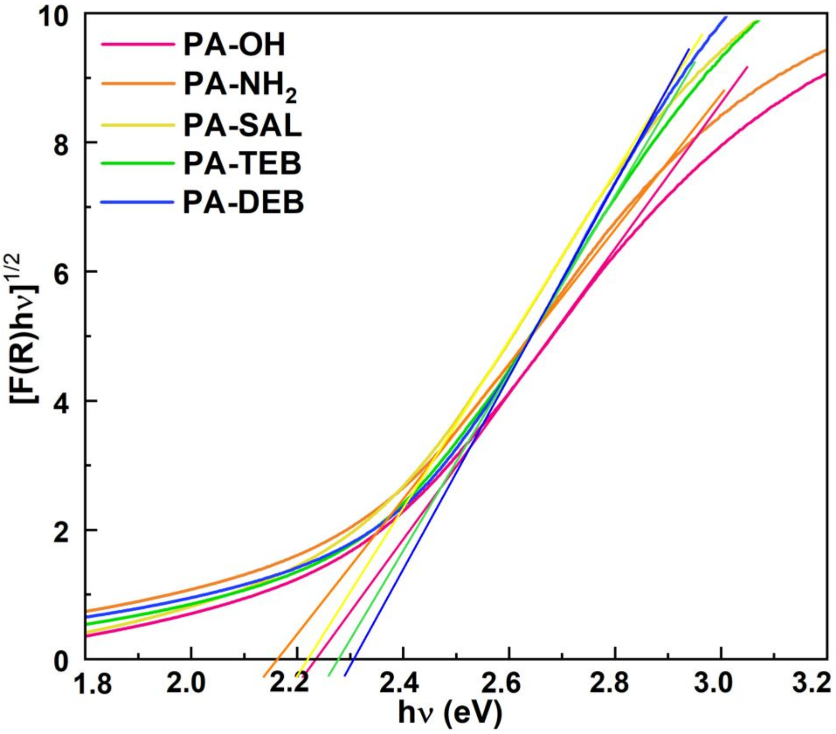

Figure S5. The Tauc plots.

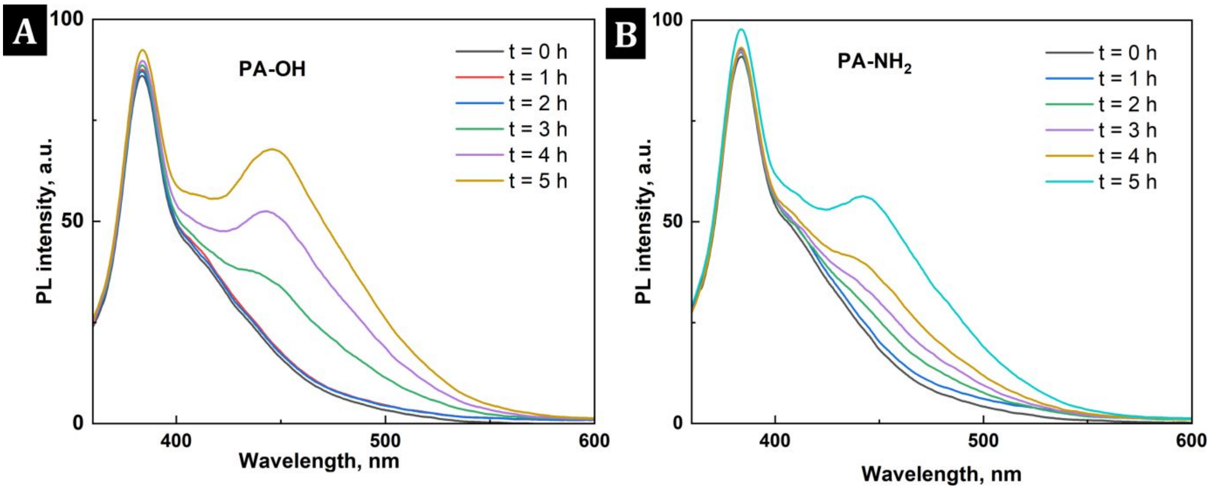

Figure S6. Coumarin test for the observation of 7-hydroxycoumarin generation using PA-OH (**A**) and PA-NH_2 (**B**) networks. Maximum of coumarin @ λ=384 nm; maximum of 7-hydroxycoumarin @ λ=445 nm.